Sagittarius A* and Low Luminosity Accreting Sources

Physikalisches Kolloquium, 13.6.2017 * Christian-Albrechts-Universität zu Kiel

Andreas Eckart

I.Physikalisches Institut der Universität zu Köln

Max-Planck-Institut für Radioastronomie, Bonn

SEVENTH FRAMEWORK PROGRAMME

STRONGGRAVITY

EU FP7-SPACE research project 312789 2013 - 2017

Max-Planck-Institut für Radioastronomie

I. Physikalisches Institut Universität zu Köln

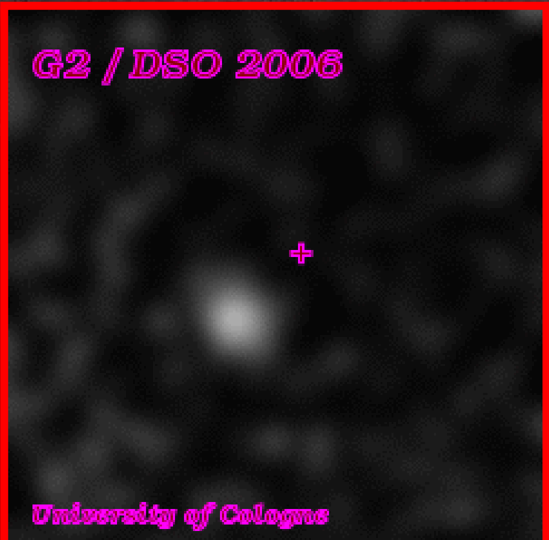

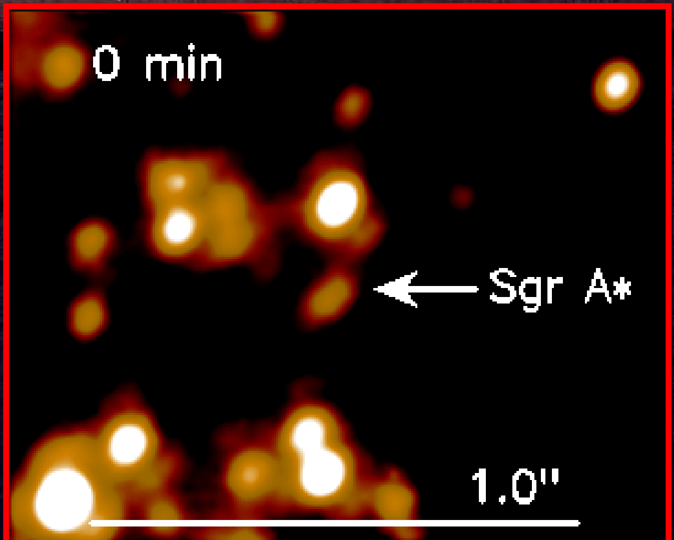

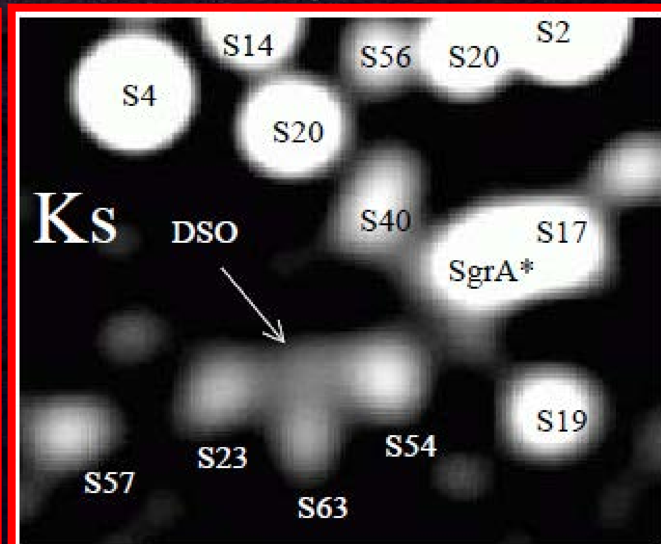

Structure of galactic nuclear regions

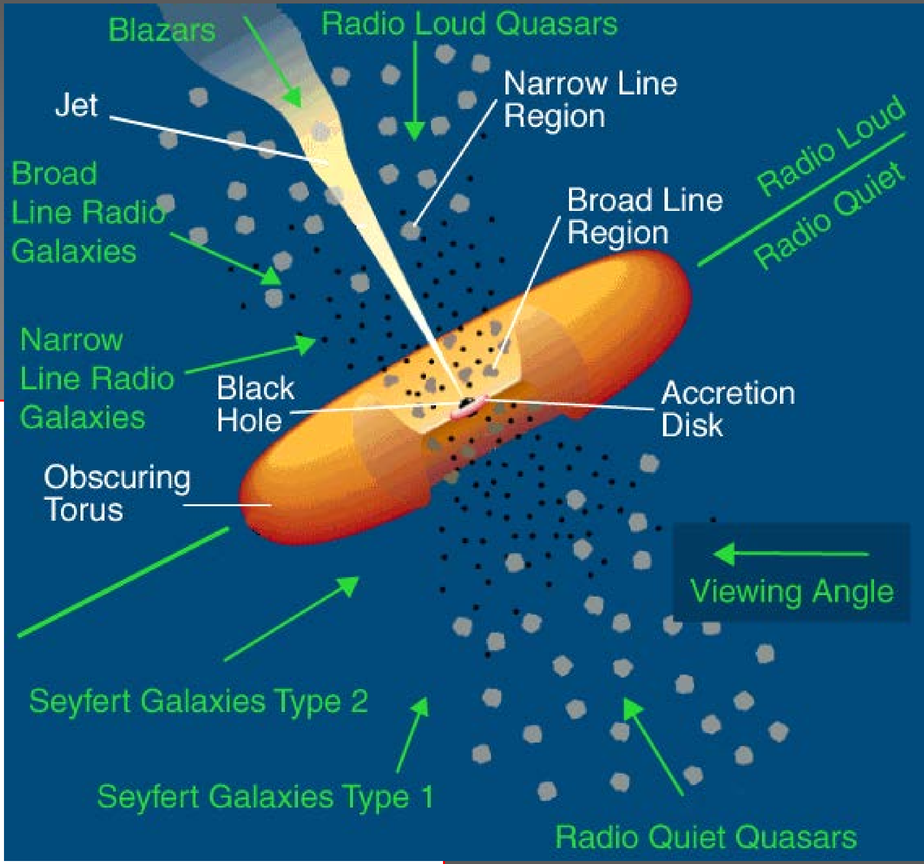

- broad line region (BLR)
- narrow line region (NLR)
- nuclear accretion disk
- obscuring torus
- unified scheme
- Extragalactic zoology

Test case: Galactic Center / NUGA survey

Seyfert 1 nuclei

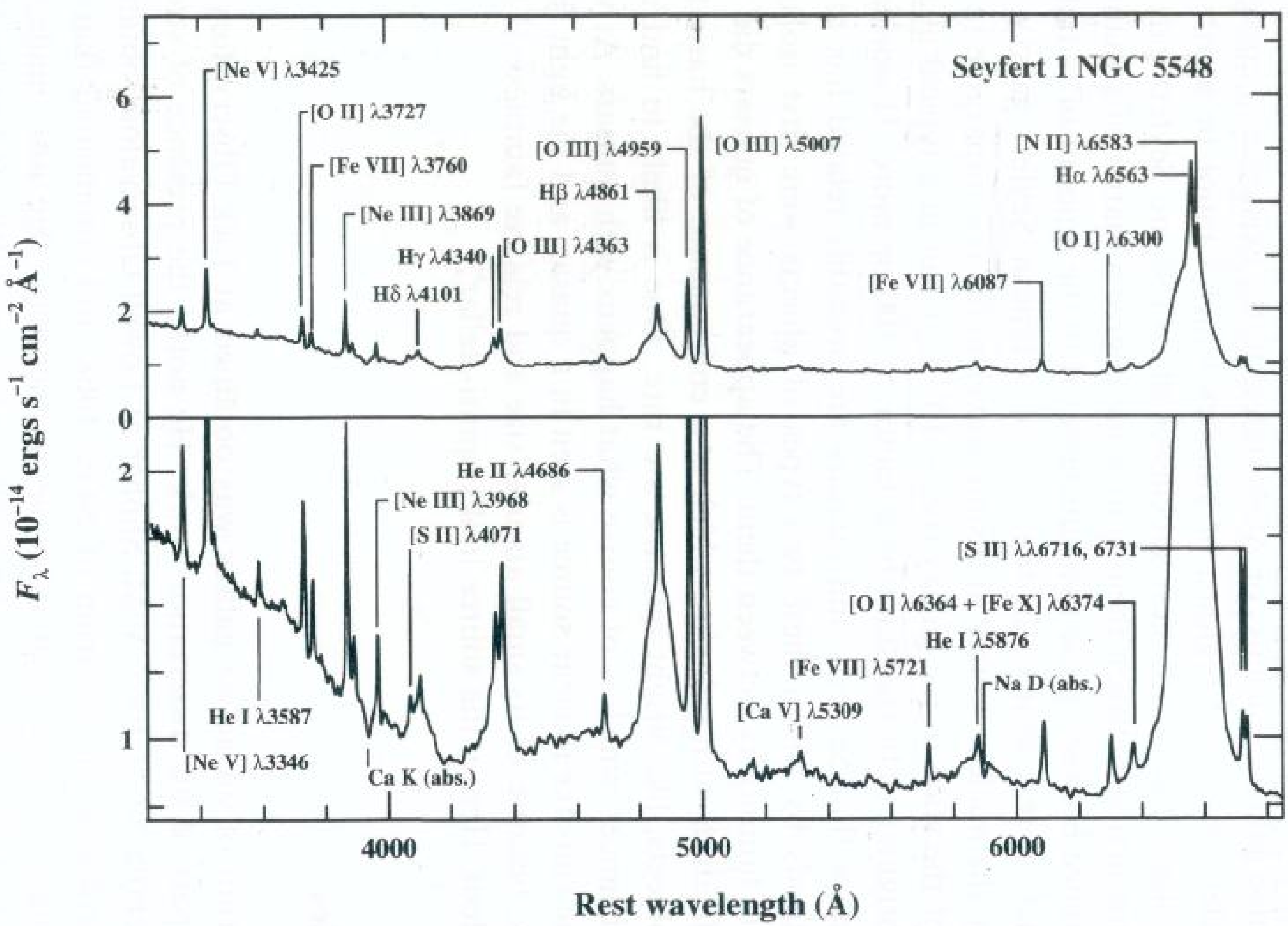

Seyfert 2 nuclei

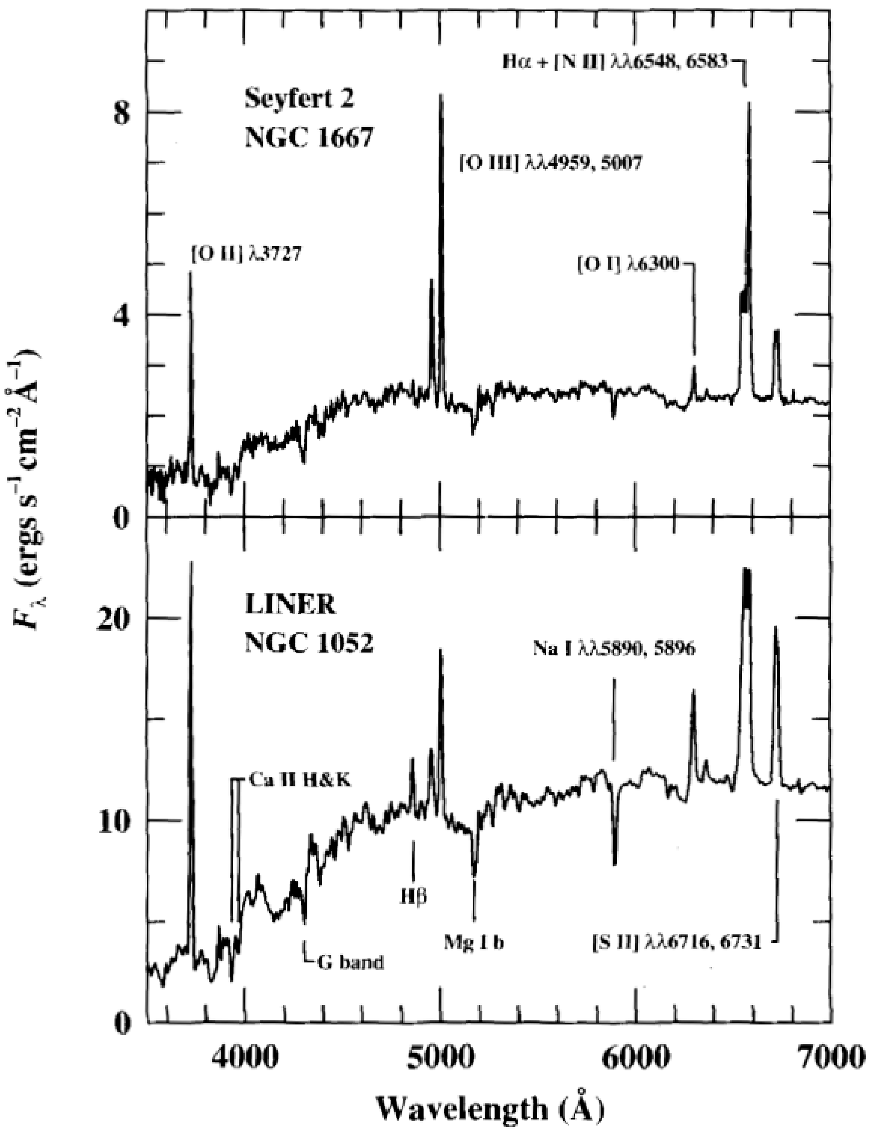

AGN structure

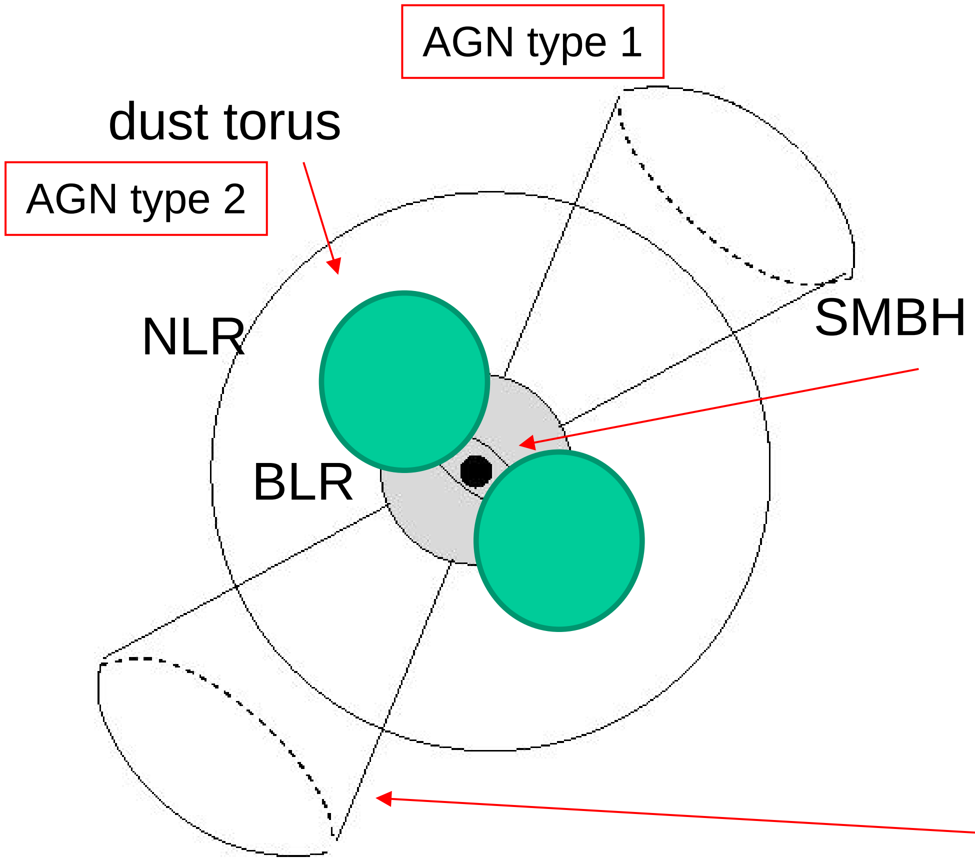

BLR:
r ~ 10 light days
FWHM ~ 5000 km/s

M=rv**2/G=
10**7-10**8 Msloar

Broad H-recombination lines
CIII], CIV, HeII
density: n=10**11 cm**-3

NLR:
r ~ 10-100 pc
FWHM ~ 200 - 900 km/s

forbidden lines
[OII], [OIII],[NII] ...
ionization cones

density: n=10**3-10**6 cm**-3

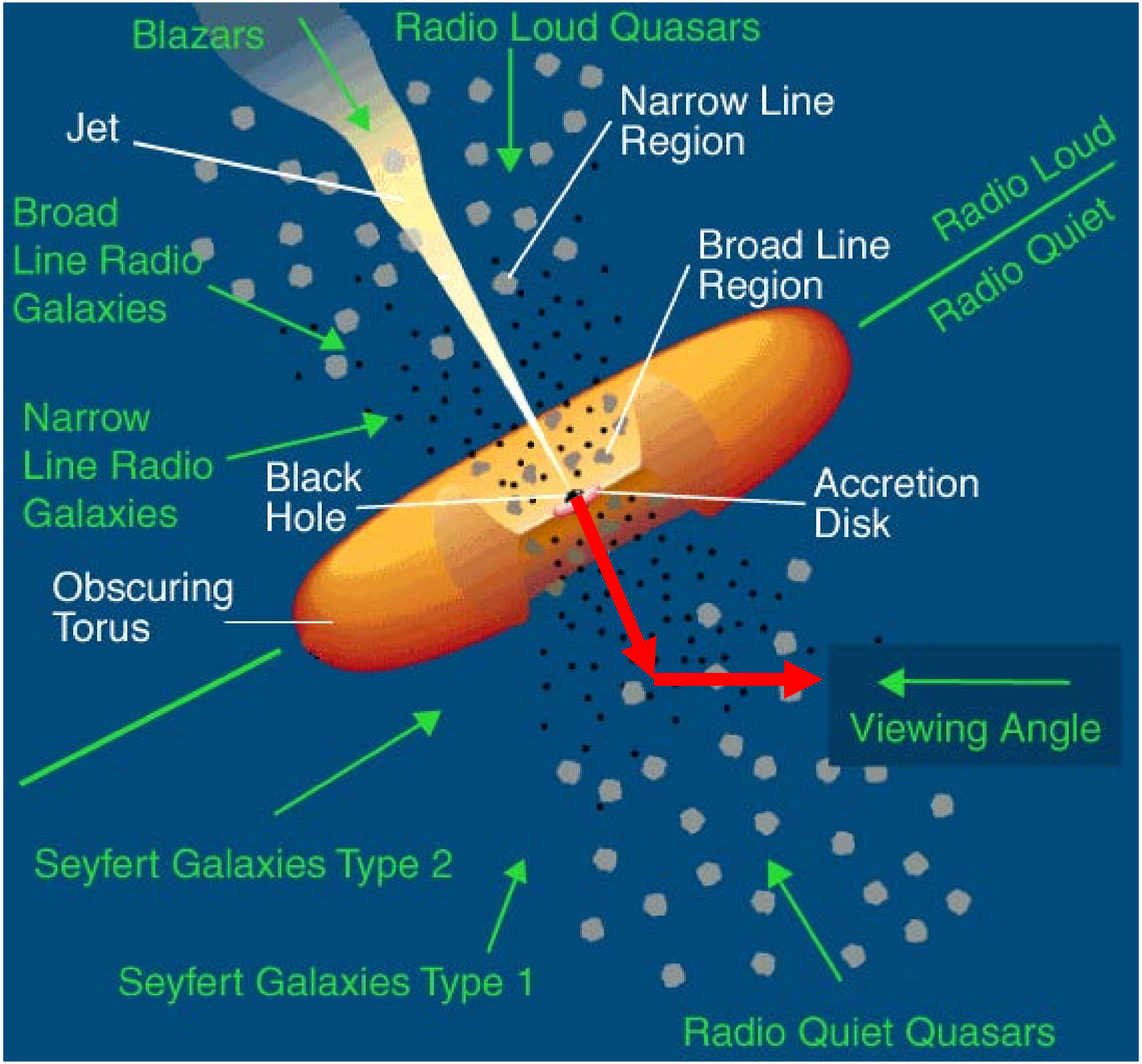
Blazars
Radio Loud Quasars
Jet
Narrow Line Region
Broad Line Radio Galaxies
Broad Line Region
Radio Loud
Radio Quiet
Narrow Line Radio Galaxies
Black Hole
Accretion Disk
Obscuring Torus
Viewing Angle
Seyfert Galaxies Type 2
Seyfert Galaxies Type 1
Radio Quiet Quasars

Accretion of Mass

Structure of the accretion disk

CASE 1: low accretion rate
high opacity

$$\dot{M} / \dot{M}_E \lesssim 0.1$$

thin accretion disk
compared to diameter
efficiency: $\eta \approx 0.1$

CASE 0
plus advection
dominated accretion
for LLAGN
$\dot{M} / \dot{M}_E$

X-ray
UV

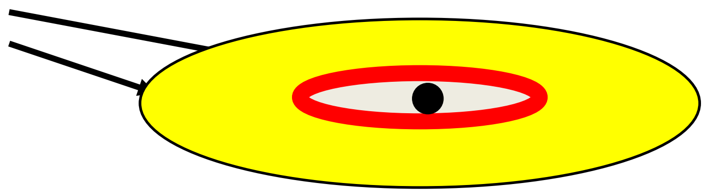

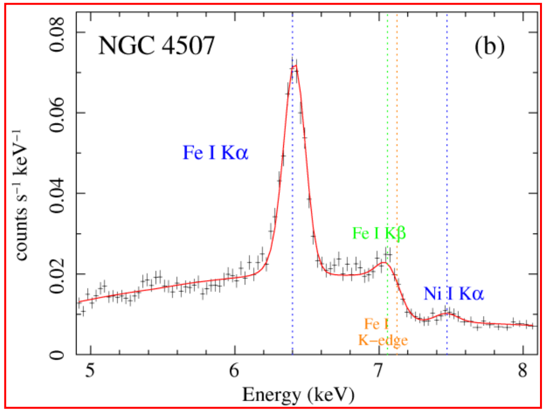

Suzaku data

CASE 2: high accretion rate
radiation heats disk
disk inflates and cools
at larger radii, i.e.
radiation becomes
inefficient.

$$\dot{M} / \dot{M}_E \gg 1$$

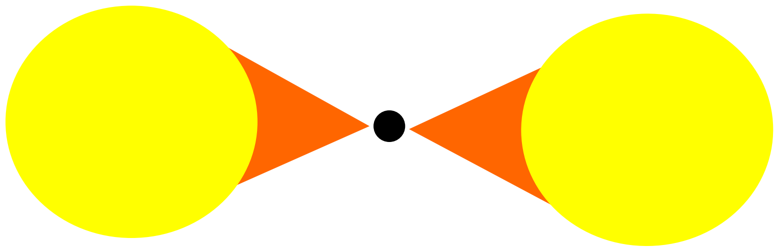

looks like a
10**4 K
young star

SgrA* as an extreme LLAGN Nucleus

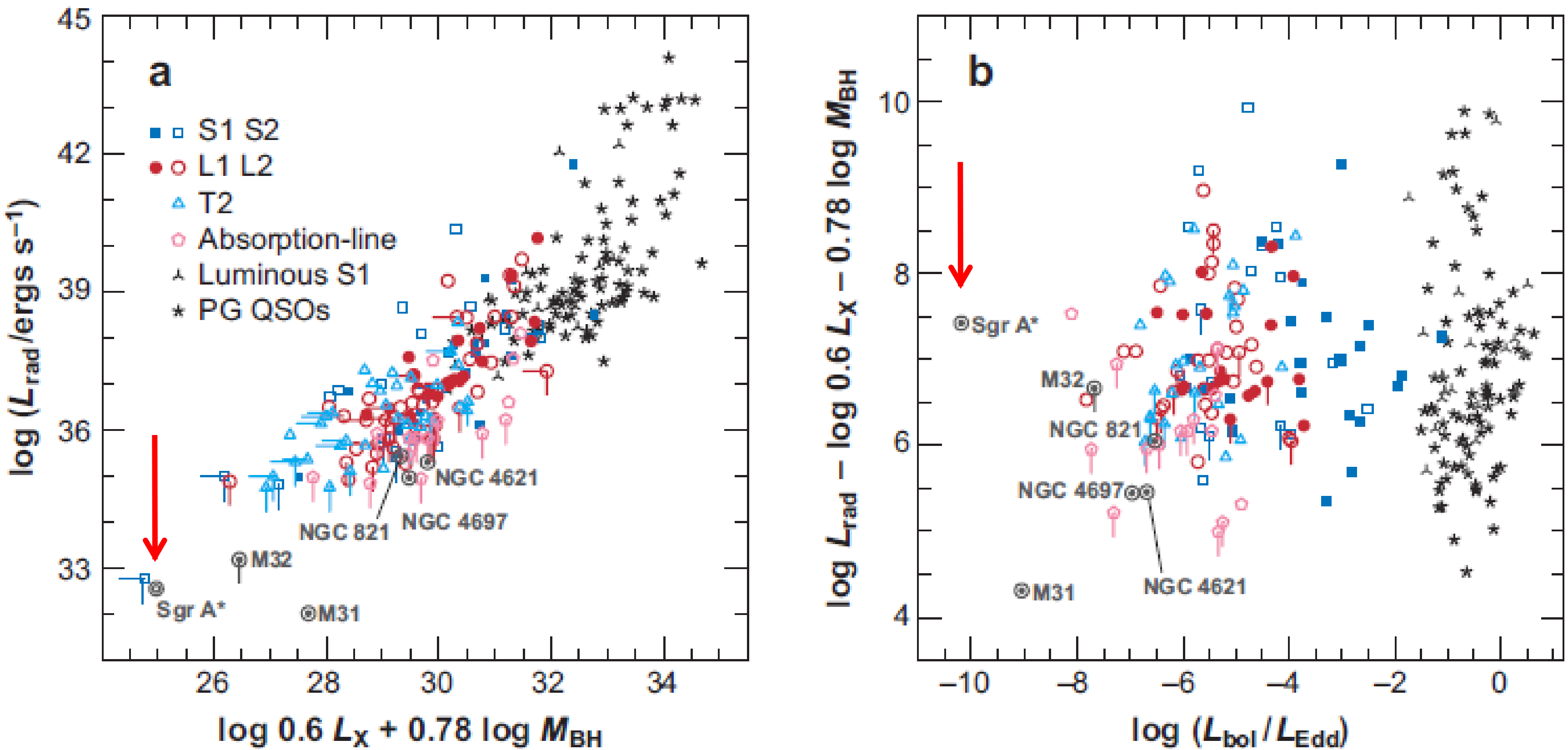

Ho 2008: Fundamental plane correlation among core radio luminosity, X-ray (a)luminosity, and BH mass. (*b*) Deviations from the fundamental plane as a function of Eddington ratio.

SgrA* is accreting in an advection dominated mode, else ist luminosity would be than 10^7 times higher

Demographics of activity in nearby galaxies.

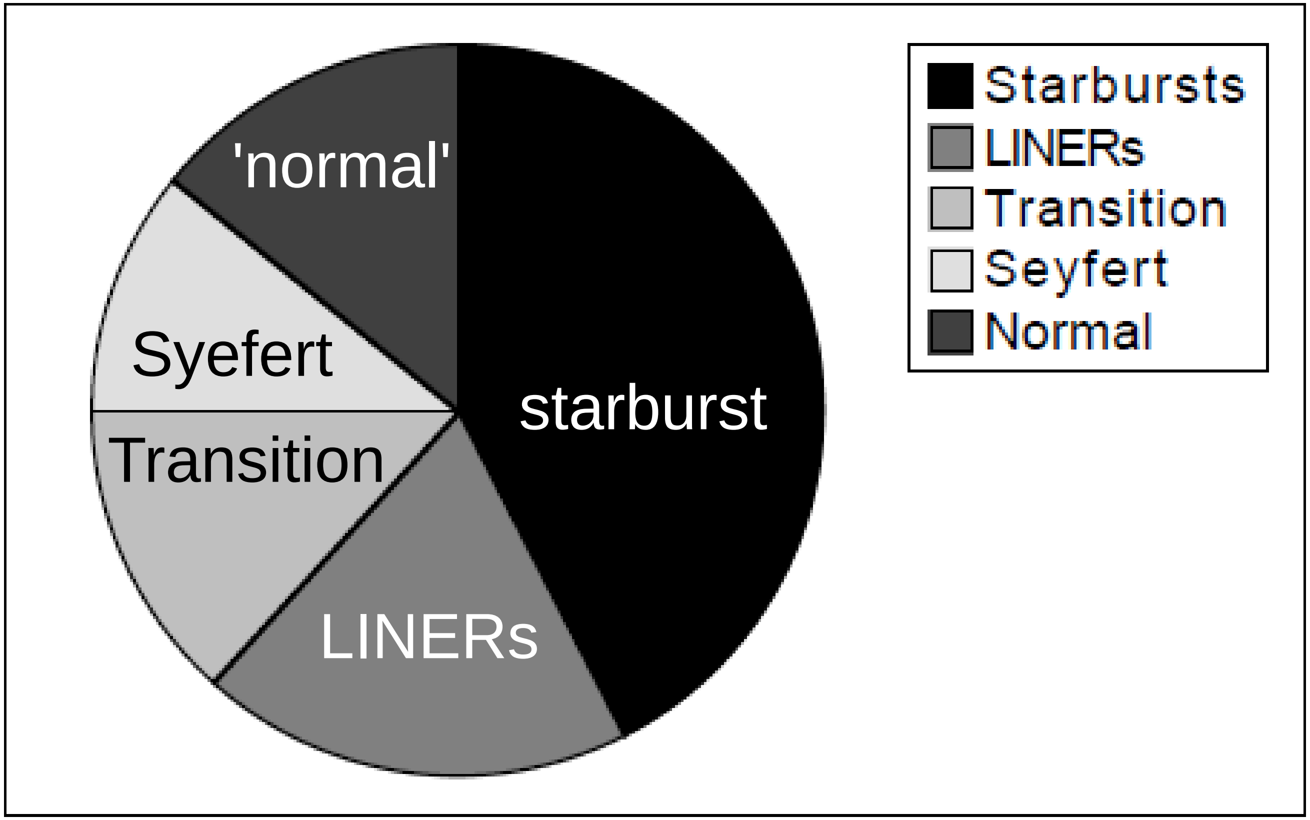

Ptak 2000

Low-luminosity AGN (with Lx < 10^42 ergs s^−1) far outnumber ordinary AGN, and are therefore perhaps more relevant to our understanding of AGN phenomena and the relationship between AGN and host galaxies. Many normal galaxies harbor LINER and starburst nuclei, which, together with LLAGN, are a class of “low-activity” galaxies that have a number of surprisingly similar X-ray characteristics, despite their heterogenous optical classification. This strongly supports the hypothesis of an AGN-starburst connection.

The proposed unification scheme of Falcke et al. (2004) for accreting black holes in the mass and accretion rate plane. The X-axis denotes the black hole mass and the Y -axis the accretion power. For stellar black holes it coincides with the two normal black hole states.
For the AGN zoo we include low-luminosity AGN (LLAGN), radio galaxies (RG), low ionization emission region sources (LINER), Seyferts, and quasars.

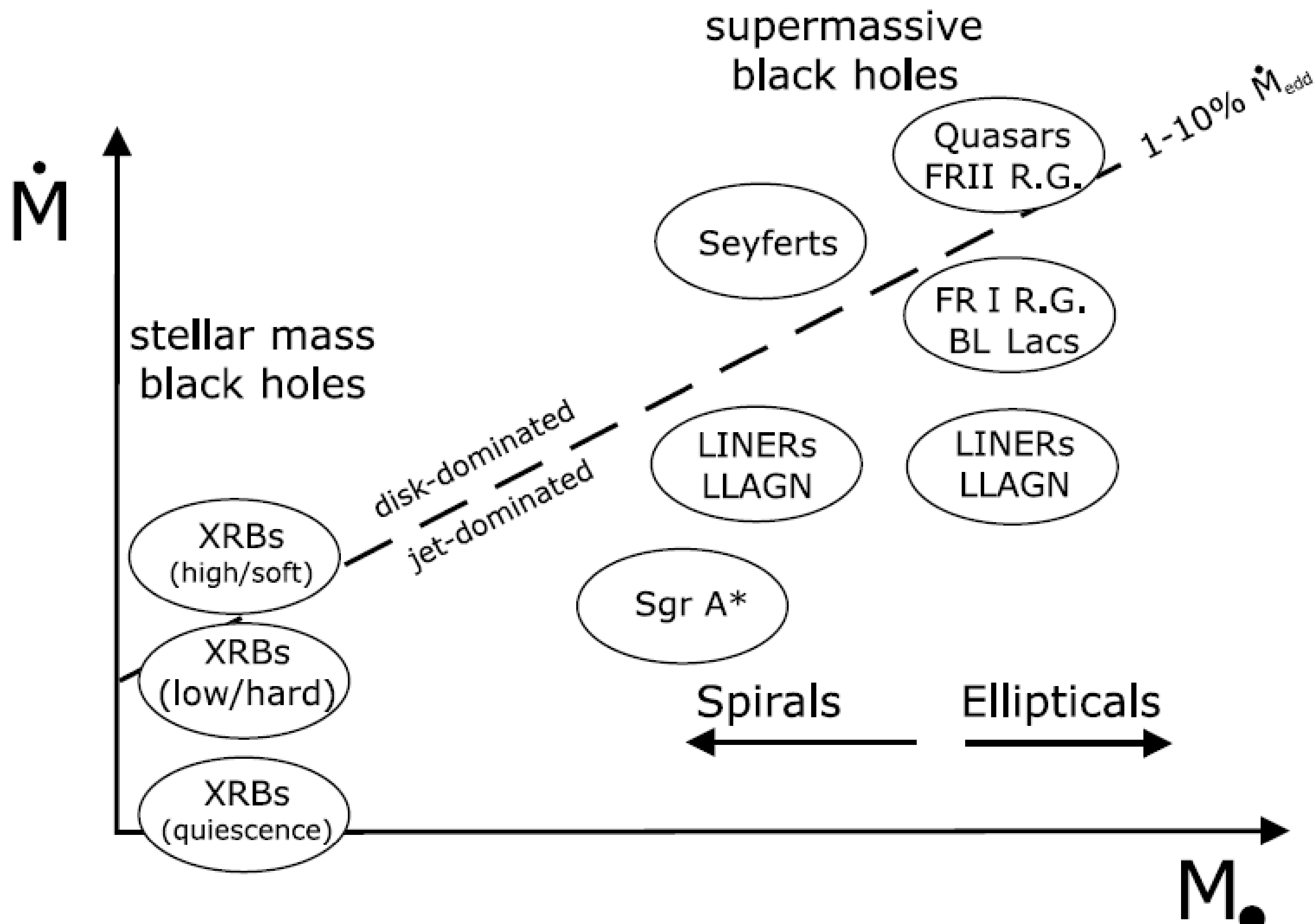

Körding & Falcke (2004)

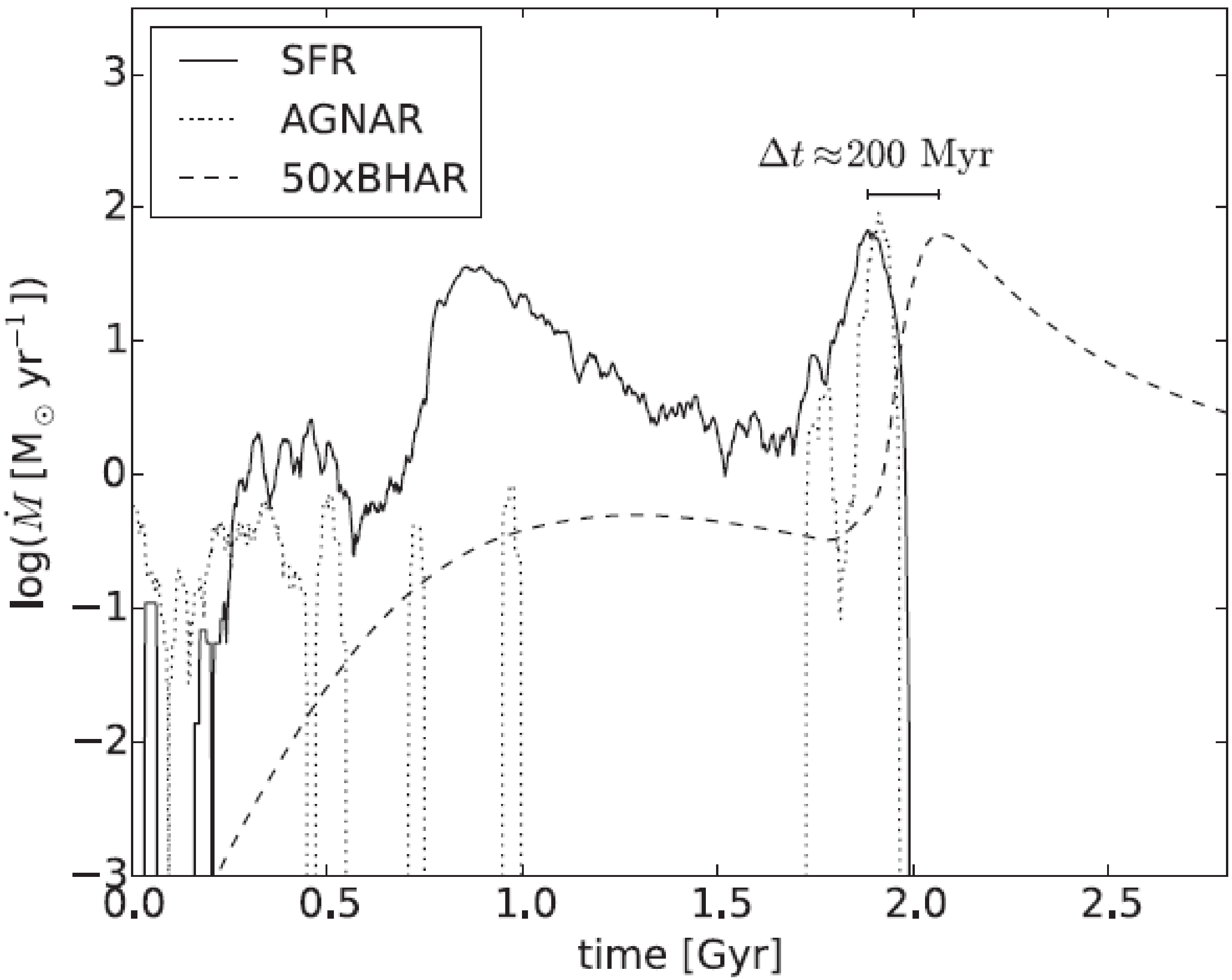

SFR, AGN accretion and Black Hole accretion as functions of time. Left: with AGN feedback

Blank & Duschl 2016

There is strong observational evidence indicating a time lag of order of some 100 Myr between the onset of starburst and AGN activity in galaxies. The time lag is given via dynamical and BH disk viscosity processes.

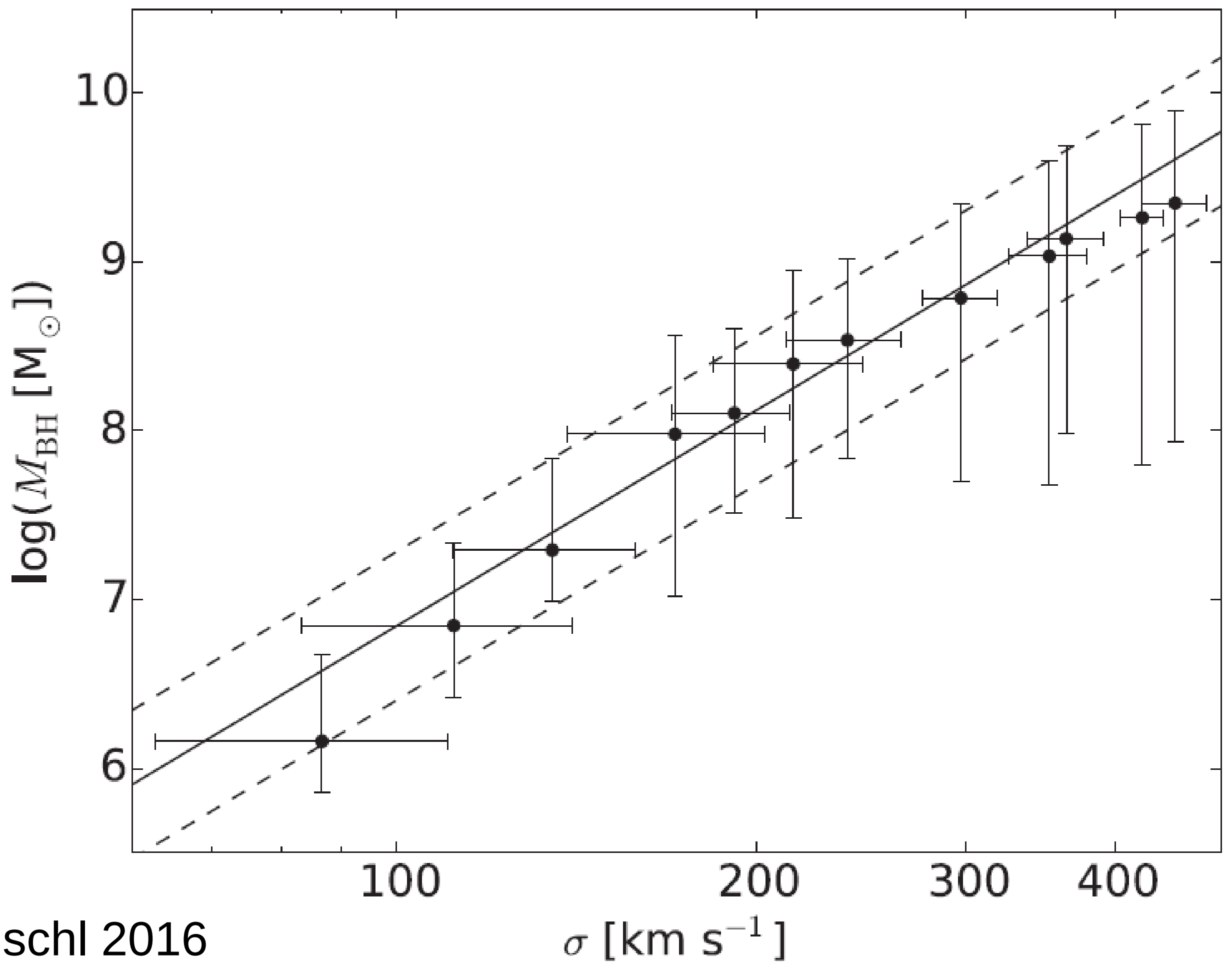

Blank & Duschl 2016

Black hole mass MBH as function of the galaxy's stellar velocity dispersion σ. The dots indicate the black hole mass at the time the BHAR reaches its maximum value. The horizontal bars indicate the error of σ, the vertical bars indicate the range of black hole mass from the time of the end of the starburst to the time the BHAR decreases to 0.3 per cent of its Eddington rate. The solid line indicates the observed MBH-σ correlation with intrinsic scatter (dashed lines) according to Gültekin et al. (2009).

MBH scaling relation for spiral galaxies, spheroids, ellipticals

Koliopanos et al (2017) find that all LLAGN in their list have low-mass central black holes with log MBH/M⊙≈6.5 on average (closer to spirals, below ellipticals ?).

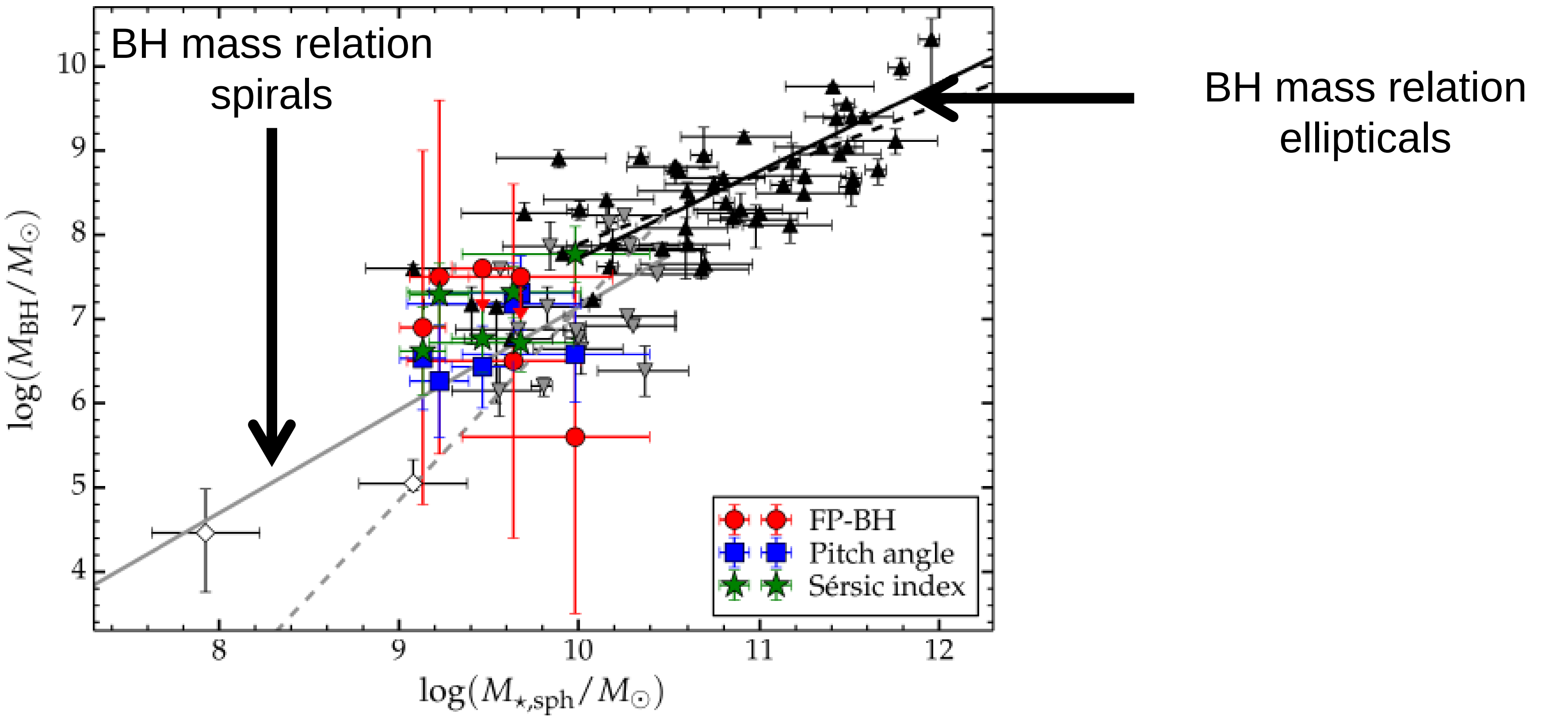

Koliopanos et al. 2017

Low Surface brightness AGN tend to have BH masses below the standard relations for spirals and ellipticals.

Subramanian et al. 2016

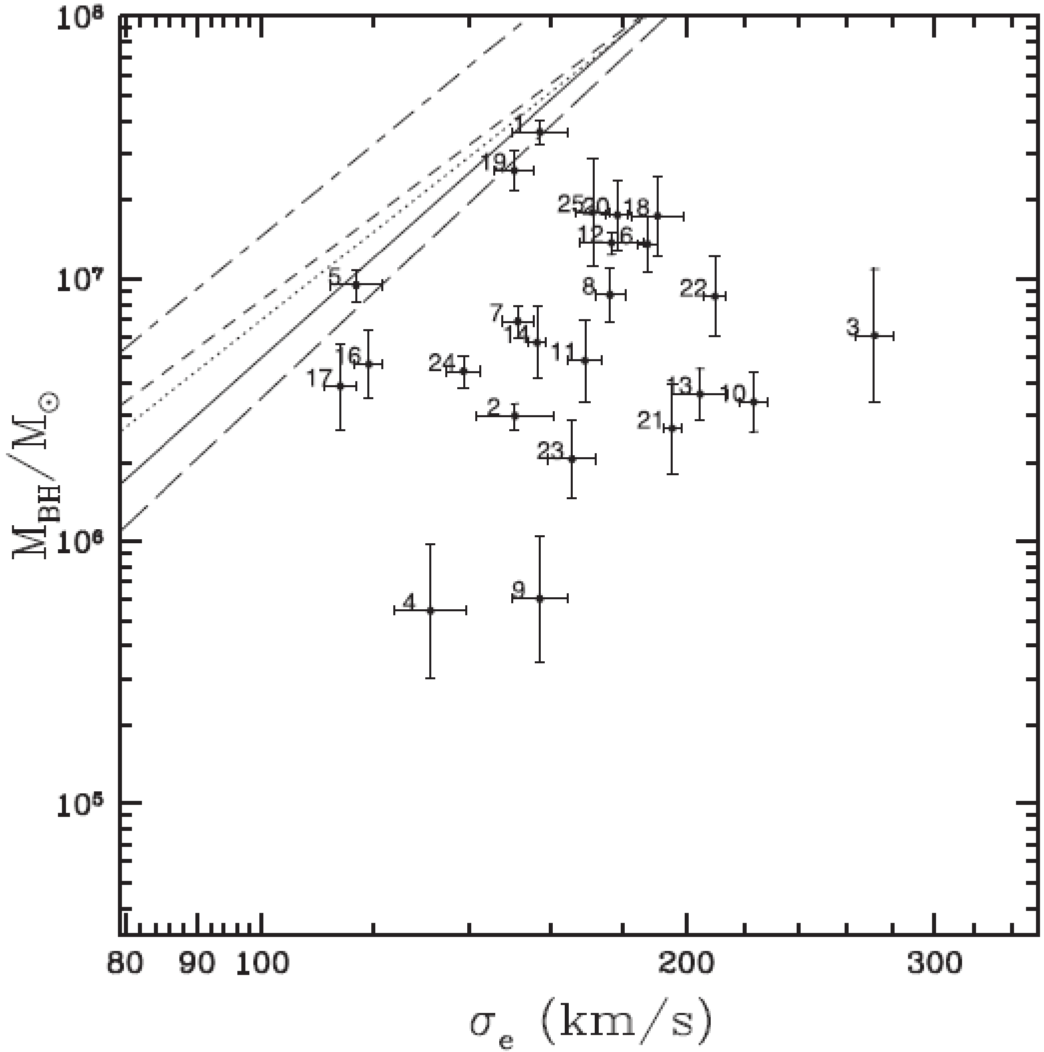

The M–σe plot with broad line AGN candidates. The linear regression lines given by Tremaine et al. (2002), Ferrarese & Merritt (2000), Gültekin et al. (2009) and Kormendy & Ho (2013) relation for classical bulges/elliptical galaxies and (McConnell &Ma 2013) relation for late-type galaxies (dashed, solid, dotted short-long dashed and long-dashed lines, respectively) for MBH against σe are also shown.

Starformation and Blackhole Growth in Nearby QSOs

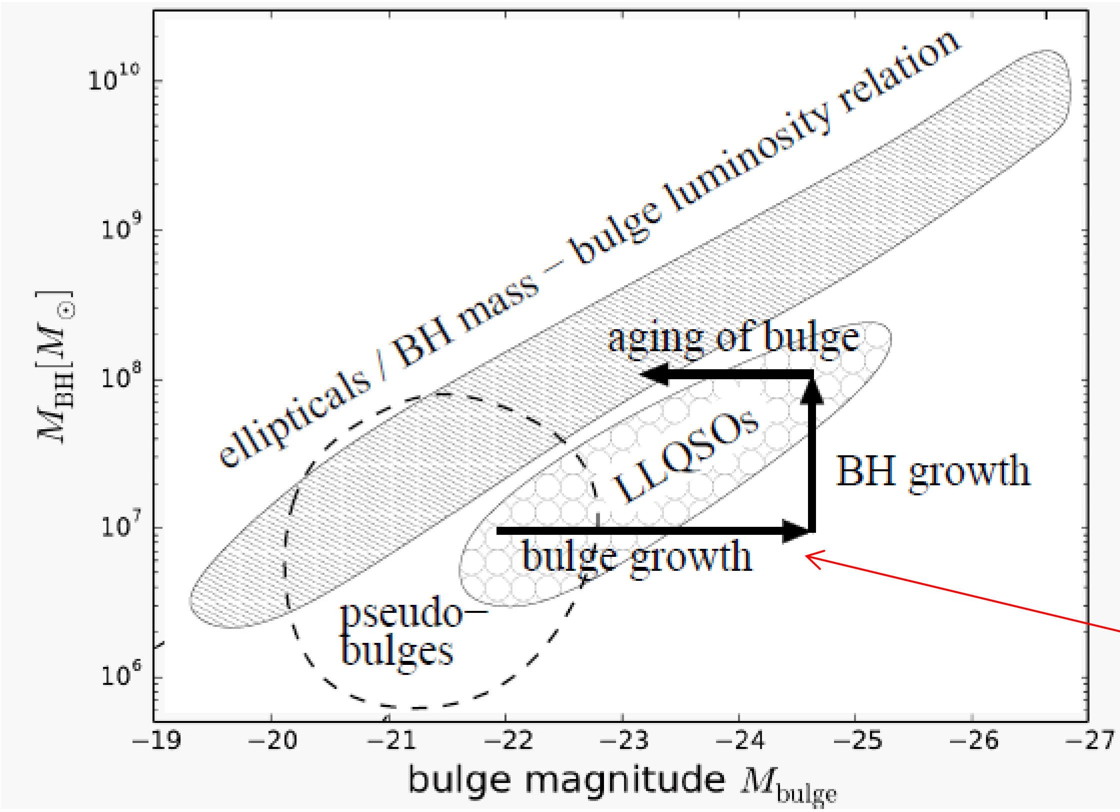

Figure 2: A possible evolutionary scenario in the black hole mass - bulge luminosity diagram. Accretion of matter onto the central region results into enhanced star formation and black hole growth. Young stellar populations cause over-luminous bulges compared to inactive galaxies on the relation. Black hole growth and aging of the stellar populations then move the objects back onto the relation.

Bulge Luminosity Growth:
Conditions of Starformation

in Nuclei of Galaxies

Busch et al. 2016

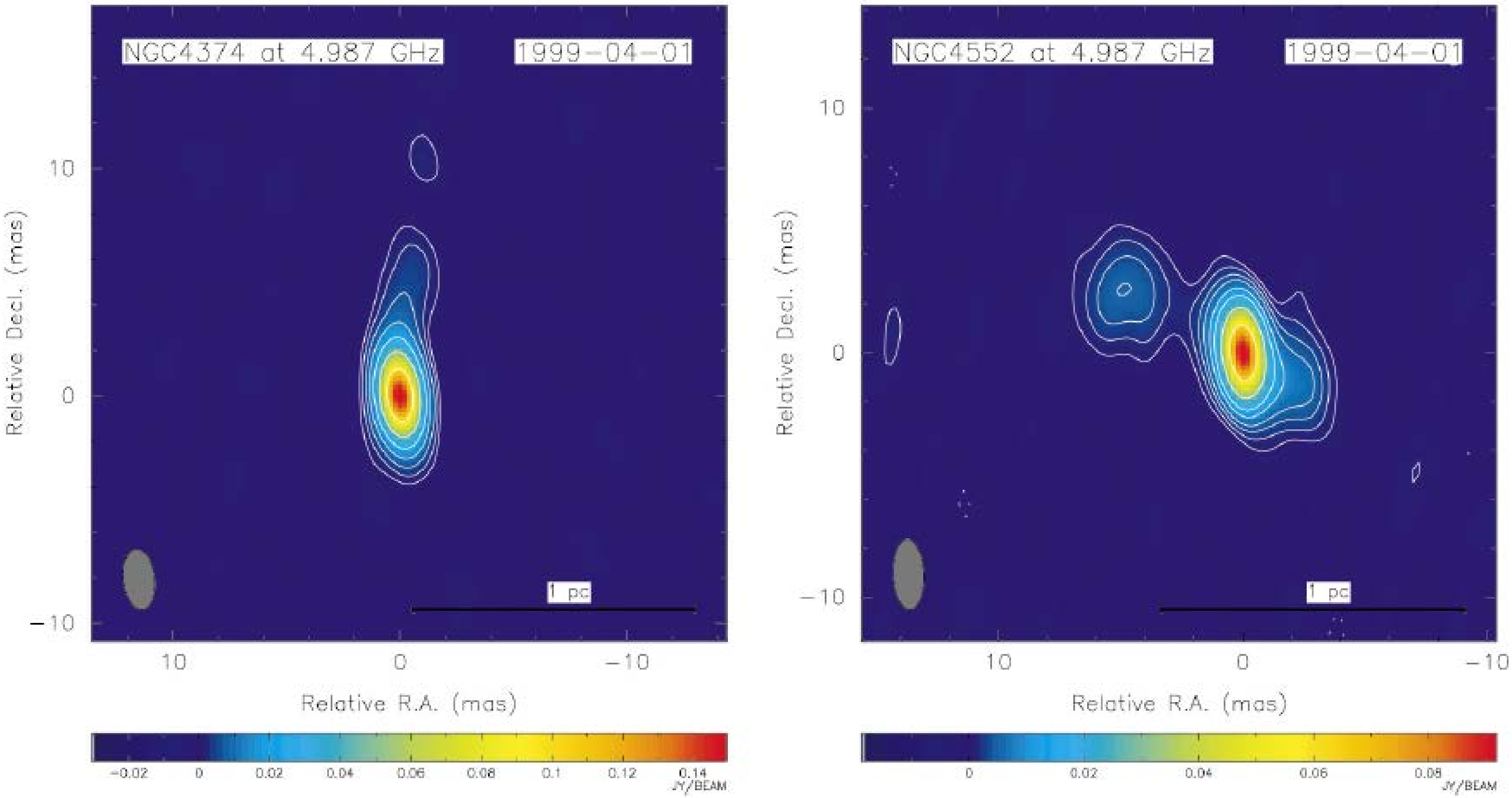

VLBA phase-referenced and self-calibrated maps of NGC 4374 (left) and 4552 (right) at 5 GHz.

Nagar et al. 2002

The low radiative output of LLAGN may be due to a low mass accretion rate, rather than a low radiative efficiency.

Jolley & Kuncic (2007) apply such a model to the well known LLAGN M87 and calculate the combined disk-jet steady-state broadband spectrum.
M87 may be a maximally spinning black hole accreting at a rate of $\sim 10^{-3} M_\odot \, yr^{-1}$.
This is about 6 orders of magnitude below the Eddington rate for the same radiative efficiency.
Furthermore, the total jet power inferred by our model is in remarkably good agreement with the value independently deduced from observations of the M87 jet on kiloparsec scales.

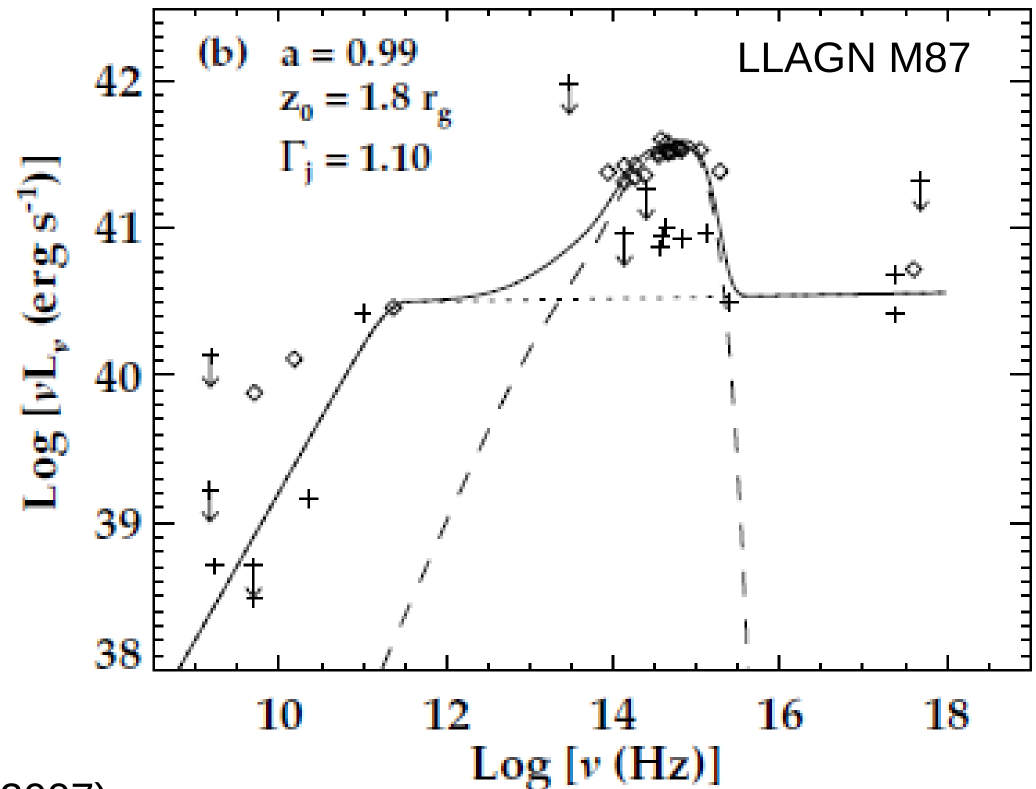

Jolley & Kuncic (2007)

Radio/equivalent X-ray luminosity correlation for a sample of jet-dominated AGN and XRBs. The X-ray flux has been adjusted to correspond to a black hole mass of 6 M□. The term equivalent X-ray flux denotes that this luminosity is extrapolated from the optical fluxes for some AGN sources (FR-I and Bl Lac objects). This extrapolation is motivated by the idea that one has to compare synchrotron emission.

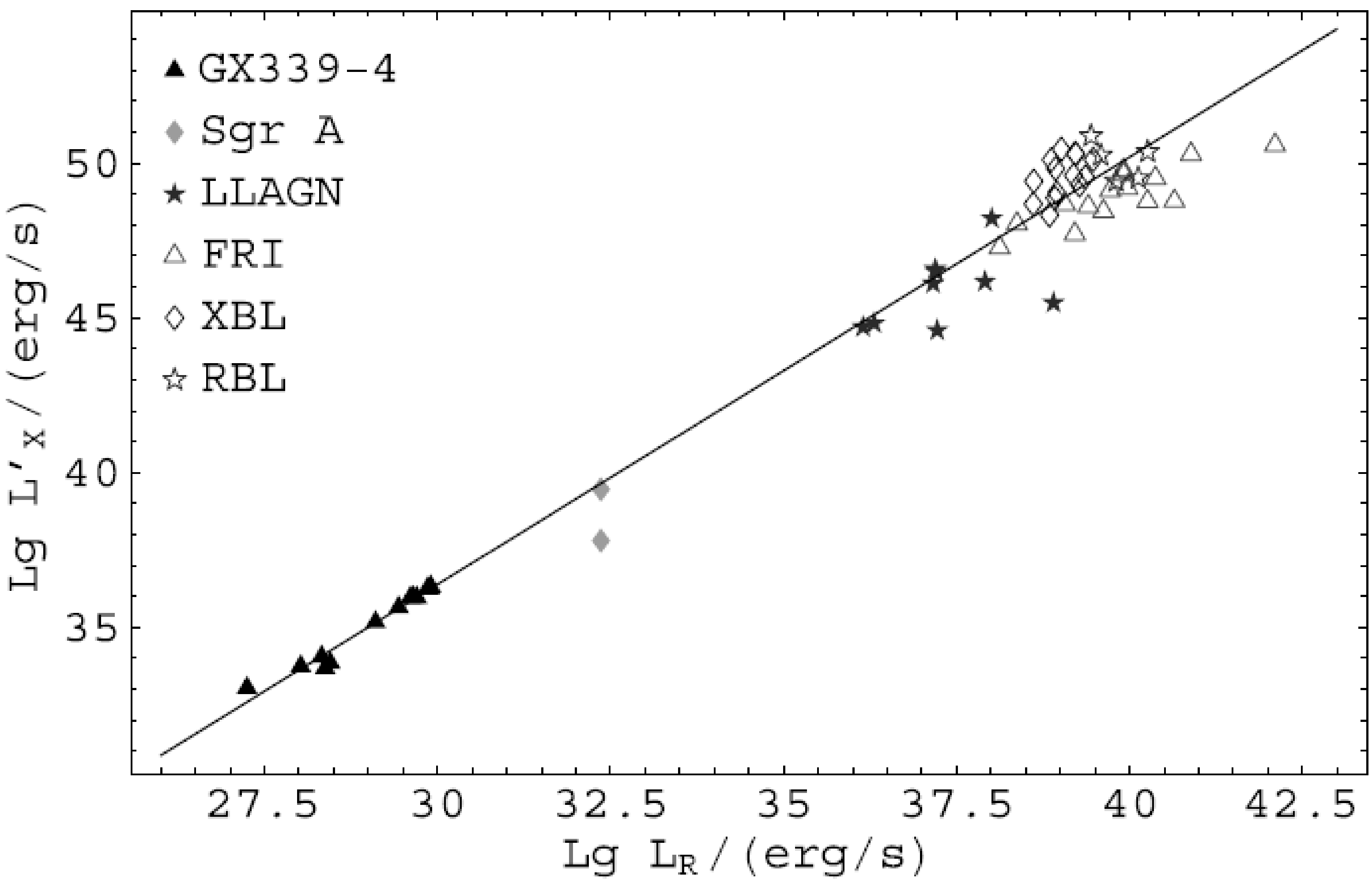

Körding & Falcke (2004)

Radio sources in the optical diagnostic diagram.

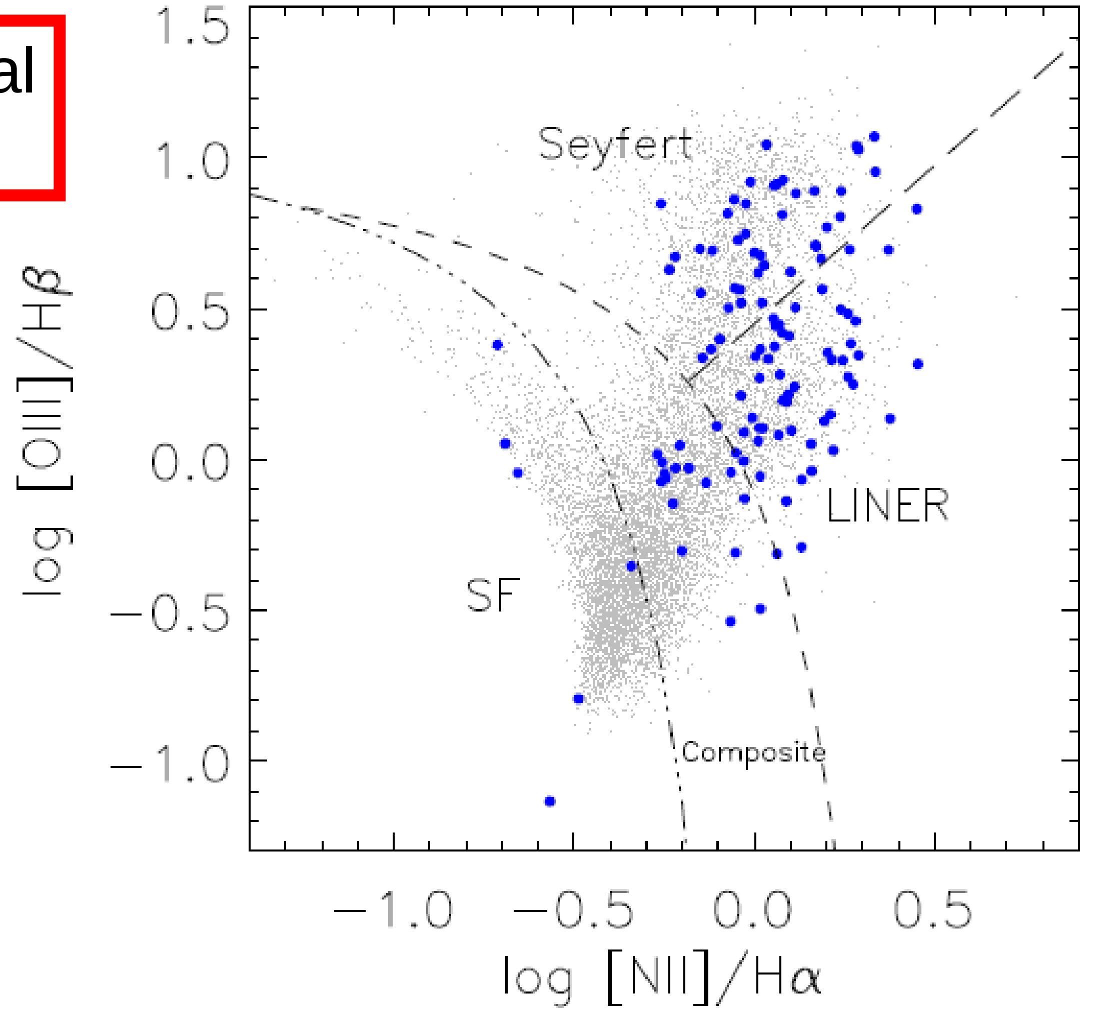

Vitale et al. 20012/15

[NII]-based diagnostic diagrams of the parent (gray) and Effelsberg (blue) samples. Demarcation lines were derived by Kewley et al. (2001; dashed) to set an upper limit for the position of starforming galaxies and by Kauffmann et al. (2003b; three-point dashed) to trace the observed lower left branch (purely star-forming galaxies) more closely. The dividing line between Seyferts and LINERs (long dashed) was set by Schawinski et al. (2007).

Radio spectral indices in the optical diagnostic diagram.

Red: flat/unverted
Blue: steep.

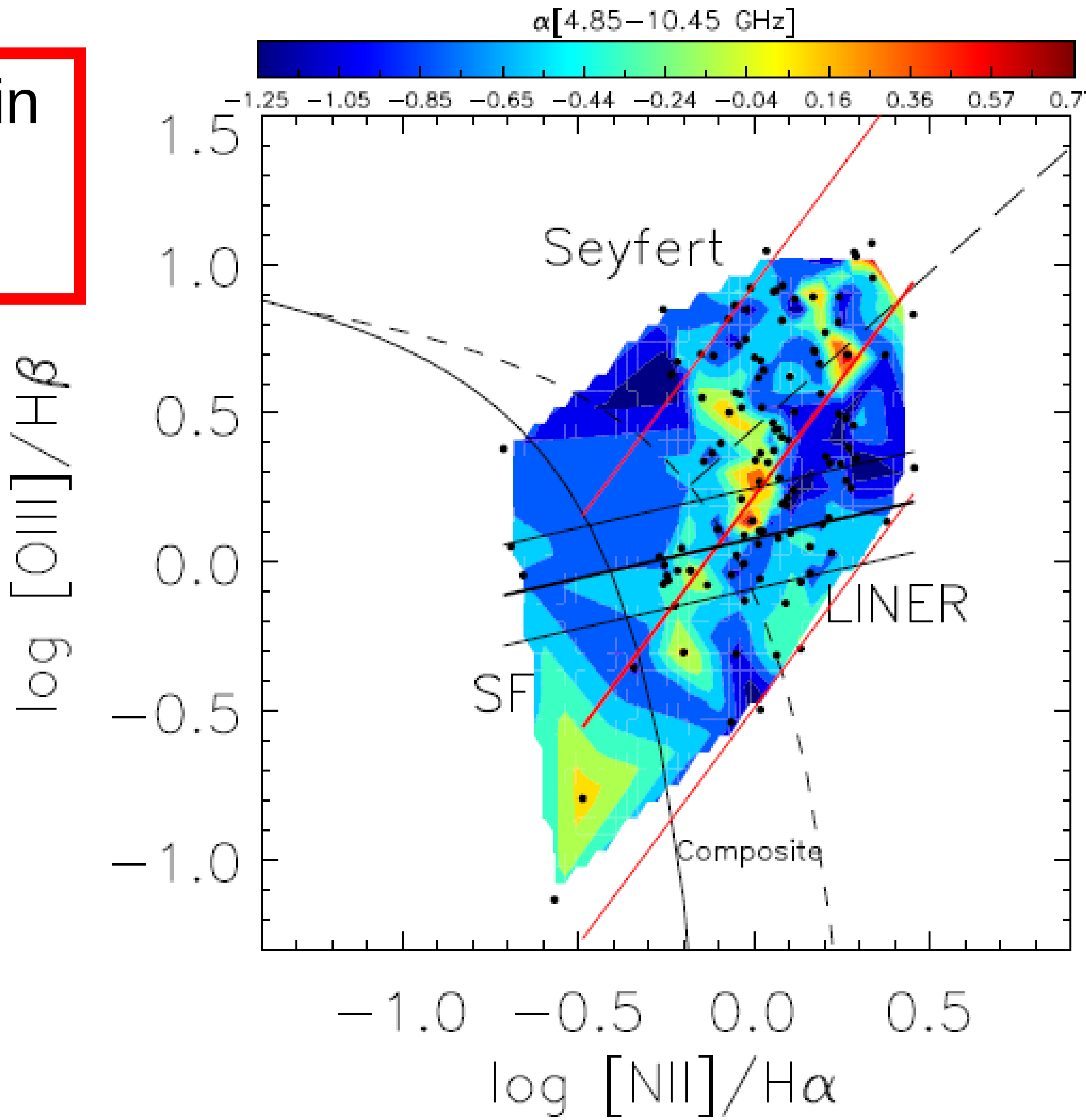

Vitale et al. 20012/15

Two-point spectral index distribution of the Effelsberg sample represented in the [NII] based diagnostic diagram. The color gradient indicates the spectral index values. Black dots correspond to sources positions in the diagram. Red thick lines are regression curves of the 15% most flat- and inverted-spectrum sources; black thick lines are regression curves of the steep-spectrum sources

Mass increase of Radio LLAGN in the optical diagnostic diagram.

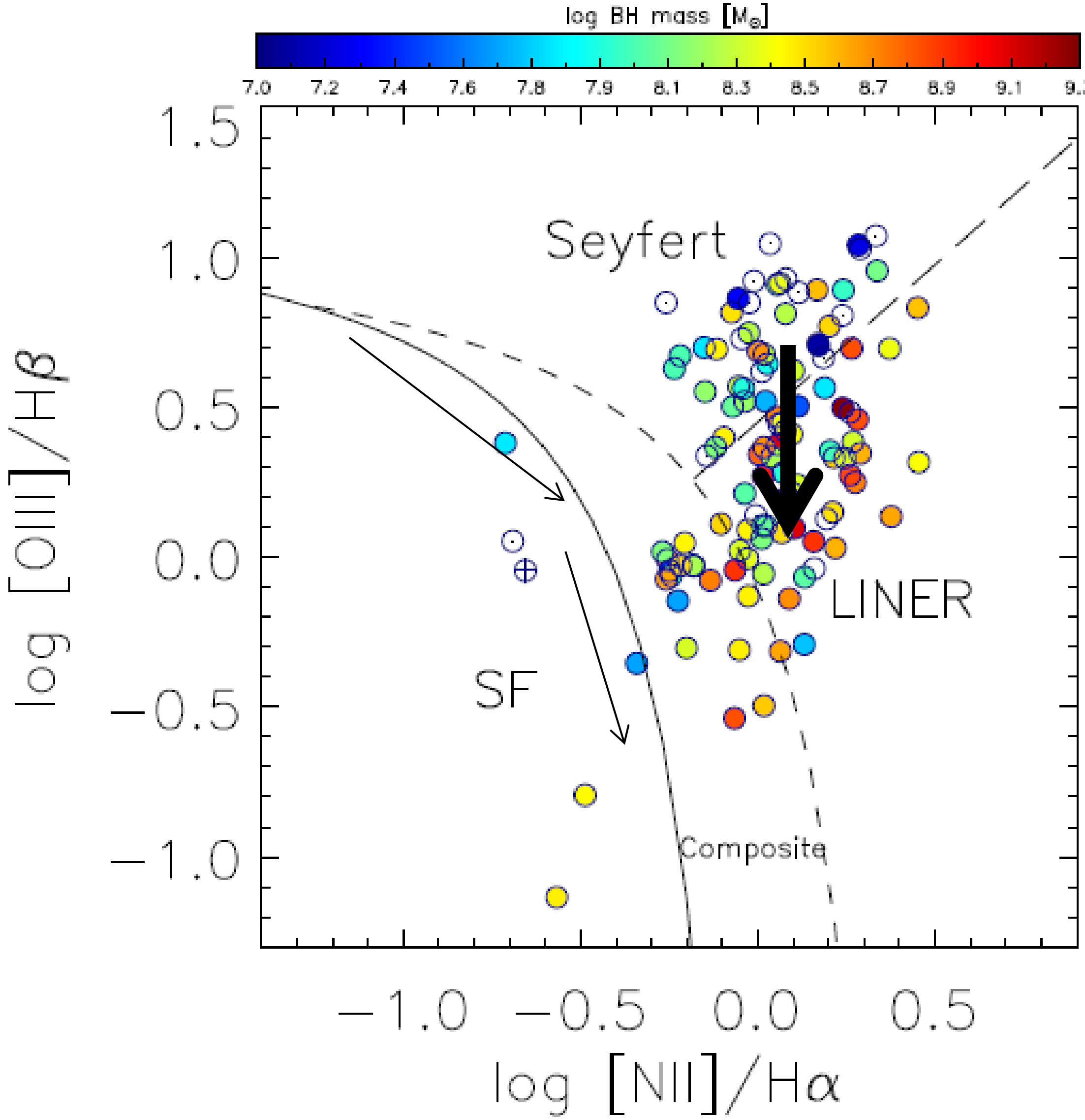

Vitale et al. 20012/15

Black hole masses distribution in the [NII]-based diagram. The color bar indicates MBH in solar masses. White circles indicate sources where the SDSS measurement of the stellar velocity dispersion is not accurate. The crossed circle again indicates an unreliable measurement, not flagged in the SDSS catalog.

Mass increase of Radio LLAGN in the optical diagnostic diagram.

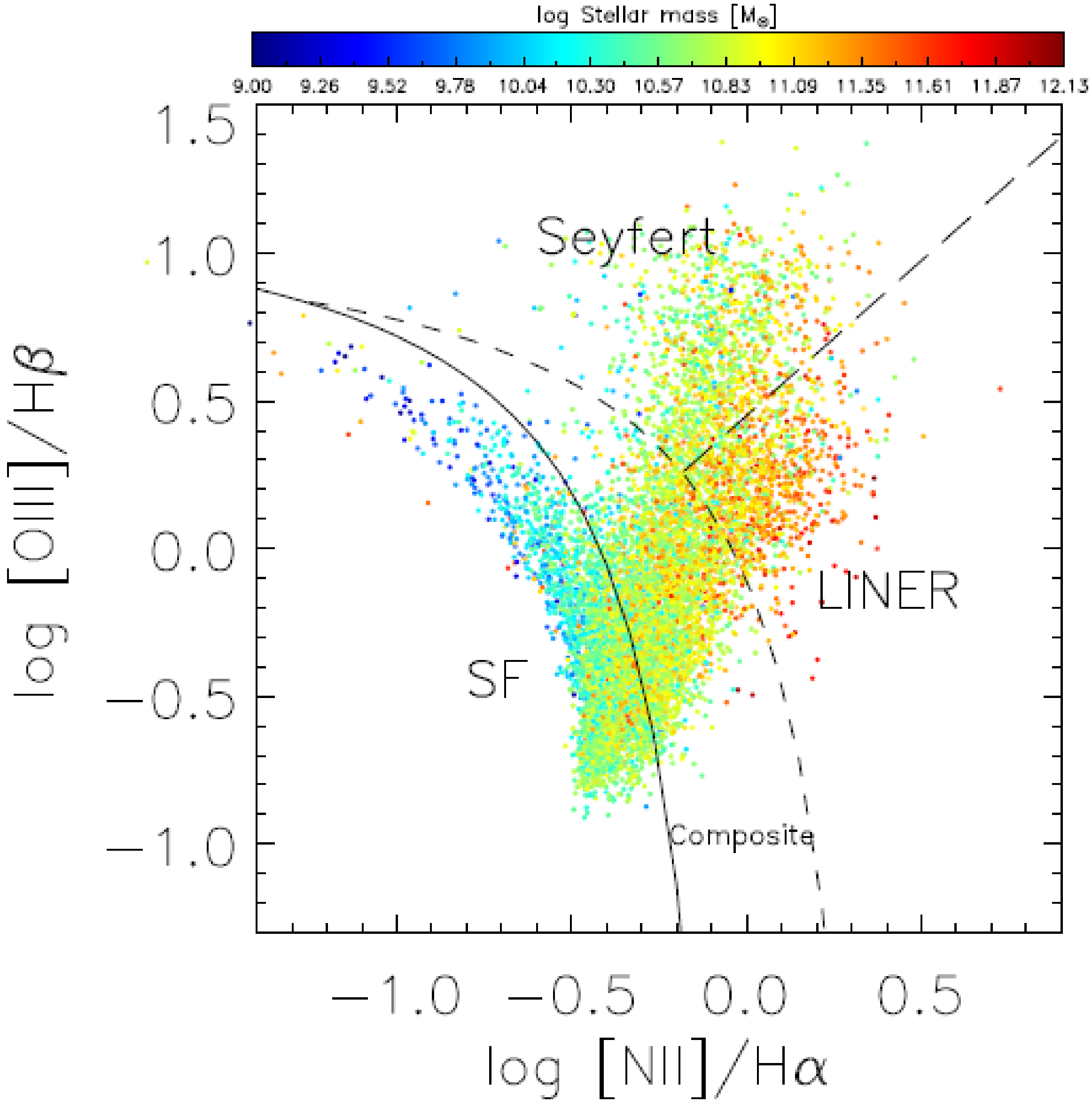

Vitale et al. 20012/15

SDSS-FIRST stellar mass distribution in the [NII]-based diagnostic diagram. The color bar indicates the stellar mass values from SDSS measurements, in solar units.

Possible Evolution of Radio LLAGN in the optical diagnostic diagram.

Vitale et al. 20012/15

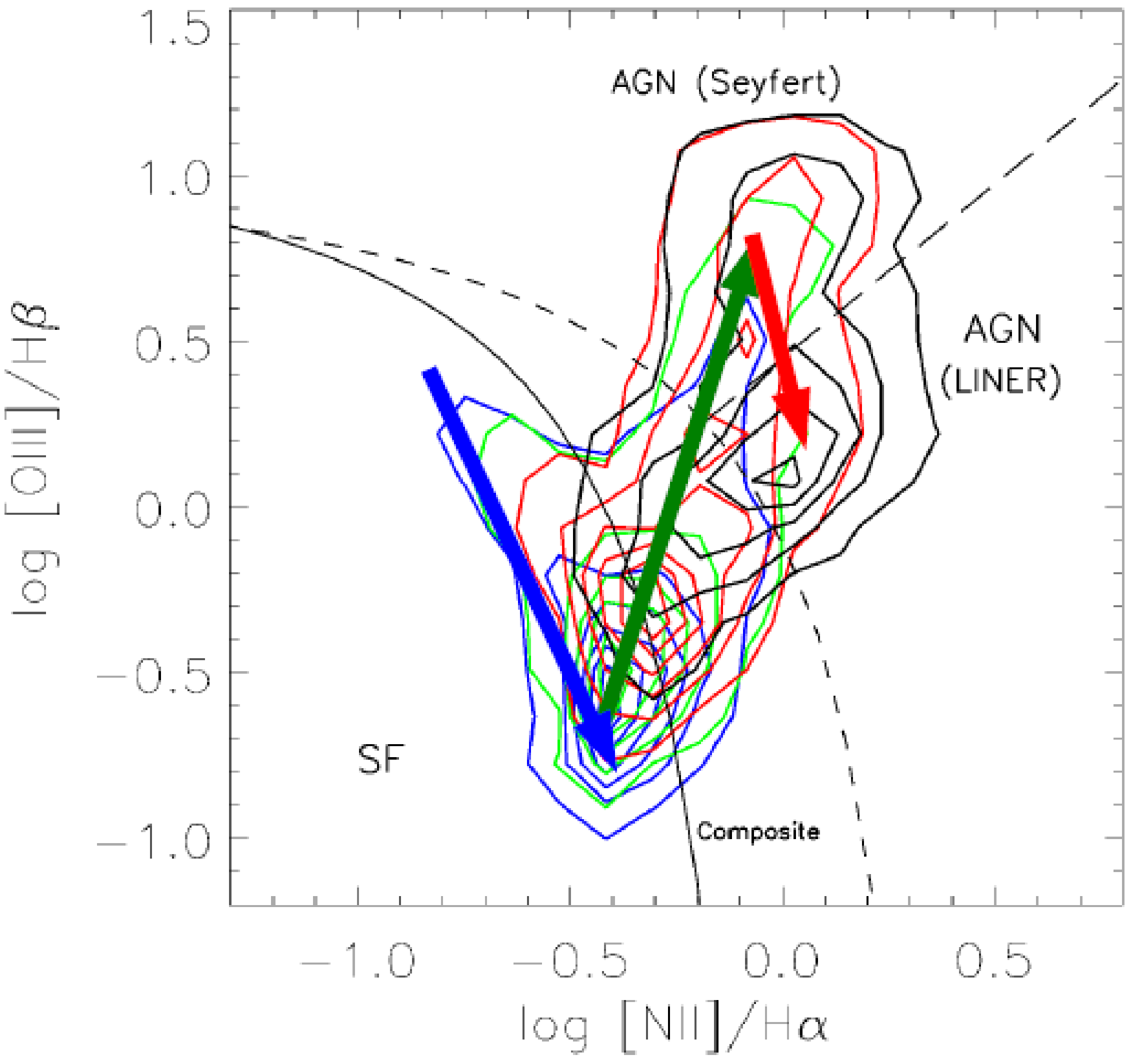

Sketch of galaxy evolution across the [NII]-based diagnostic diagram. Color contours represent sub-samples of the parent sample with increasing values (blue, green, red, and black) of the ratio between radio luminosity and luminosity of the H-line as in Vitale et al. (2012). The arrows represent the trend of possible galaxy evolution from starforming galaxies to Seyferts and LINERs.

SgrA* and its Environment

Orbits of High Velocity Stars
in the Central Arcsecond

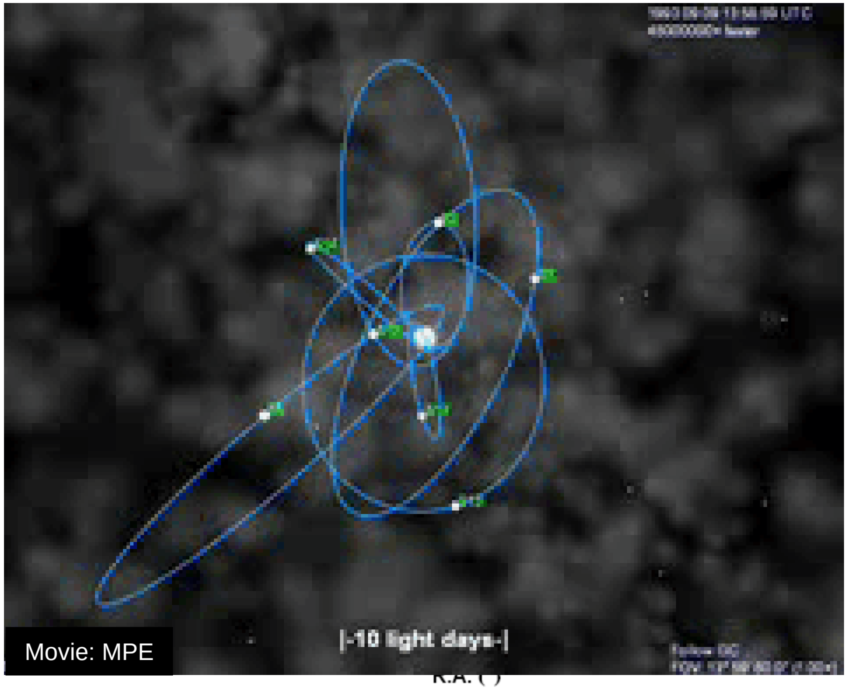

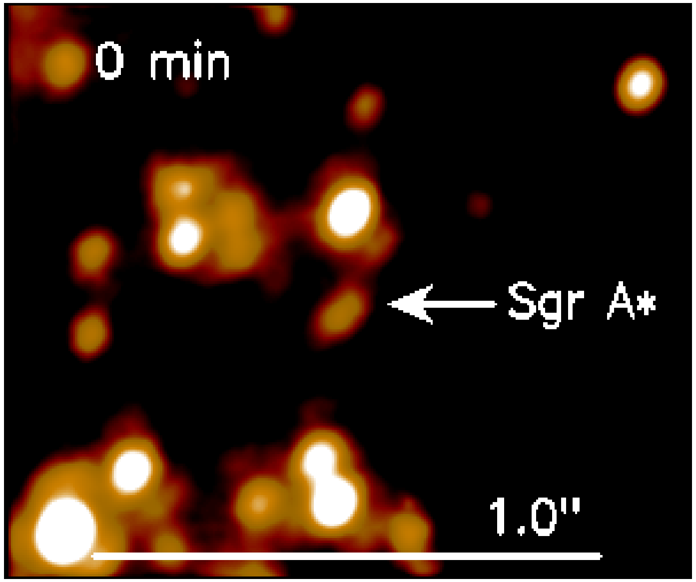

Eckart & Genzel 1996/1997 (first proper motions)
Eckart+2002 (S2 is bound; first elements)
Schödel+ 2002, 2003 (first detailed elements)
Ghez+ 2003 (detailed elements)
Eisenhauer+ 2005, Gillessen+ 2009
(improving orbital elements)
Rubilar & Eckart 2001, Sabha+ 2012, Zucker+2006
(exploring the relativistic character of orbits)

~4 million solar masses
at a distance of
~8+-0.3 kpc

Accretion of winds onto SgrA*

Starvation?

NIR and X-ray observations as well as simulations suggest stellar winds contribute up to 10^-4 MSun/yr at Bondi radius (10^5 rS) (Krabbe+ 1995, Baganoff+ 2003)

At this accretrion rate SgrA* is 10^7 times under luminous (e.g. Shcherbakov & Baganoff 2010)

Accretion of gaseous clumps from the Galactic Centre Mini-spiral onto Milky Way's supermassive black hole ? (Karas, Vladimir; Kunneriath, Devaky; Czerny, Bozena; Rozanska, Agata; Adhikari, Tek P. ; 2016grg..conf...98K)

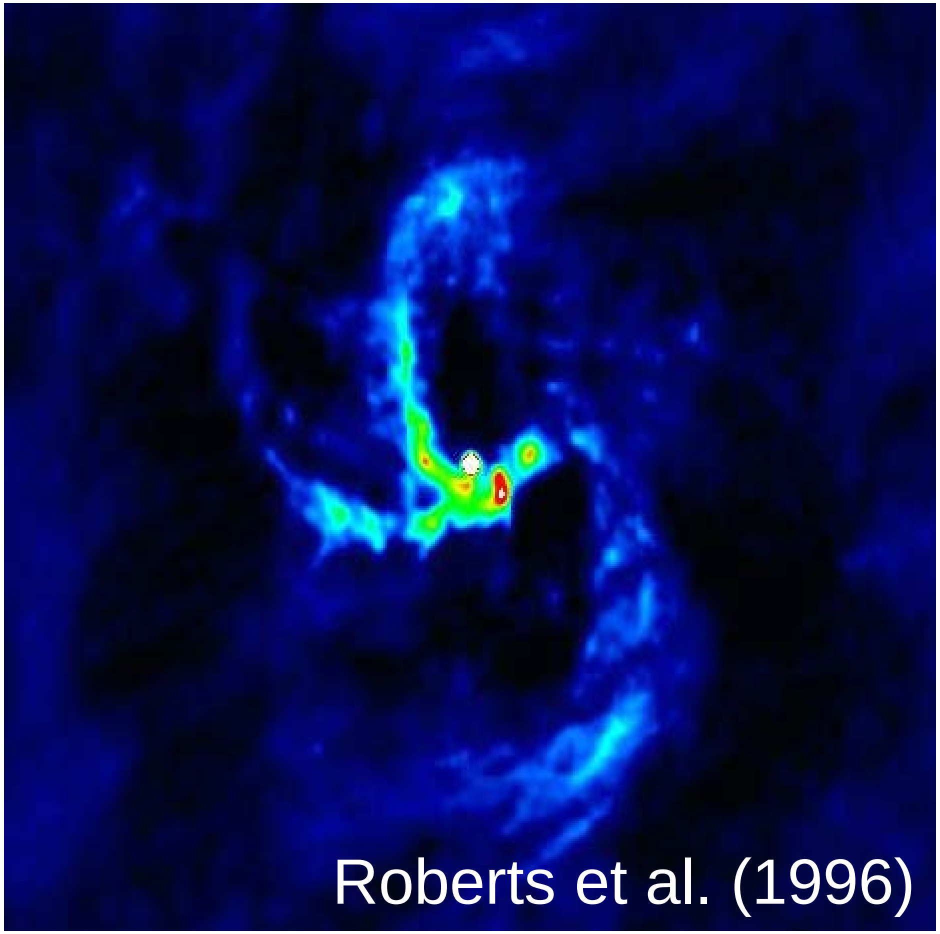

Adiabatic Expansion in SgrA*

$$\nu_m = \nu_{m0}\left(\frac{R(t)}{R_0}\right)^{-(4p+6)/(p+4)}$$

van der Laan (1966)

$$p = 1 - 2\alpha_{sync} \sim 2.4,$$

$$\frac{R(t)}{R_0} \sim \left(\frac{\nu_m}{\nu_{m0}}\right)^{-1/2.44} \sim \left(\frac{100\,\mathrm{GHz}}{350\,\mathrm{GHz}}\right)^{-1/2.44} \approx 1.67$$

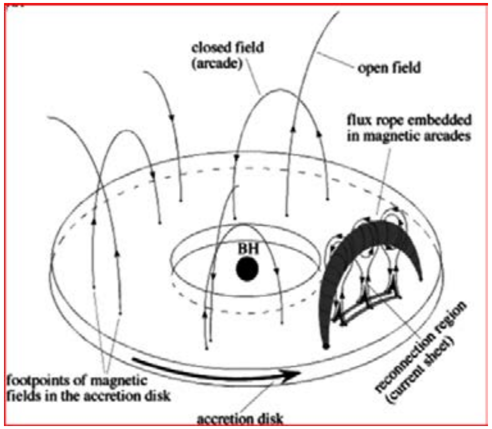

Yuan et al. 2009

$$R(t) = v_{exp}t + R_0$$

starting at ~1 Rs

$$v_{exp} \times 0.5\,\mathrm{h} \sim 0.67\,R_S.$$

$$v_{exp} \sim 0.01\,\mathrm{c}$$

Subroweit et al. 2016 submitted

Radiative Models of SGR A* from GRMHD Simulations

MOTION IN
OR CLOSE TO
THE MIDPLANE

relativistic effects
may become
observable here

Accretion of matter onto SgrA* results in a variable spectrum

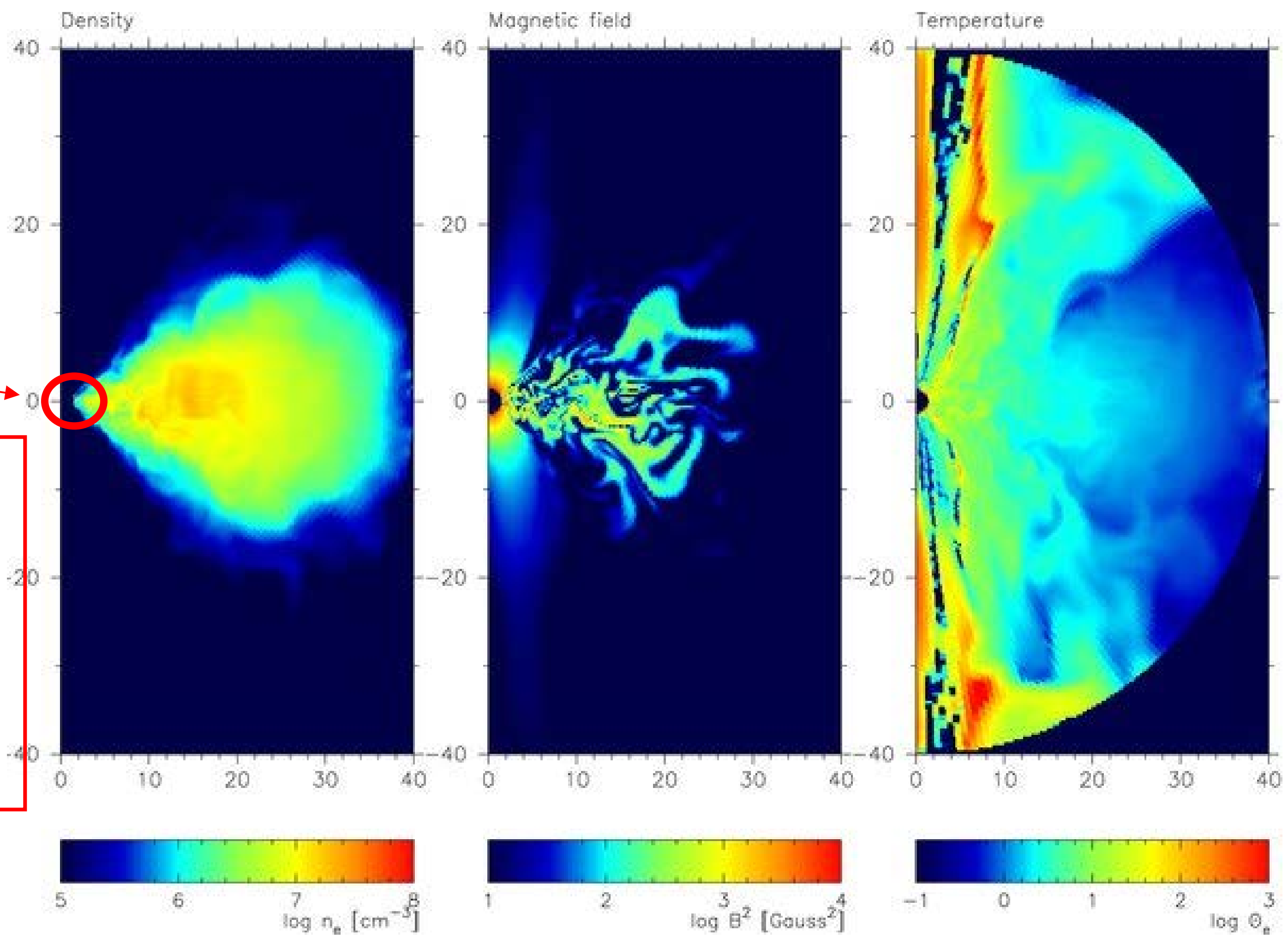

Mościbrodzka+ 2010, 2009
Dexter+ 2010

Flare Emission from SgrA*

Recent work on SgrA* variability

Radio/sub-mm:

Mauerhan+2005, Marrone+2006/8, Yusef-Zadeh+2006/8 and may others

X-ray:

Baganoff+2001/3, Porquet+2003/2008, Eckart+2006/8, and several others

NIR:

Genzel+2003, Ghez+2004, Eckart+2006/9, Hornstein+2007,Do+2009, and many others

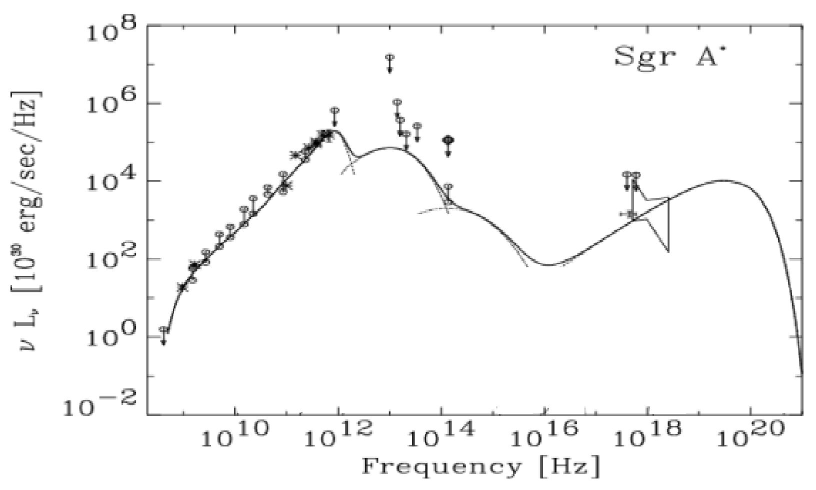

Multi frequency observing programs:

Genzel, Ghez, Yusef-Zadeh, Eckart and many others

Questions:

- What are the radiation mechanisms?
- How are the particles accelerated?
- (How) Are flux density variations at different wavelength connected to each other?

Possible flare scenarii

Possible flare models

NIR X-ray

SYN-SYN: Synchrotron-synchrotron

SYN-SSC: Synchrotron-Self-Compton

SSC-SSC: Self-Compton-self-Compton

Parametrization of the logarithmic expression

Two extreme cases:
High demands on electron acceleration or density

SYN-SYN: X-ray produced by synchrotron radiation;
<10% by SSC

SSC-SSC: X-ray produced by synchrotron self-Compton;
<10% by SYN; required density higher than average

Moderate demand on density and acceleration

SYN-SSC: radio/NIR by Syncrotron and X-ray by SSC

Radiative Models of SGR A* from GRMHD Simulations

In the mid-plane the vertical particle distribution is well described by a Gaussian, with a dimensionless scale height of about 0.1-0.3 (1 σ).

DENSITIES CLOSE TO THE MIDPLANE WILL BE HIGHER THAN AVERAGE

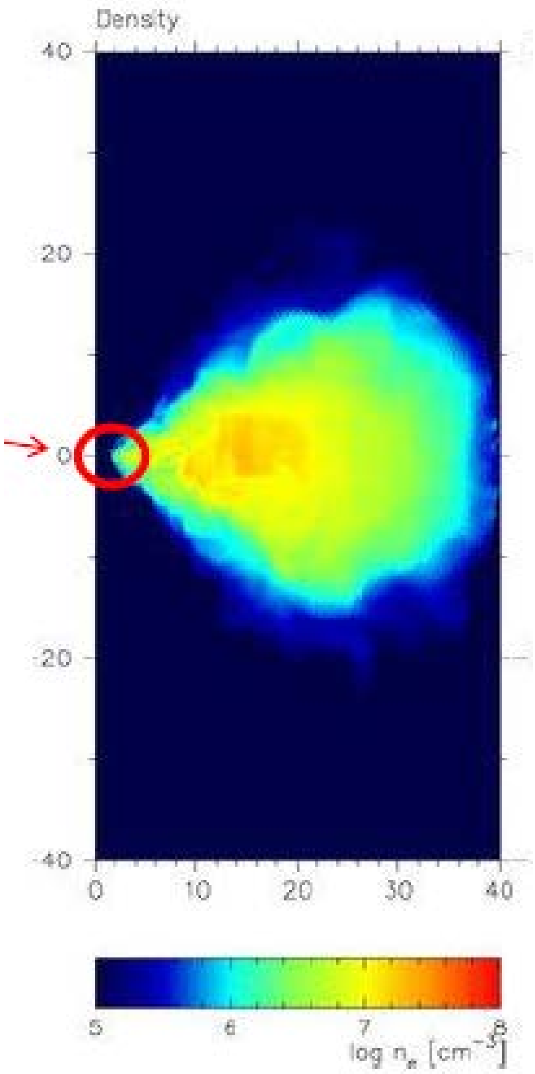

However, the thickness (and hence the mid-plane density) is mostly determined by the initial conditions and energy evolution methods used in the simulations rather than by the physics of the accretion flow.

Collisionless Shocks

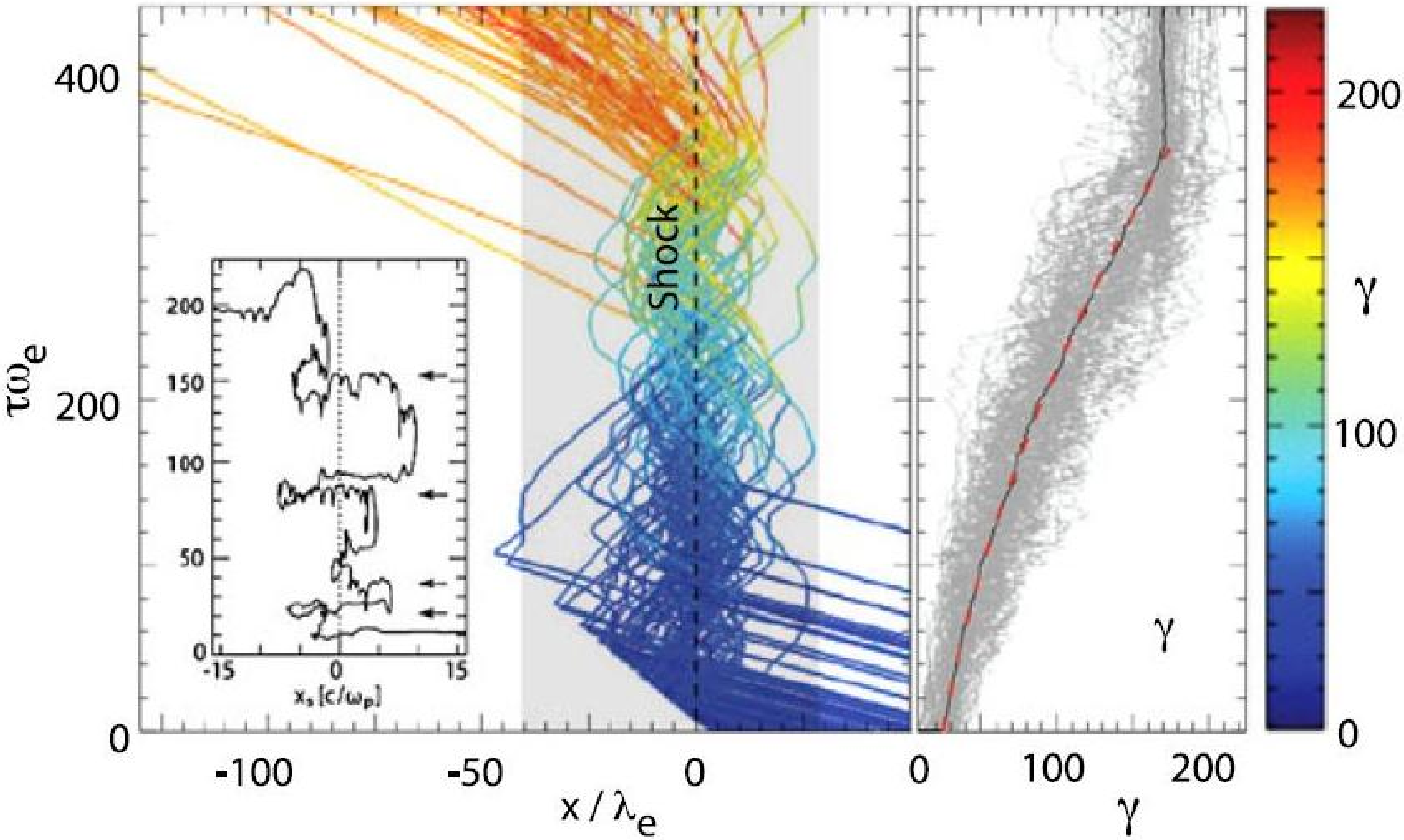

Left: Time-evolution of the orbits of the 80 most energetic ions in a non-magnetized relativistic shock simulation with Γ = 20. The particles are coming from the upstream flow, are back-scattered and accelerated in the magnetic turbulence in the shock transition, staying within the distance of an ion inertial length λi ≈ 50λe.

Bykov & Treumann, 2011, Astr. Astro. Rev. 19, 42

Radiative Models of SGR A* from GRMHD Simulations

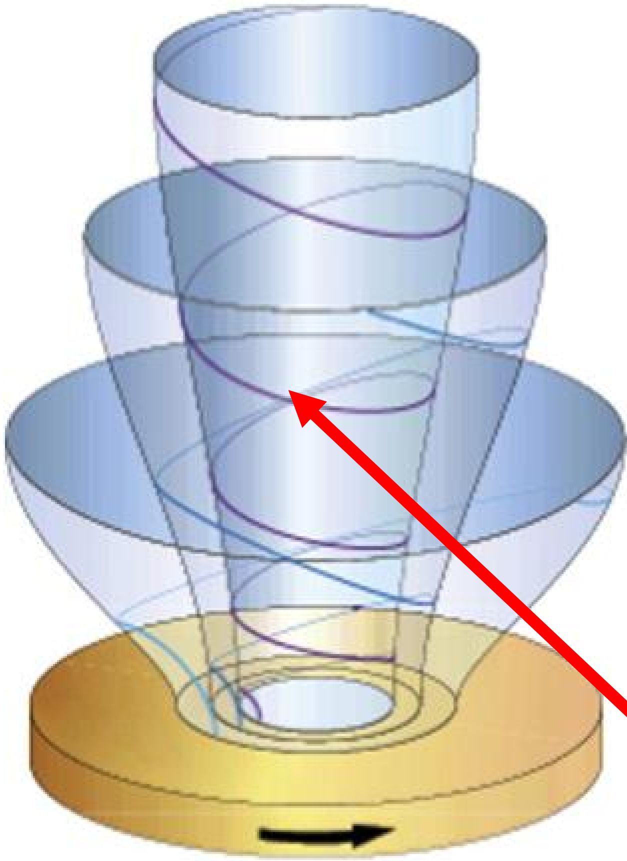

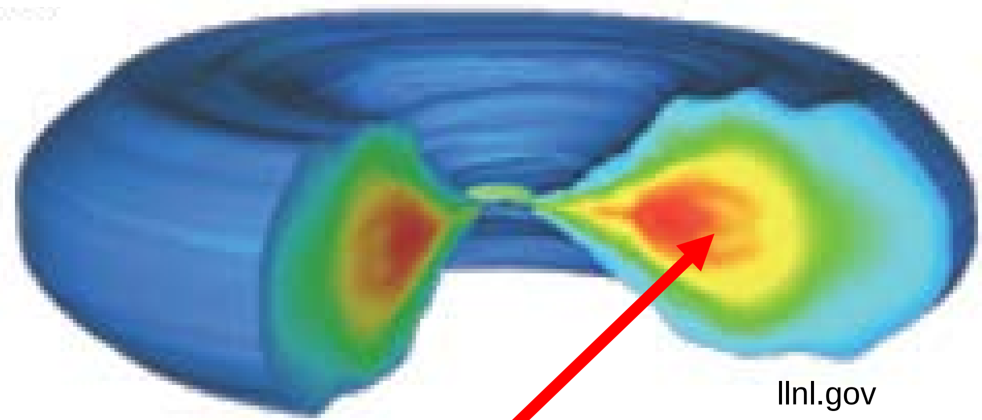

llnl.gov

Possible locations of electron accelerating collisionles shocks in the immediate vicinity of SgrA*.

Jonathan Ferreira, Remi Deguiran,
High Energy Density Physics
Volume 9, Issue 1, March 2013, Pages 67–74

Variability in the SYN-SSC case

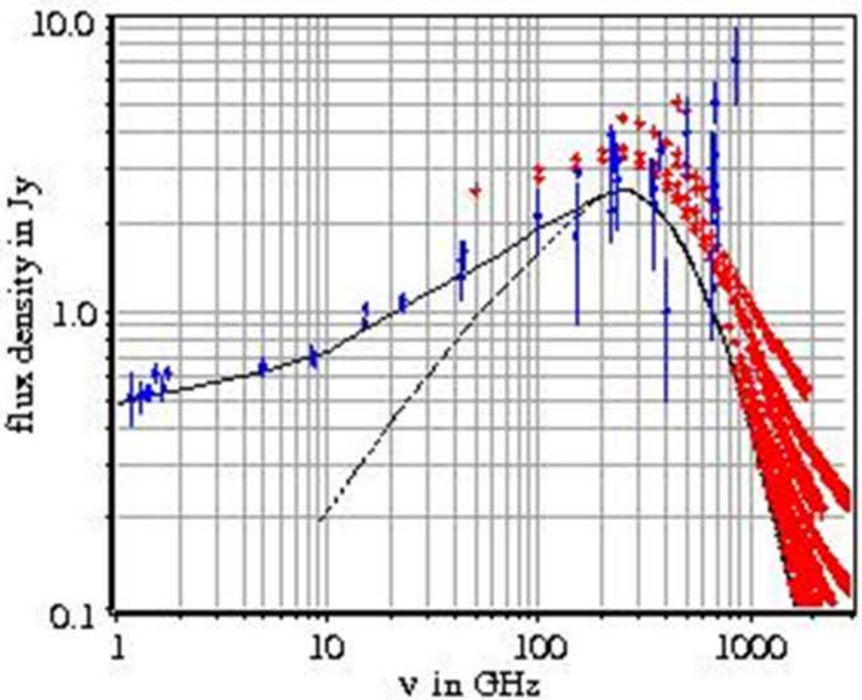

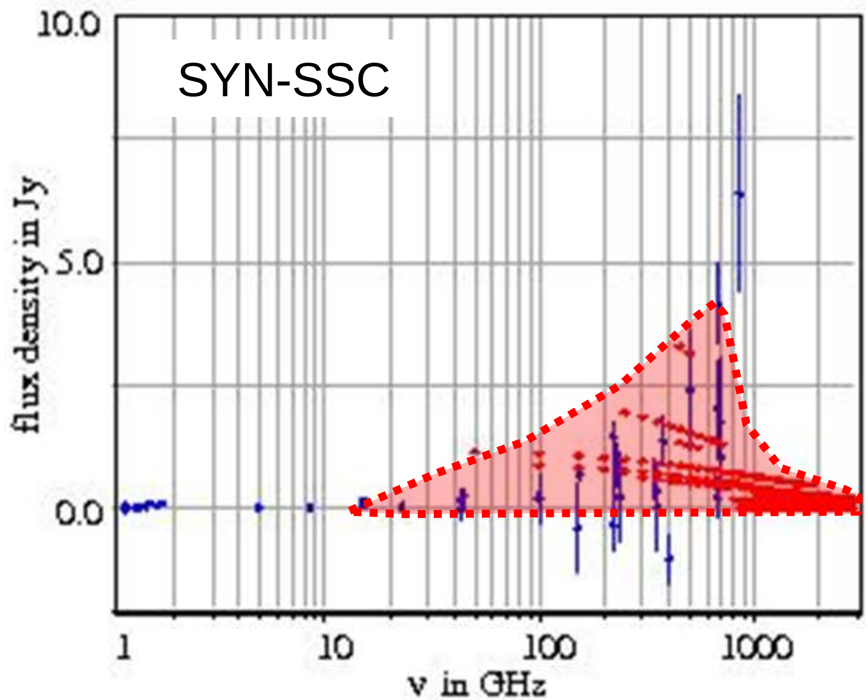

SYN-SSC: Density moderate
consistent with MHD model of mid-plane
Moderate demand on electron acceleration

Eckart et al. 2012

Flare Activity of SgrA*

Seeing the effect of ongoing accretion

Observations

SgrA* on 3 June 2008:
VLT L-band and APEX
sub-mm measurements

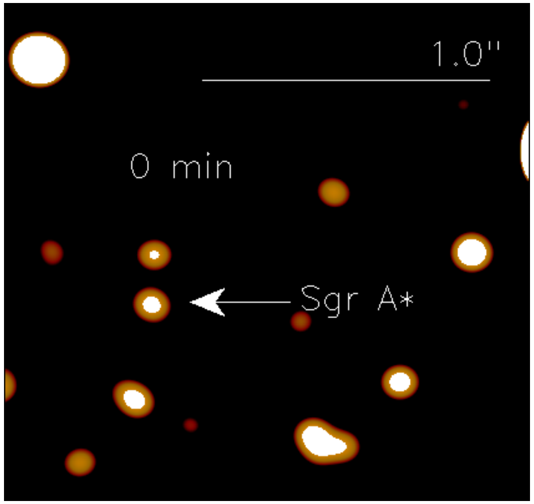

VLT 3.8um L-band

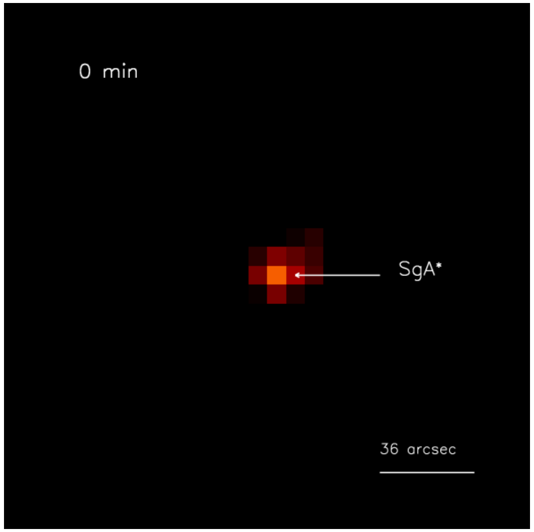

APEX 1.3 mm

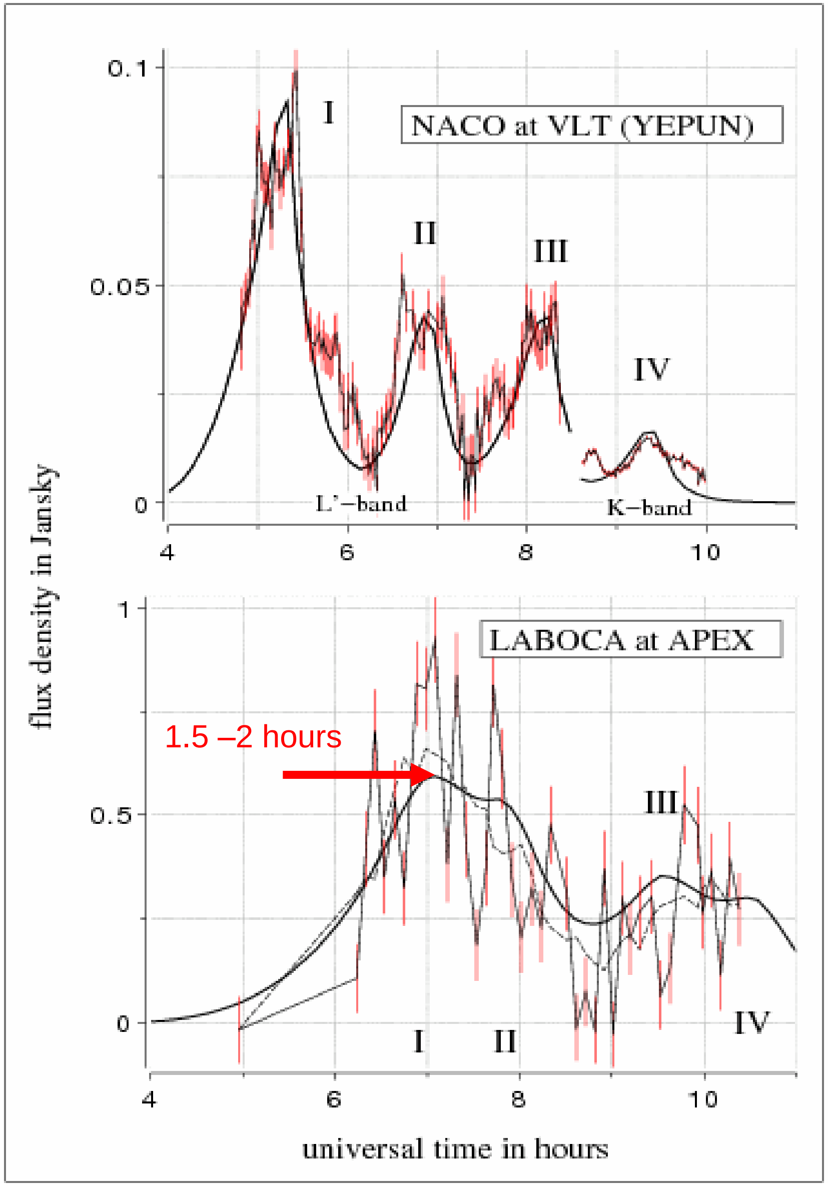

Eckart et al. 2008; A&A 492, 337
Garcia-Marin et al.2009

Simultaueous NIR/X-ray Flare emission 2004

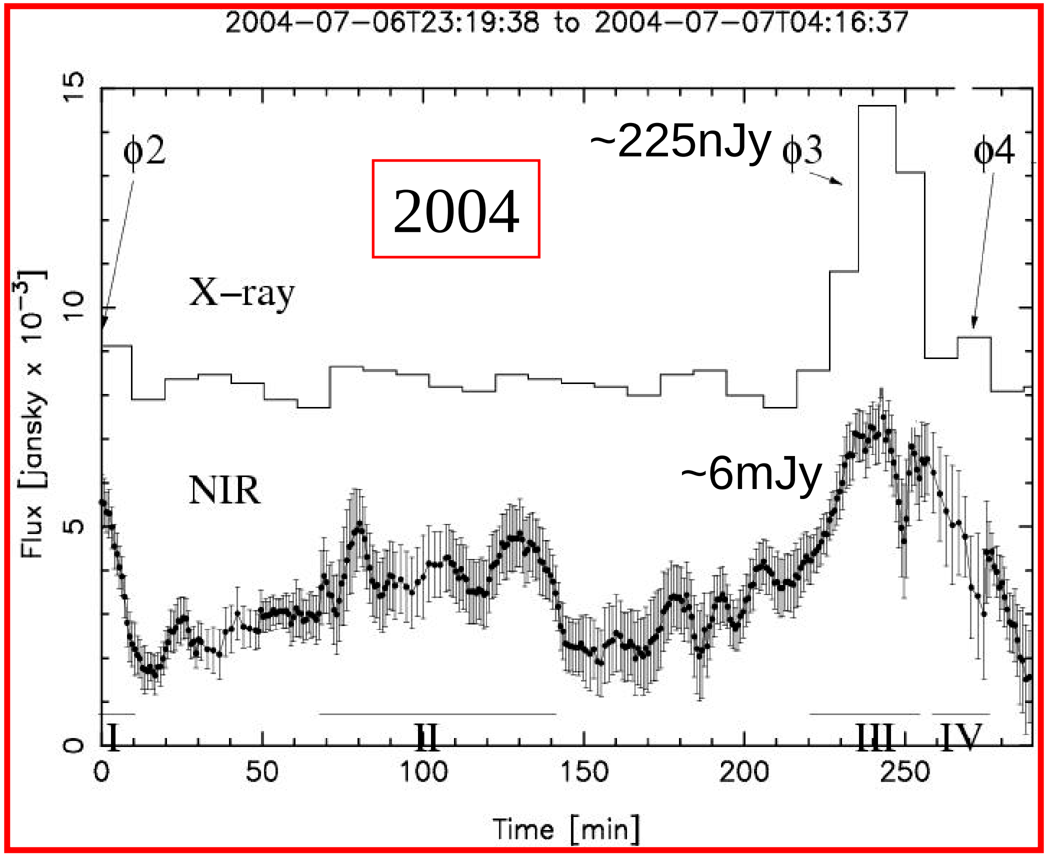

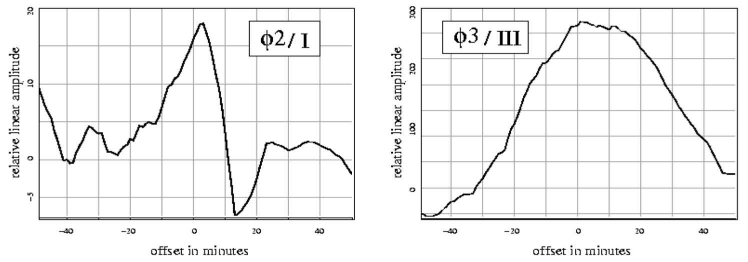

Time lags are less <10-15 minutes

NIR and X-ray flares are well correlated.

Flare emission originates from within <10mas form the position of SgrA*

First simultaneous NIR/X-ray detection

2003 data: Eckart, Baganoff, Morris, Bautz, Brandt, et al. 2004 A&A 427, 1

2004 data: Eckart, Morris, Baganoff, Bower, Marrone et al. 2006 A&A 450, 535

see also Yusef-Zadeh, et al. 2008, Marrone et al. 2008

Bright He-stars provide mass for accretion

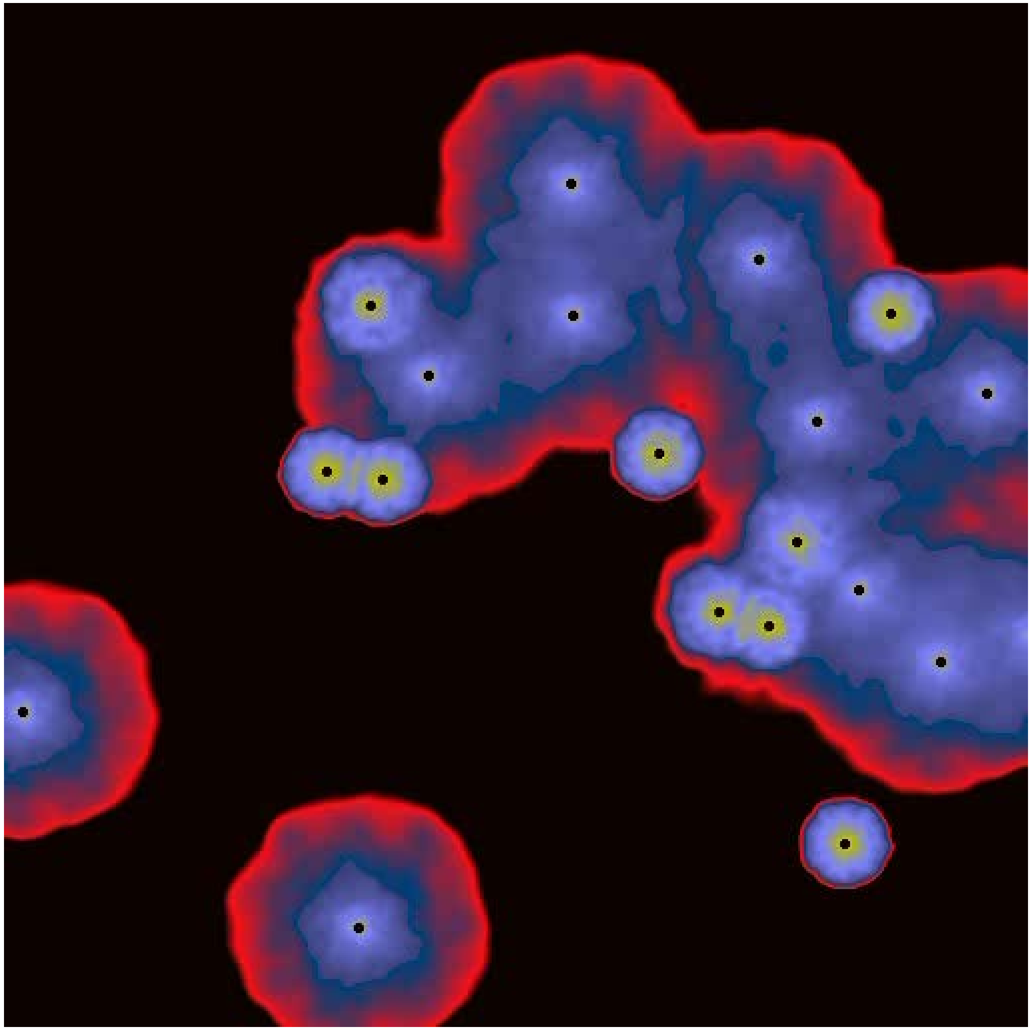

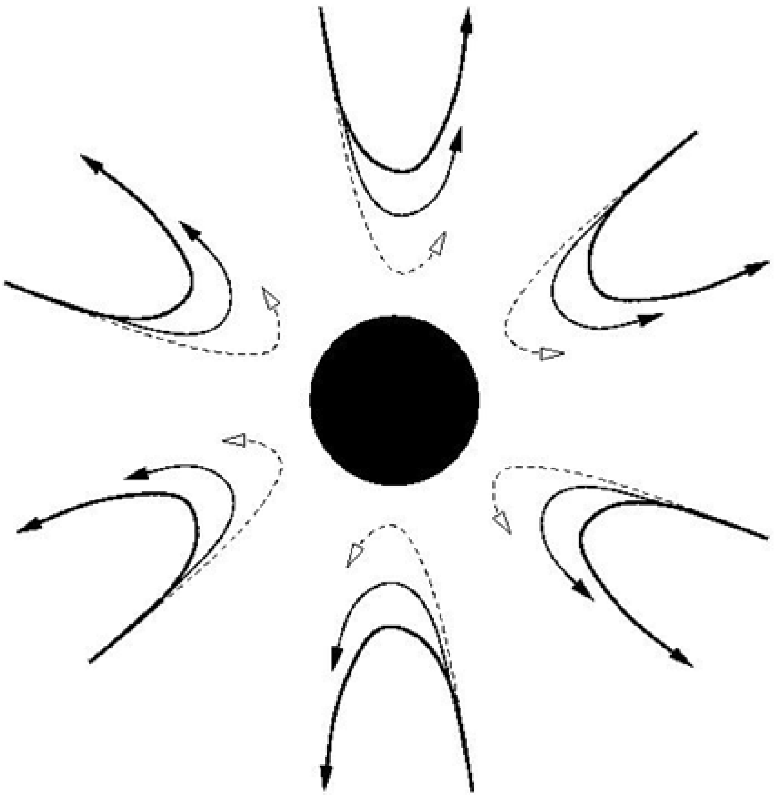

radius dependent
accretion

Cuadra, Nayakshin, Springel, and Di Matteo 2005/6

Shcherbakov & Baganoff ApJ, 2010

VLBI Imaging and Polarization SgrA*

Imaging the effect of ongoing accretion

VLBI at 230 GHz (1.3 mm wavelength)

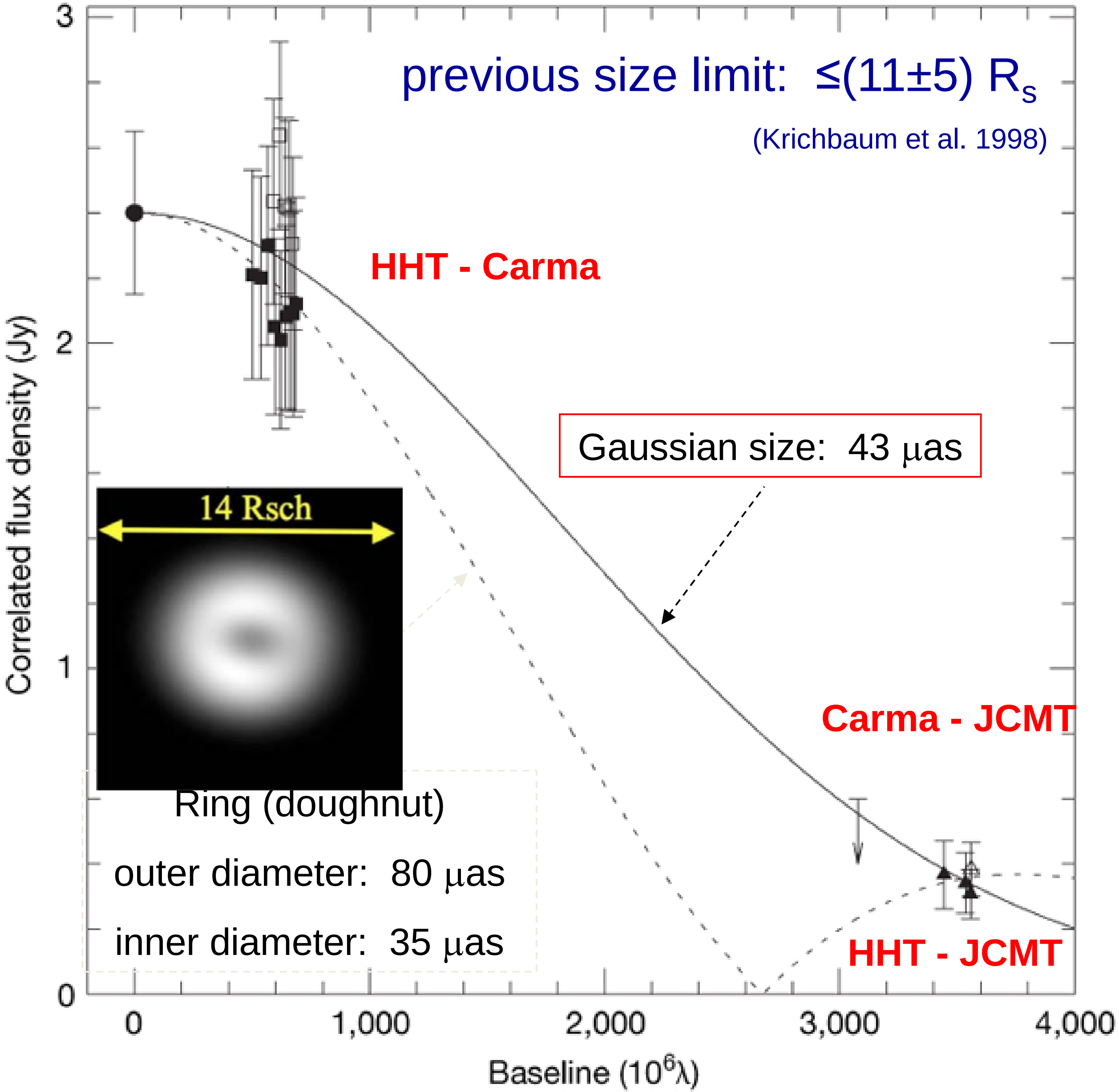

Doeleman *et al. Nature* **455**, 78-80 (2008)

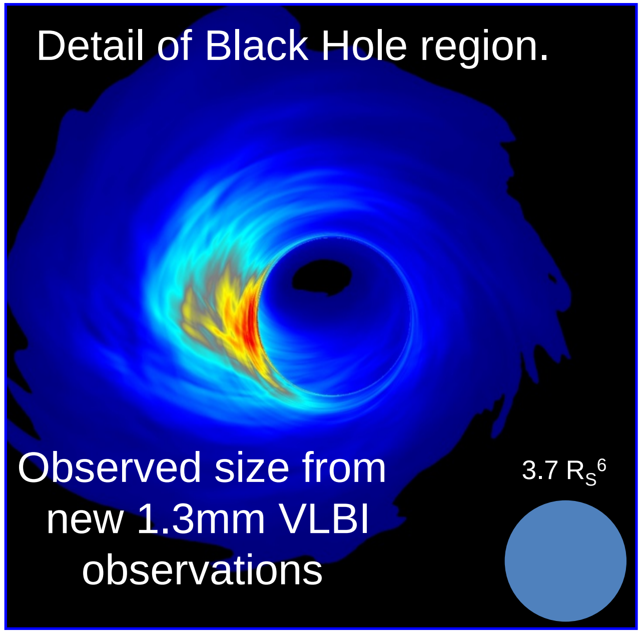

observed size:

43 (+14/-8) μas

deconvolved :

37 μas (3.7 R_S)

1.3mm VLBI Visibility of the Variable Source SgrA*

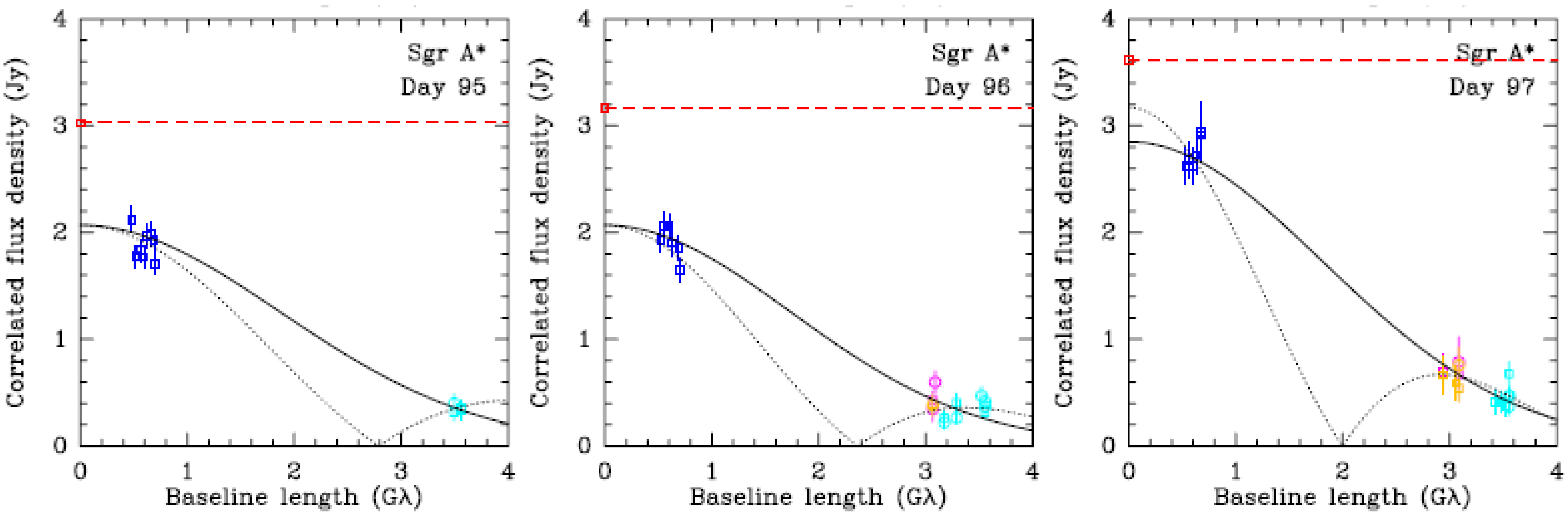

The Astrophysical Journal Letters, 727:L36 (6pp), 2011 February 1
doi:10.1088/2041-8205/727/2/L36

1.3 mm WAVELENGTH VLBI OF SAGITTARIUS A*: DETECTION OF TIME-VARIABLE EMISSION ON EVENT HORIZON SCALES

Vincent L. Fish[1], Sheperd S. Doeleman[1], Christopher Beaudoin[1], Ray Blundell[2], David E. Bolin[1,3], Geoffrey C. Bower[4], Richard Chamberlin[5], Robert Freund[6], Per Friberg[7], Mark A. Gurwell[2], Mareki Honma[8], Makoto Inoue[9], Thomas P. Krichbaum[10], James Lamb[11], Daniel P. Marrone[12,14], James M. Moran[2], Tomoaki Oyama[8], Richard Plambeck[4], Rurik Primiani[2], Alan E. E. Rogers[1], Daniel L. Smythe[1], Jason SooHoo[1], Peter Strittmatter[6], Remo P. J. Tilanus[7,13], Michael Titus[1], Jonathan Weintroub[2], Melvyn Wright[4], David Woody[11], Ken H. Young[2], and Lucy M. Ziurys[6]

Fish et al. 2011

VLBI Image Reconstruction for SgrA*

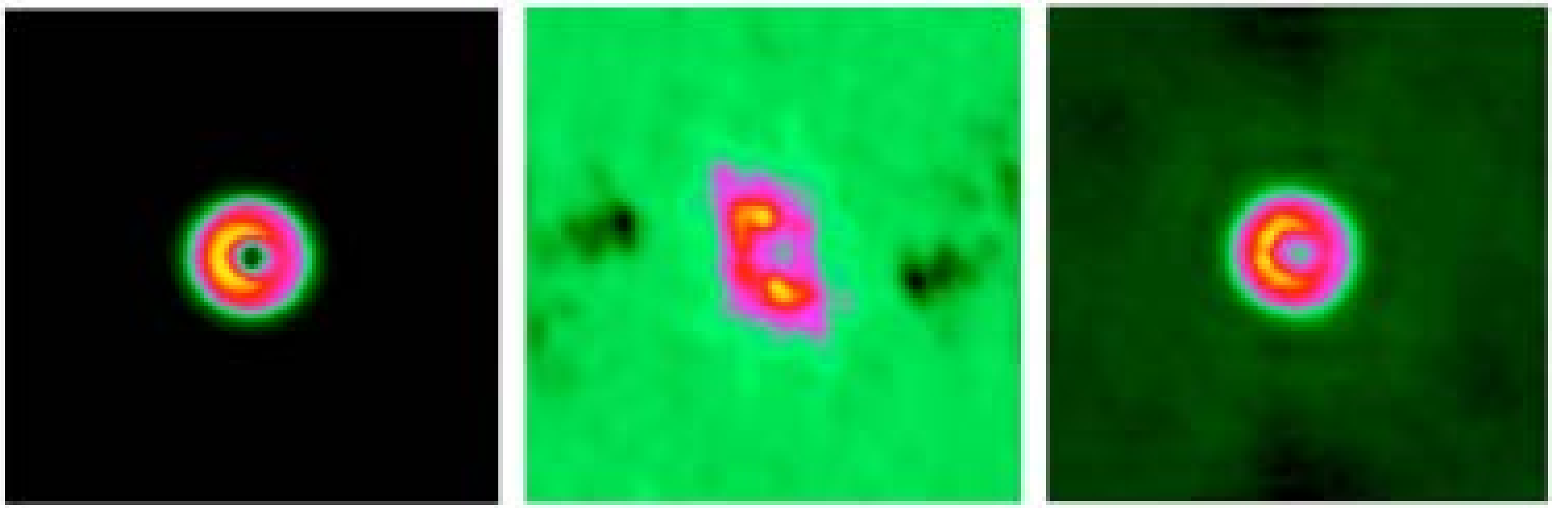

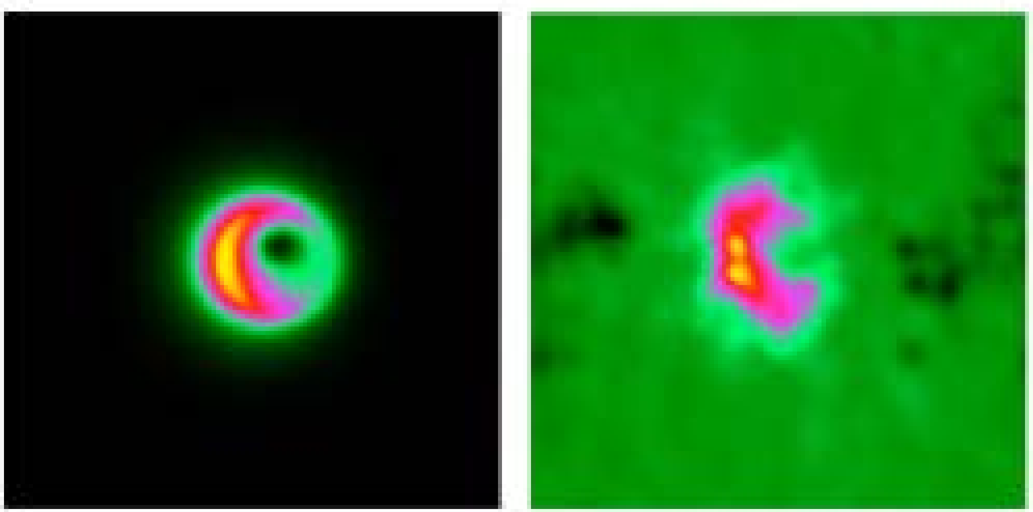

Figure 3: *0.8mmλ VLBI imaging simulations of Sgr A*. The left-most images are models that have been scatter broadened by ISM effects. The middle panels show images reconstructed using a 7-station array that could reasonably be scheduled within 3-5 years. The right panels show images reconstructed using a 13-station array that could be assembled within this decade. Images on the top correspond to a GRMHD simulation with a black hole spin of a=0.5 and an accretion disk inclination of 85 degrees from our line of sight. Bottom images correspond to a RIAF model with spin a=0 and disk inclination of 60 degrees. Models courtesy Charles Gammie and Avery Broderick.*

Doeleman et al. 2010 Decadel Survey

Imaging simulation of Sgr A* with the EHT.

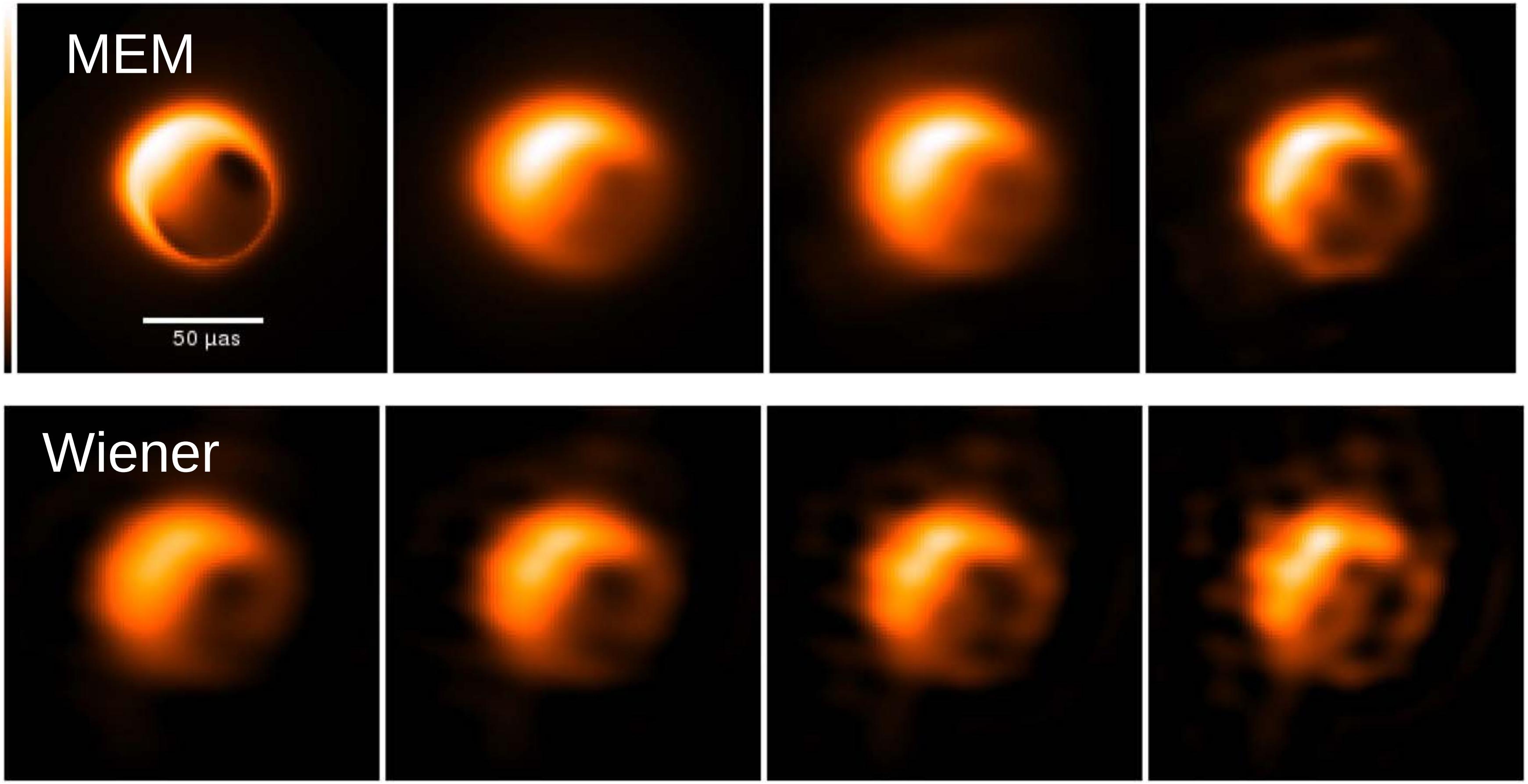

Fish et al. 2014 imaging in presence of scattering

Effect of a Polarized Spot Orbiting SgrA*

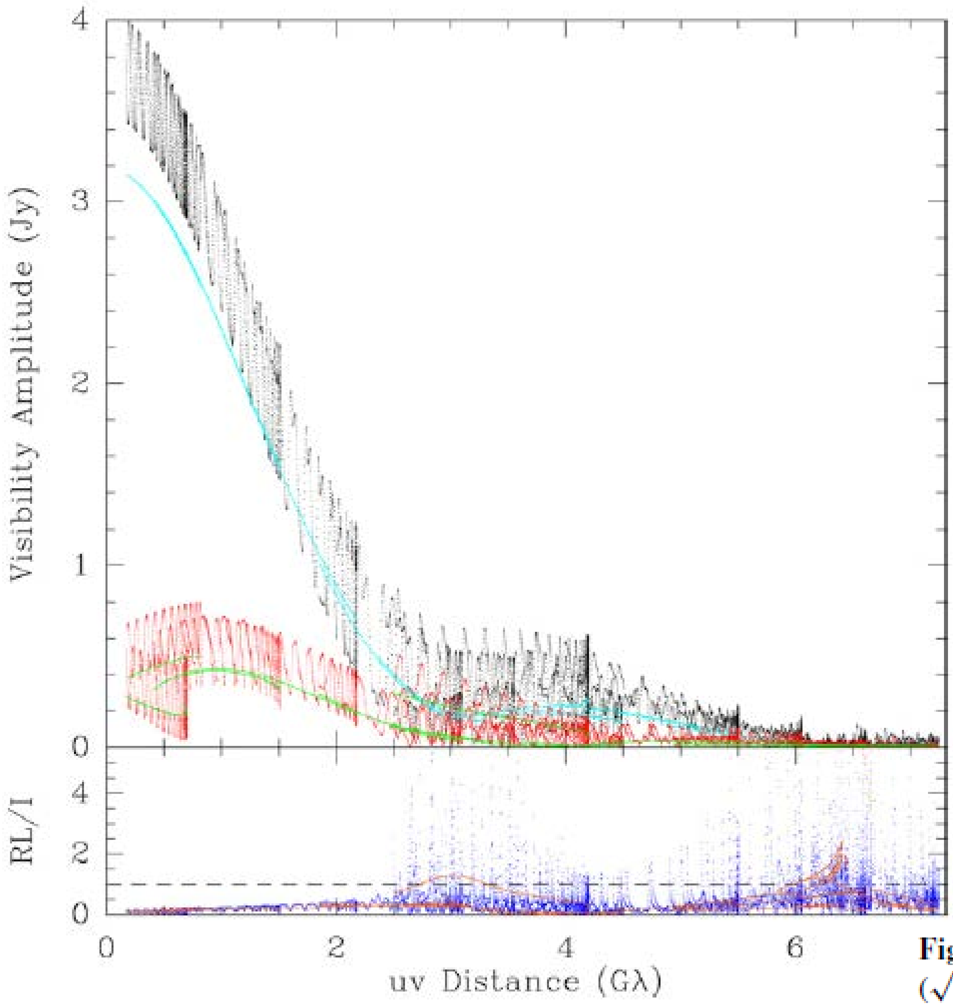

Fish et al. 2009

Figure 2. Top: visibility amplitude as a function of projected baseline length ($\sqrt{u^2 + v^2}$) for Model A at 230 GHz (noiseless). Stokes I is shown in black, and RL is shown in red. A real orbiting hot spot would persist for only a small fraction of a day, producing a plot corresponding to a subset of the above points. Contributions from the disk alone in the absence of a hot spot are shown in cyan (Stokes I) and green (RL). Bottom: ratio of RL/I visibility amplitudes for the disk and hot spot (blue) and disk alone (orange). On small scales, RL/I can greatly exceed unity.

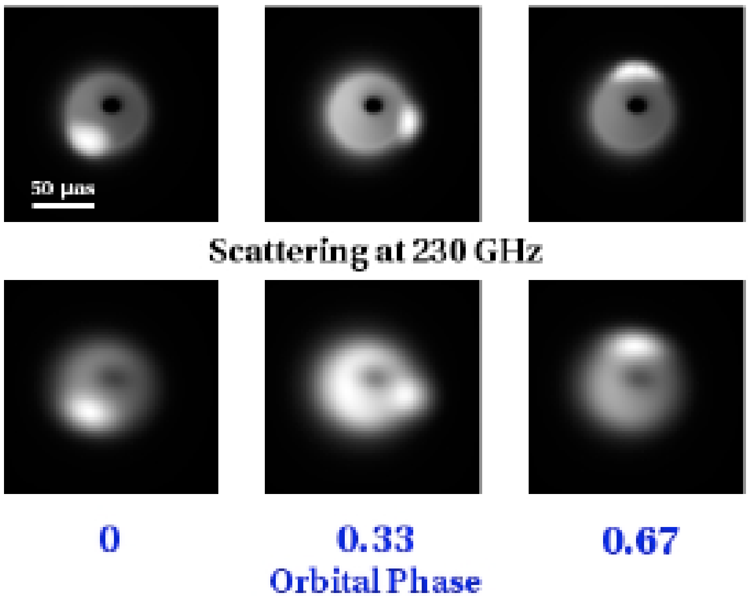

Doeleman et al. 2010 Decadel Survey

Effect of a Hot Spot Orbiting SgrA*

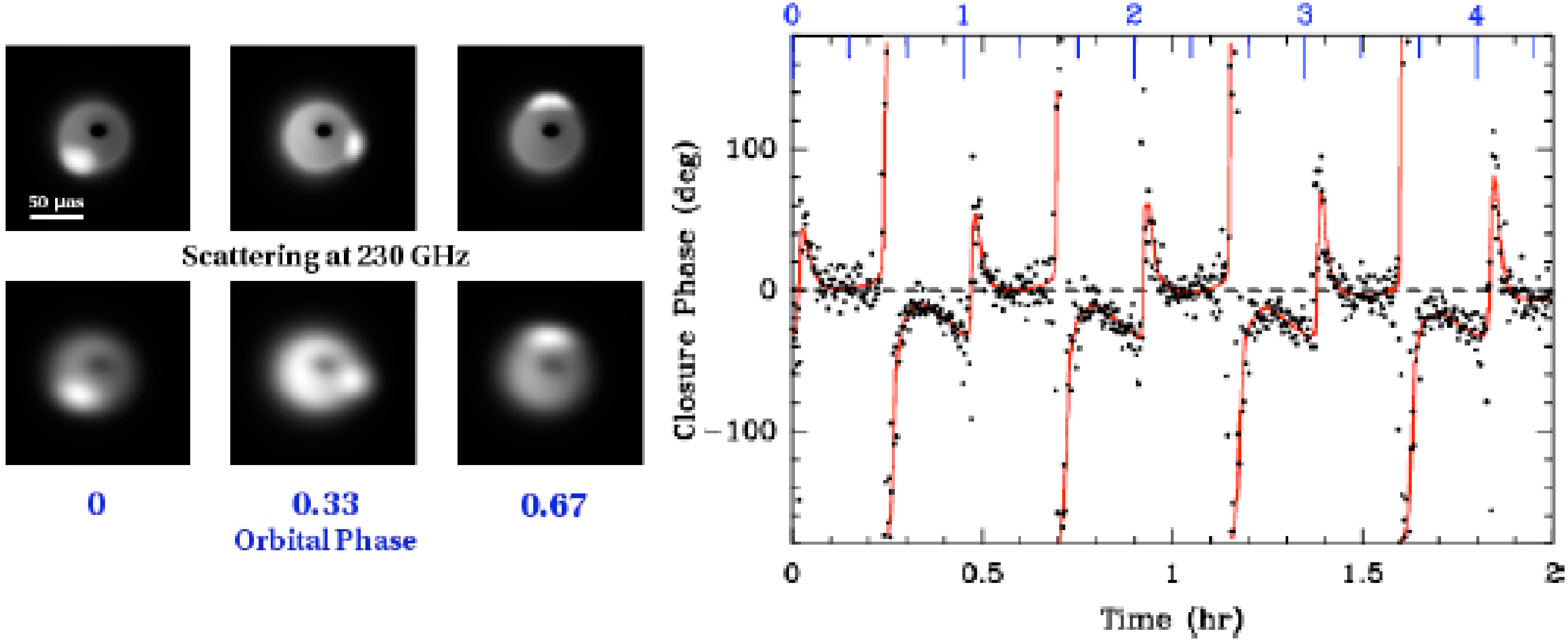

Figure 4: *Signature of a hot-spot orbiting the SgrA* black hole. The left panel shows a quiescent Radiatively Inefficient Accretion Flow (RIAF) model for a non-spinning 4x10*^{6} *solar mass black hole, and a hot spot orbiting at the Innermost Stable Circular Orbit (ISCO), with a disk inclination of 60 degrees from line of sight. The raw model is shown for 3 orbital phases in the top three figures, and the bottom three show the effects of scattering by the ISM. VLBI closure phase (the sum of interferometer phase over a triangle of baselines) is non-zero when asymmetric structure is present. The right panel shows 1.3mm wavelength VLBI closure phases every 10-seconds on the ARO/SMT-Hawaii-CARMA triangle with the model phases shown as a red curve (Doeleman et al. 2009).*

Doeleman et al. 2010 Decadel Survey

Effect of a Polarized Spot Orbiting SgrA*

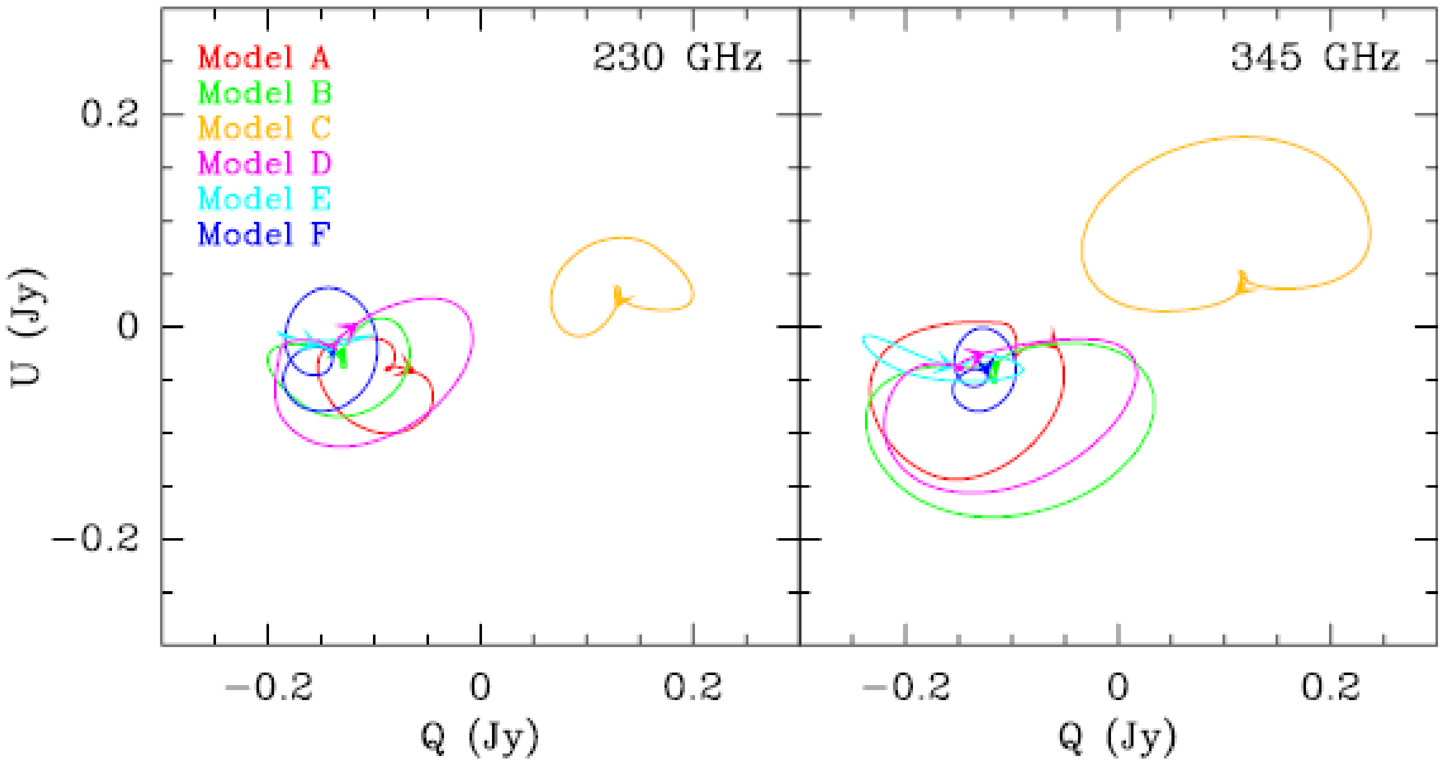

Figure 1. Integrated polarization traces of the models in the Stokes (Q, U) plane at 230 and 345 GHz over a full hot spot orbit, as would be seen by the SMA (for instance).

Fish et al. 2009

Jet vs. Core Luminosity in SgrA*

200x200 Rg   20x20 Rg

$\left(\left(\frac{T_p}{T_e}\right)_{disk}, \Theta_{e,jet}\right)$

(5,20)

(15,20)

(25,20)

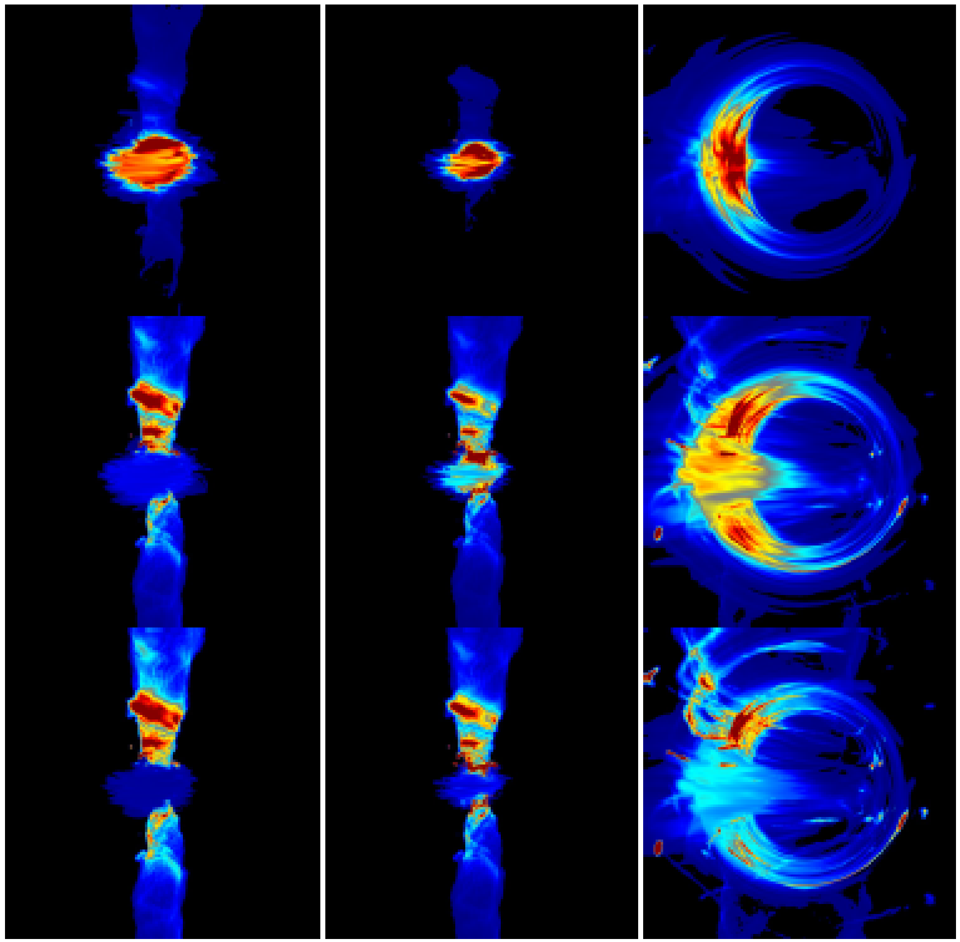

13 mm   7 mm   1.3 mm

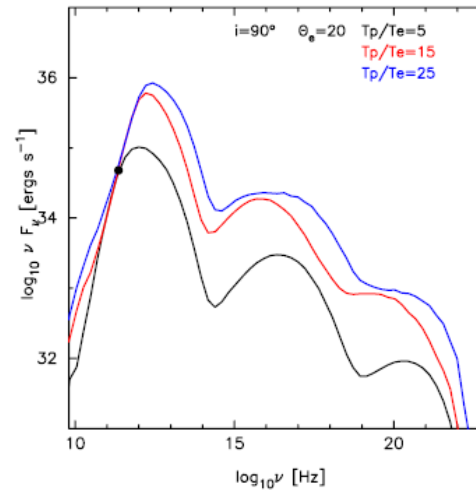

Jet:
const. E-Temp.

$$\frac{k_b T_e}{m_e c^2} = \Theta_{e,j} = \mathrm{const.}$$

Disk: proton
e-Temp. ratio

$$\frac{k_b T_e}{m_e c^2} = \left(\frac{k_b T_p}{\mu m_p}\right)\left(\frac{m_p}{m_e}\right)\frac{1}{(T_p/T_e)_{disk}}$$

Moscibrodzka et al., A&A 570, A7, 2014

Nature of some SgrA* radio flares

7 mm VLBA

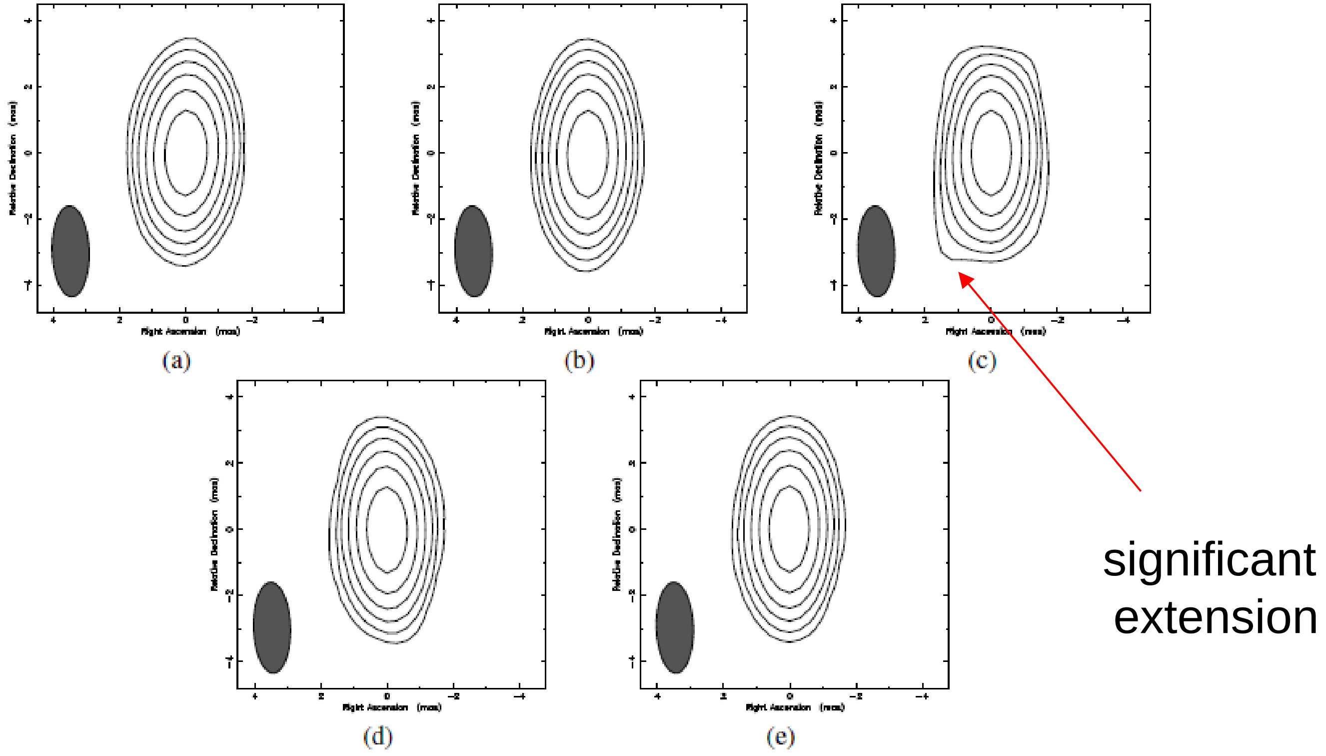

Fig. 5: 2 hour LCP maps of Sgr A* observed on May 17 2012. (a) May 17 6-8h. (b) May 17 7-9h. (c) May 17 8-10h. (d) May 17 9-11h. (e) May 17 10-12h. Summarized map parameters can be found in table 2.

Rauch et al. 2016

Nature of some SgrA* radio flares

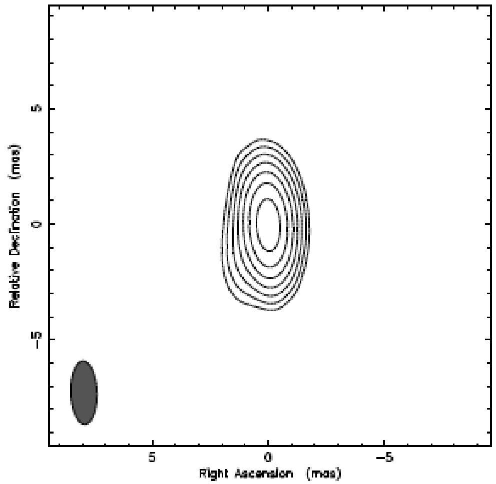

Fig. 7: RCP map of Sgr A* on May 17 2012 (8-10h UT). The map was convolved with a beam of 2.74×1.12 at 1.76°. Contour levels are 1, 2, 4, 8, 16, 32 and 64% of the peak flux density of 1.5 Jy/beam.

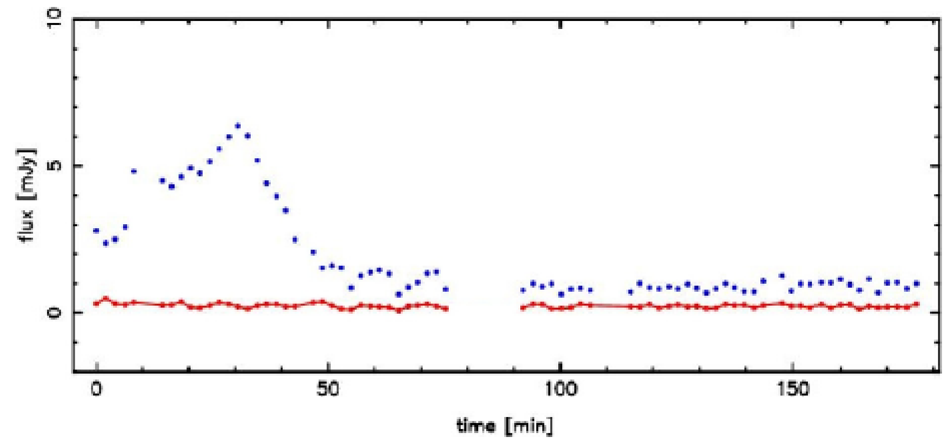

Fig. 3: NIR K_s-band (2.2 μm) light curve of Sgr A* observed in polarimetry mode on 17 May 2012. The light curve shown is produced by combining pairs of orthogonal polarization channels: 0° and 90° (taken from Shahzamanian et al. (2015)). Observations started at 4:55 AM UT.

Central component of 1.55 Jy secondary component of 0.02 Jy at 1.5 mas and 140 deg. E-N with a 4 hout delay relativ to the NIR flare

Bower et al. (2014) report major axis sizes of Sgr A* as an elliptical Gausssian of $35.4 \times 12.6\,R_S$ at an position angle of 95° east of north. Which is much lower than the discussed source morphology due to a secondary component of 0.02 Jy at 1.8±0.4 mas at 140° east of north.

Rauch et al. 2016

See also ‚Asyummetric structure in SgrA* …‘ Brinkerink et al. 2016, MNRAS 462, 1382 ‘speckle transfer function‘

MNRAS 462, 1382–1392 (2016)
Advance Access publication 2016 July 19

d

Asymmetric structure in Sgr A* at 3 mm from closure phase measurements with VLBA, GBT and LMT

Christiaan D. Brinkerink, et al.

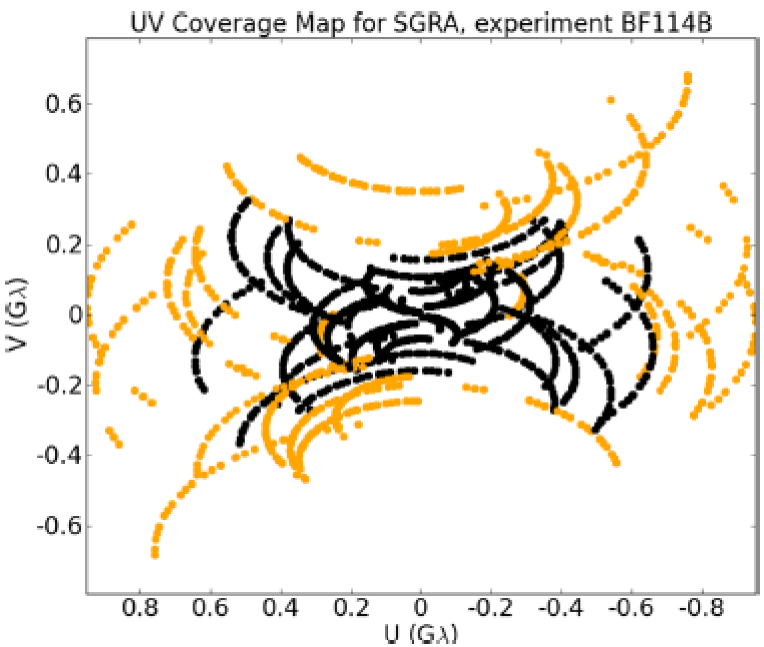

Figure 1. The (u, v) coverage for the observation of Sgr A* taken on 2015 May 23 (6:00–13:00 UT). Baselines within the VLBA are coloured black, baselines to LMT and GBT are coloured orange. No baselines to Mauna Kea (MK) are shown, as we have not found fringes for Sgr A* on any baseline to MK. The inclusion of LMT improves north–south (u, v) coverage, while the inclusion of GBT improves east–west coverage. Colour figures available in online version.

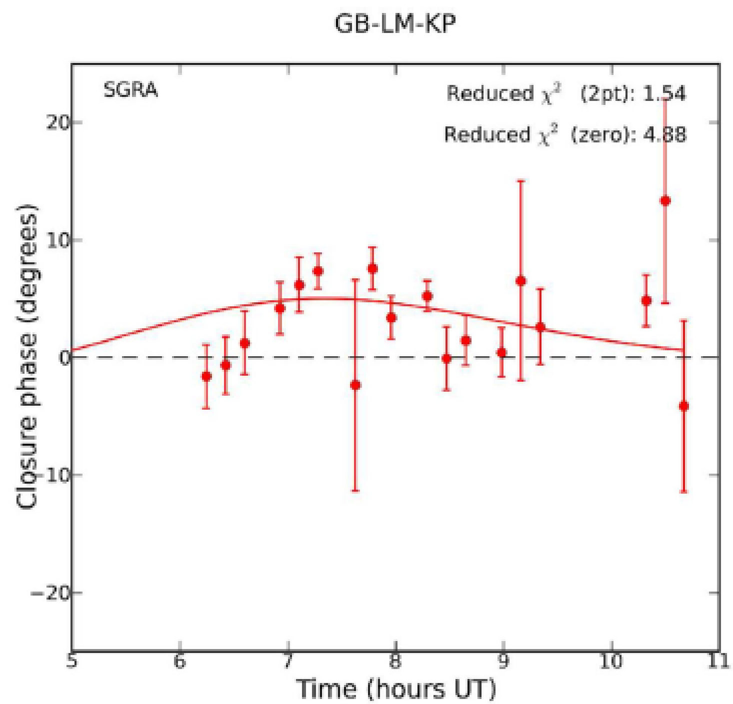

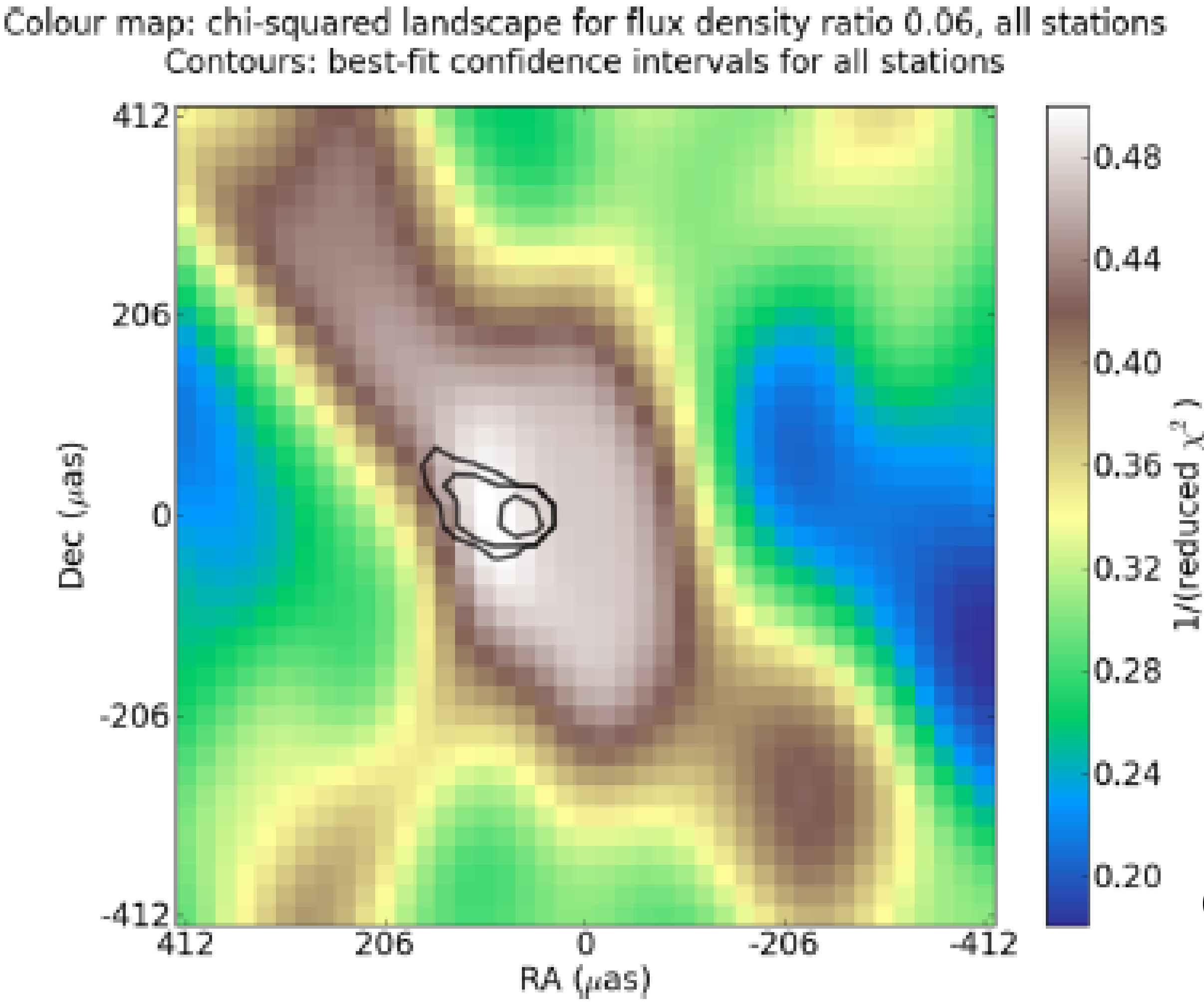

Figure 8. Confidence regions (black lines) for the best-fitting position of the secondary source component, obtained by bootstrapping the original closure phase data set. The innermost contour indicates the 99 per cent confidence region, surrounded by the 95 per cent and 68 per cent regions, respectively. Colour figures available in online version.

SgrA* at 86 GHz
VLBA, GBT, and LMT
find a 100uas offset
component.
This component could be
due to iterstellar scattering
or source intrinsic.

Brinkerink et al. 2016

THE ASTROPHYSICAL JOURNAL, 824:40 (10pp), 2016 June 10

GISELA N. ORTIZ-LEÓN[1] et al.

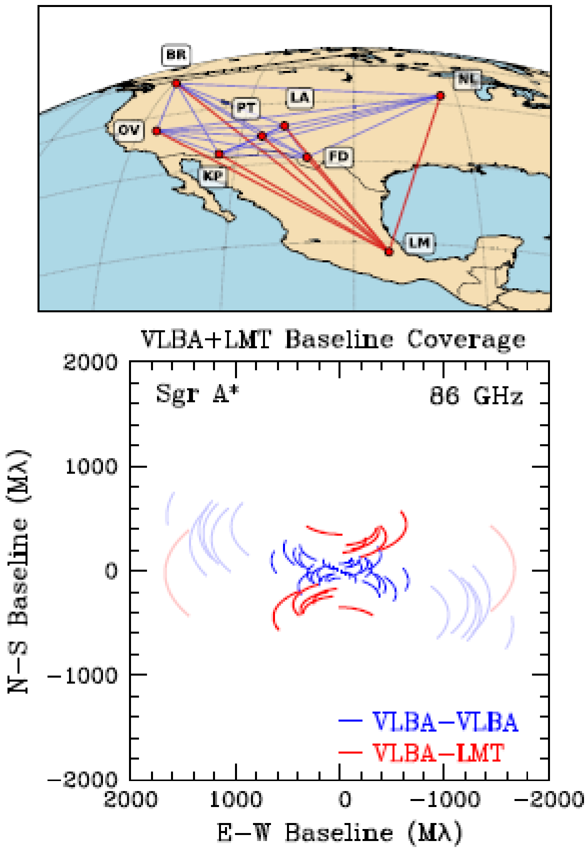

Figure 2. Top: the 3.5 mm stations of the VLBA and the LMT. Bottom: the corresponding u–v coverage; the faint tracks denote baselines to Mauna Kea, on which we do not detect Sgr A*.

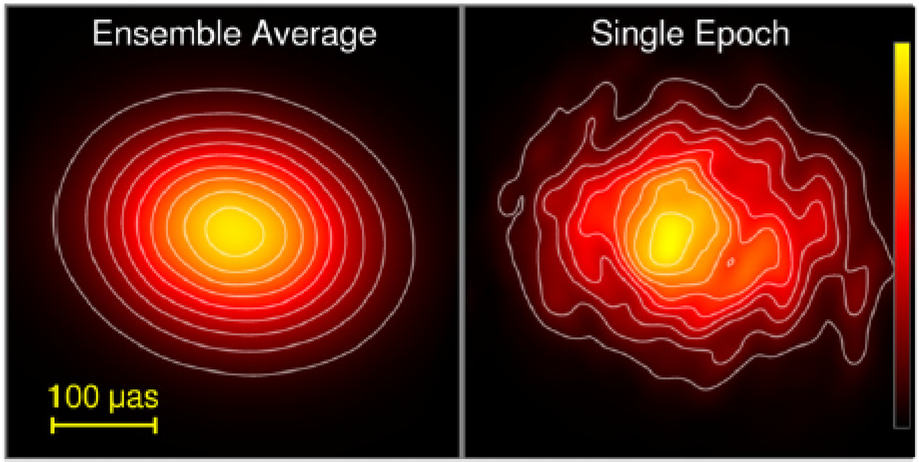

Figure 7. Simulated scattered images of Sgr A* at $\lambda = 3.5$ mm; color denotes brightness on a linear scale, shown at the far right and image contours are 10% to 90% of the peak brightness, in steps of 10%. The intrinsic source is modeled as a circular Gaussian with a FWHM of 130 μas; the ensemble-average scattered image has a FWHM of (206 μas) × (151 μas). The left image shows an approximation of the ensemble-average image, obtained by averaging 500 different scattering realizations. This image illustrates the "blurring" effects of scattering when averaged over time. The right image shows the appearance for a single epoch, which exhibits scattering-induced asymmetries that would persist over a characteristic timescale of approximately one week. Each image has been convolved with a 20 μas restoring beam to emphasize the features that are potentially detectable at $\lambda = 3.5$ mm.

Spectral properties in the radio domain

Radio properties of Quasars

Synchrotron radiation

single electron spectrum

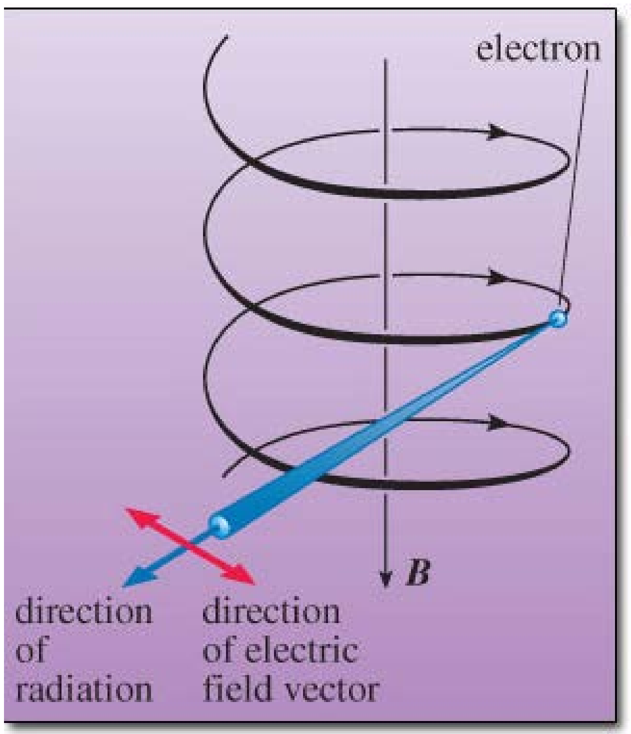

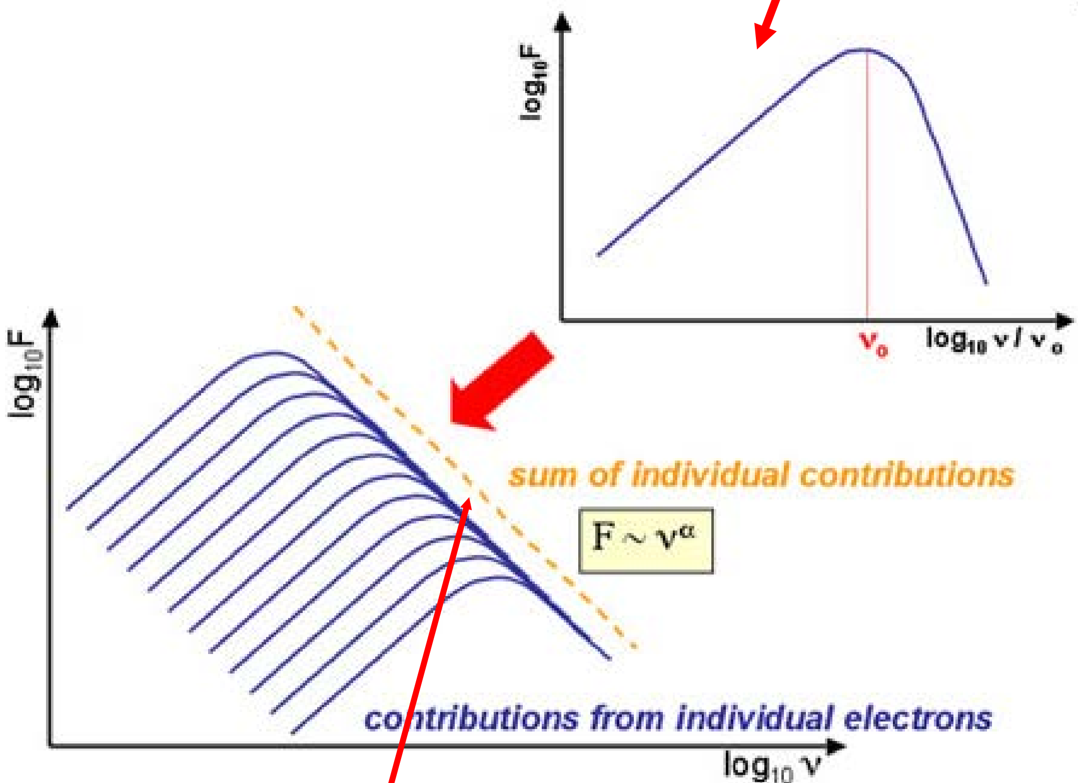

spectrum of electron ensamble

Synchrotron Radiation

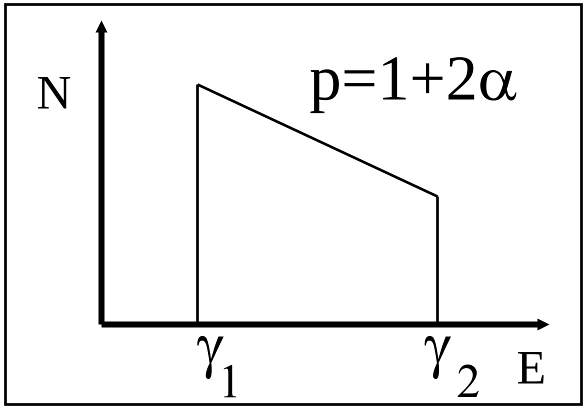

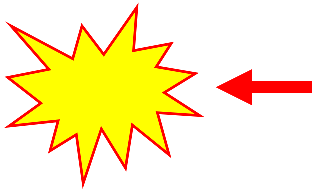

cloud of relativistic electrons threaded by tangeled magnetic field lines

relativistic electron spectrum

$$N(E) = N_0 E^{-(2\alpha+1)} (\gamma_1 mc^2 < E < \gamma_2 mc^2)$$

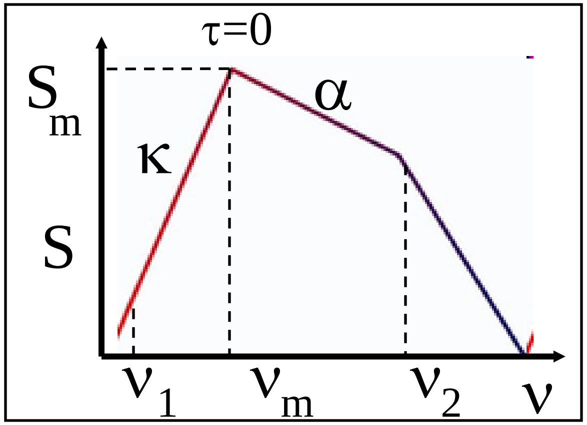

$$S_\nu \propto \nu^\alpha$$

α=-0.7

κ=+2.4

$$B = 10^{-5} b(\alpha) \theta^4 \nu_m{}^5 S_m{}^{-2} \left(\frac{\delta}{1+z} \right) \text{ gauss}$$

DIMENSIONLESS PARAMETERS OF THE SPECTRAL INDEX α

α	b	n	d
0.25	1.8	7.9	130
0.50	3.2	0.27	43
0.75	3.6	0.012	18
1.00	3.8	0.00059	9.1

with boosting factor δ

$$\delta\ (= \Gamma^{-1} [1 - \beta \cos \phi]^{-1}$$

and bulk Lorentz factor Γ

$$\Gamma = [1 - \beta^2]^{-1/2})$$

high freq. cutoff $\nu_2 = 2.8 \times 10^6 B \gamma_2{}^2$

Synchrotron Self Compton Mechanism

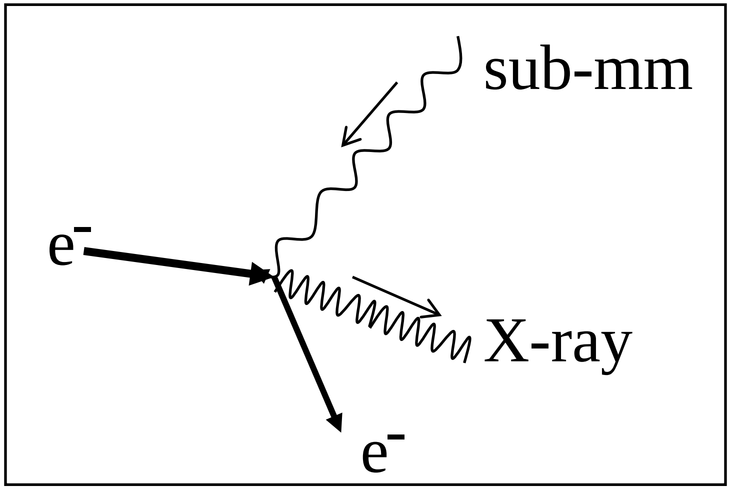

$$\gamma_e = (1-\beta_e^2)^{-1/2}$$

$$\Gamma_{bulk} = (1-\beta_{bulk}^2)^{-1/2}$$

$$\delta = \Gamma^{-1}(1-\beta_{bulk}\cos\phi)^{-1}$$

‘Isotropic‘ velocity distribution of relativistic electrons in cloud: γ
bulk motion of the entire cloud: Γ

SSC model

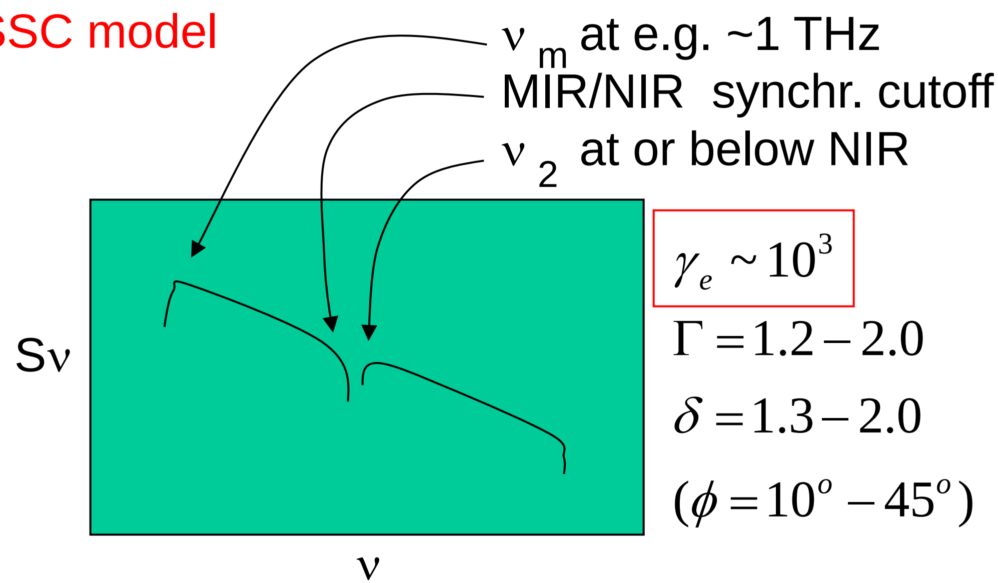

$$\gamma_e \sim 10^3$$

$$\Gamma = 1.2 - 2.0$$

$$\delta = 1.3 - 2.0$$

$$(\phi = 10^o - 45^o)$$

Synchrotron Self-Compton

particle density:

$$N_0 = n(\alpha) D_{\rm Gpc}^{-1} \theta^{-(4\alpha+7)} \nu_m^{-(4\alpha+5)} S_m^{2\alpha+3} \times (1+z)^{2(\alpha+3)} \delta^{-2(\alpha+2)} .$$

SSC flux density:

$$S_\nu^C(E_{\rm keV}) \approx d(\alpha) \ln(\nu_2/\nu_m) \theta^{-2(2\alpha+3)} \nu_m^{-(3\alpha+5)} \times S_m^{2(\alpha+2)} E_{\rm keV}^{-\alpha} [(1+z)/\delta]^{2(\alpha+2)} \ \mu\text{Jy}$$

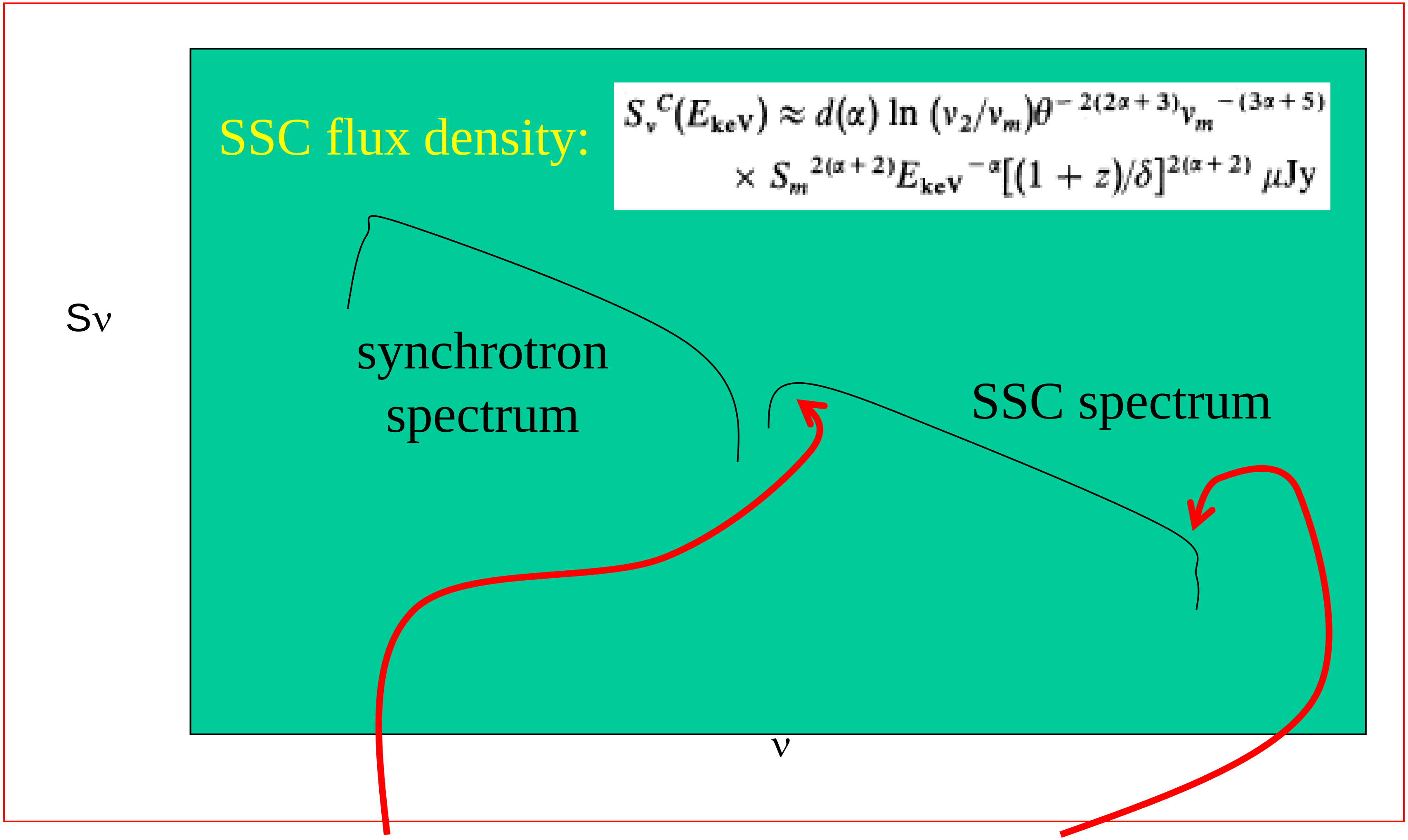

$$5.5 \times 10^{-9} \gamma_1^2 \nu_m \lesssim E_{\rm keV} \lesssim 0.2 b^{-1}(\alpha) \theta^{-4} \nu_2^2 \nu_m^{-5} S_m^2 [(1+z)/\delta]^2$$

Our VLBA survey of nearby bright LLAGN has found high brightness temperature (>10^8 K) radio cores in 16 of 17 objects observed, with four of them even hosting parsec scale jets, strongly suggesting that at least 20% of LLAGN are accretion powered. Few LLAGN show the steep radio spectra expected in an advection dominated accretion flow (ADAF).

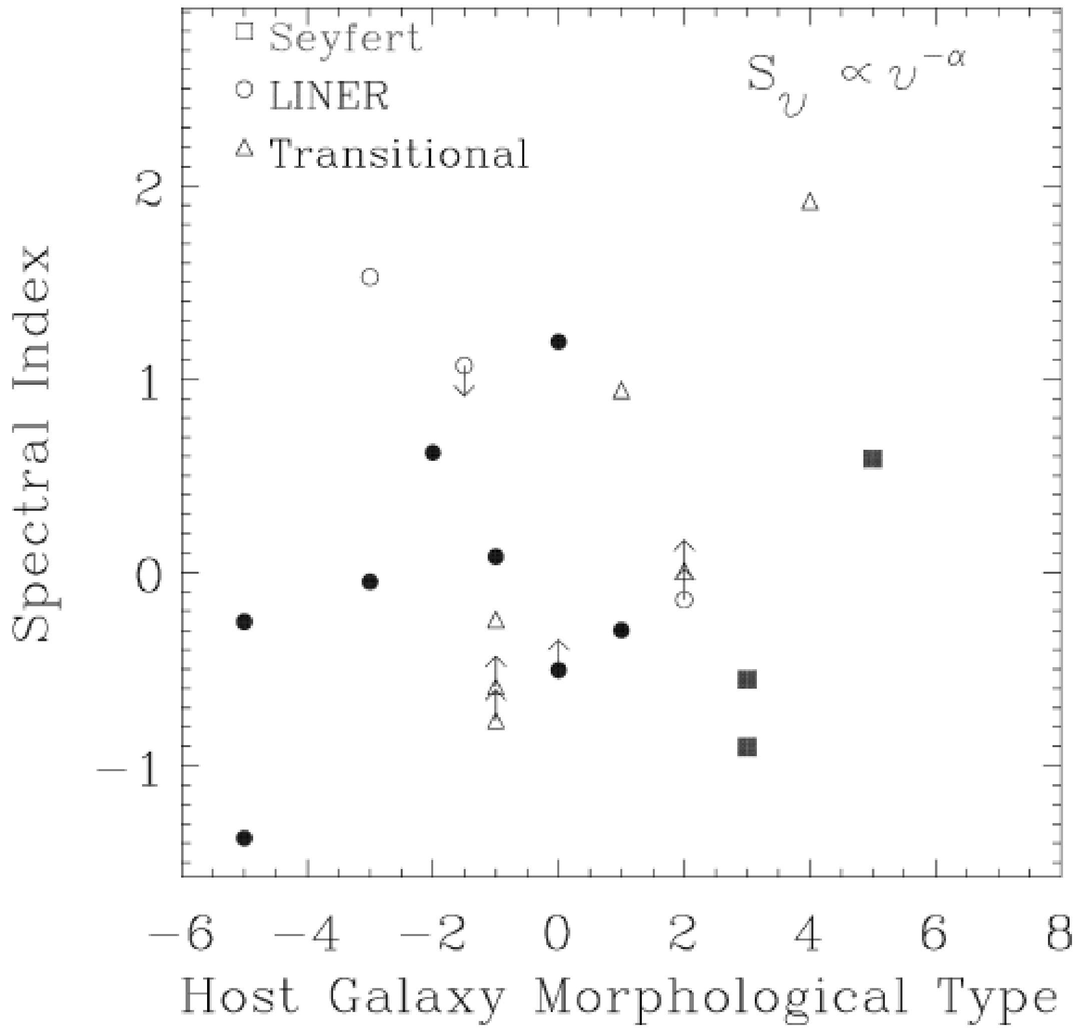

Nagar et al. 2002

Spectral index as derived from VLA 2, 3.6 or 6 cm data, as a function of host galaxy morphological type. Filled symbols represent type 1 objects, open symbols represent type 2 objects.

Synchrotron Modeling

Rapid variability time scales (< 1hour) imply a non-thermal radiation mechanism:

$$S_{X,ssc} = d(\alpha)\ln(\frac{\nu_2}{\nu_m})\theta^{-2(2\alpha+3)}\nu_m^{-(3\alpha+5)}S_m^{2(\alpha+2)}E_X^{-\alpha}\delta^{-2(\alpha+2)},$$

$$B = 10^{-5}b(\alpha)\theta^4\nu_m^5 S_m^{-2}\delta,$$

$$N_0 = n(\alpha)D_{Gpc}^{-1}\theta^{-(4\alpha+7)}\nu_m^{-(4\alpha+5)}S_m^{2\alpha+3}\delta^{-2(\alpha+2)},$$

Marscher 1983, 2009

Visualization of possible flare scenarii

$$S_m = \kappa_1 \nu^{-\alpha}$$

$$\theta = \kappa_2 \nu_m^{\zeta_1}$$

$$B = \hat{\rho} \nu_m^{\zeta_2}$$

$$N_0 = \kappa_3 \nu_m^{\zeta_3}$$

relativistic electron density

$$\rho = mc^2 \int_{\gamma_1}^{\gamma_2} N(\gamma) d\gamma = N_0 \frac{(mc^2)^{-2\alpha}}{2\alpha} (\gamma_1^{-2\alpha} - \gamma_2^{-2\alpha})$$

$$N(\gamma) = N_0 E(\gamma)^{2\alpha+1}$$

All important quantities can be written as powers of the turnover frequency.

All constants are functions of observables (spectral index and fluxes) or parameters

Eckart et al. 2012

Visualization of possible flare scenarii

Possible flare models

NIR X-ray

SYN-SYN: Synchrotron-synchrotron

SYN-SSC: Synchrotron-Self-Compton

SSC-SSC: Self-Compton-self-Compton

Visualization of possible flare scenarii

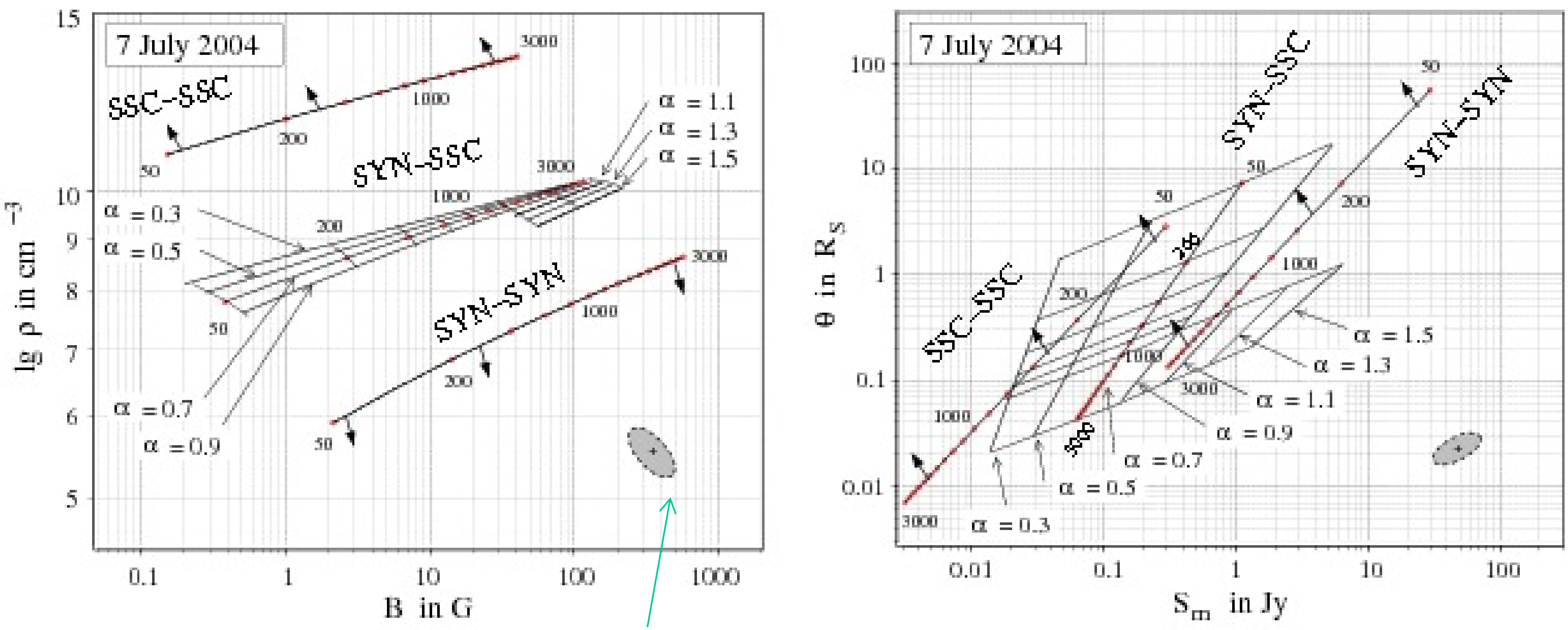

parameterized by case spectral index and turnover frequency νm.

Uncertainties due to measurement uncertaintuies

Solutions obey MIR flux limits (Schödel+ 2010,11) and: If SYN dominates - then less than 10% of the radiation should be due to SSC and vice versa.

Arrows point into directions of even more stringent constrains.

Eckart et al. 2012

Variability in the SYN-SSC case

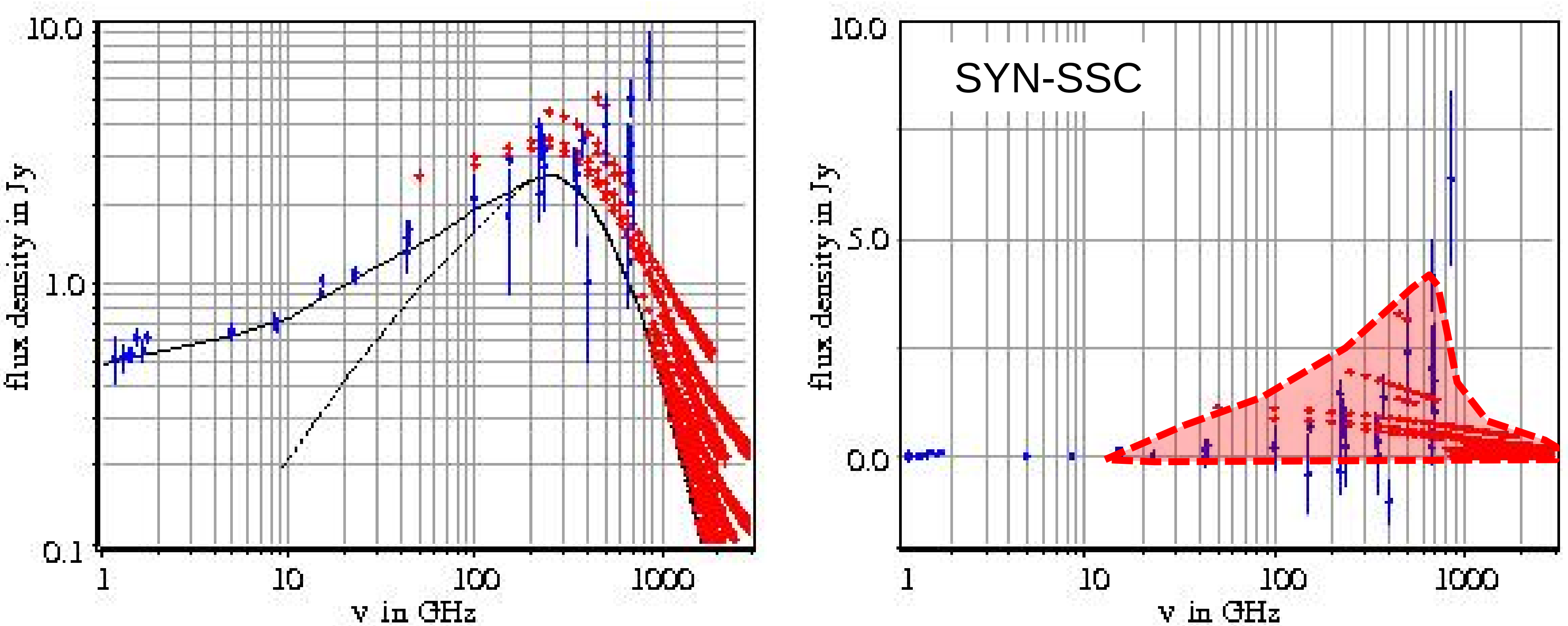

SYN-SSC: Density moderate;
consistent with MHD model of mid-plane;
Moderate demand on electron acceleration.

Eckart et al. 2012

Spectral properties in the X-ray domain
Statistics of NIR light curves of SgrA*

Synchrotron radiation is responsible for flux density variations in the NIR – which can be studied there best – without confusion due to fluxes from the larger scale accretion stream.

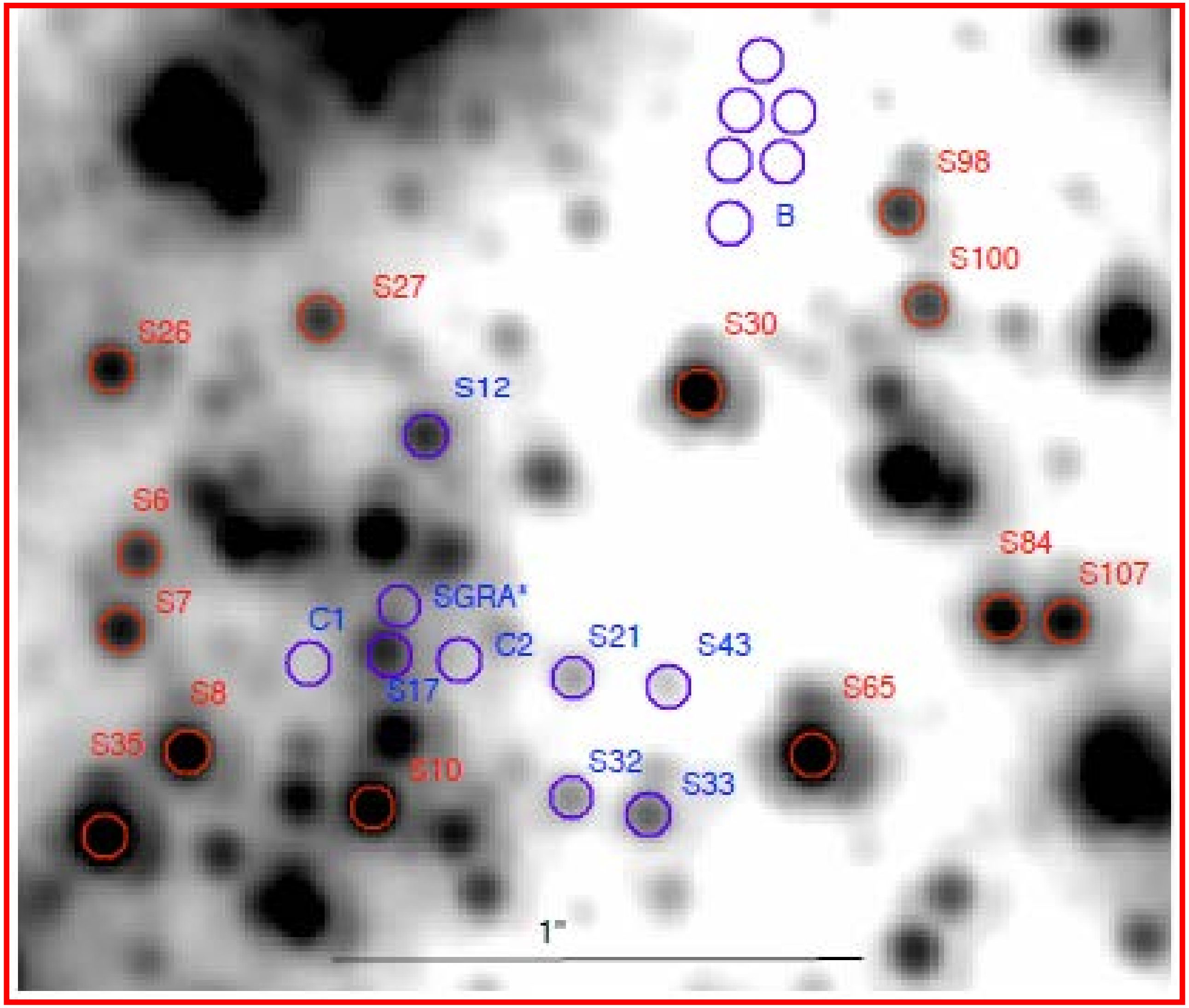

Measurements at 2 μm

Apertures on
(1) SgrA*.
(2) reference stars,
(3) and off-positions

Ks-band mosaic from 2004 September 30. The red circles mark the constant stars (Rafelski et al. 2007) which have been used as calibrators, blue the position of photometric measurements of Sgr A*, comparison stars and comparison apertures for background estimation (Witzel et al. 2012).

Witzel et al. 2012

NIR light curve of SgrA* over 7 years

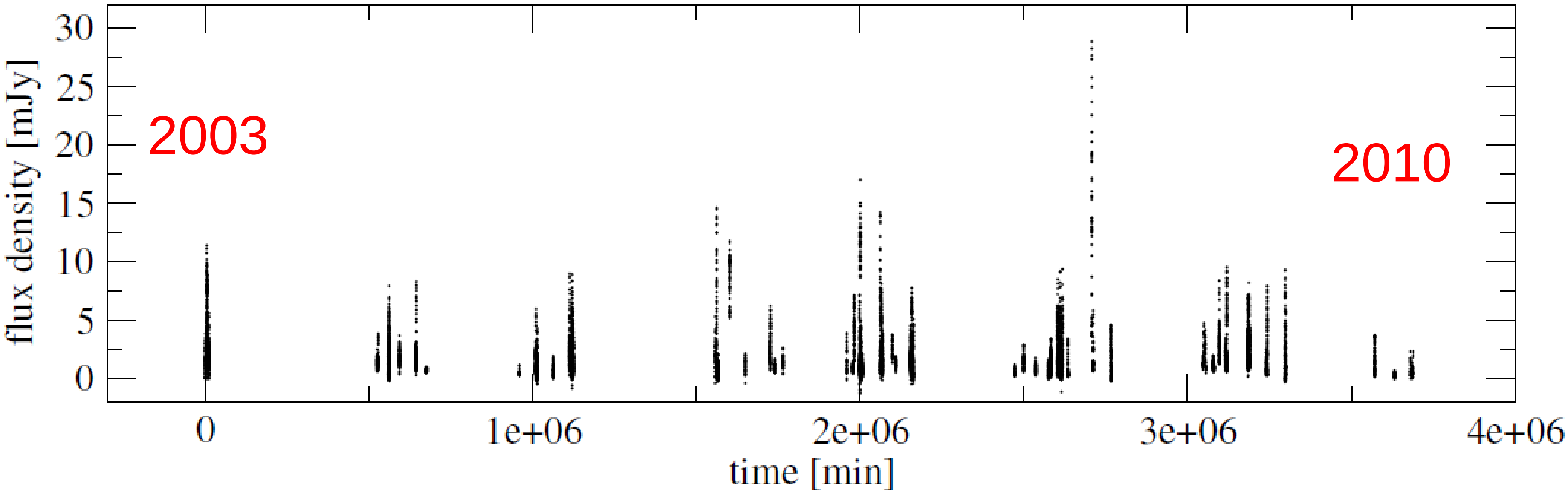

Light curve of Sgr A*. Here no time gaps have been removed, the data is shown in its true time coverage. A comparison of both plots shows: only about 0.4% of the 7 years have been covered by observations.

Witzel et al. 2012

Flux density histogram for SgrA*

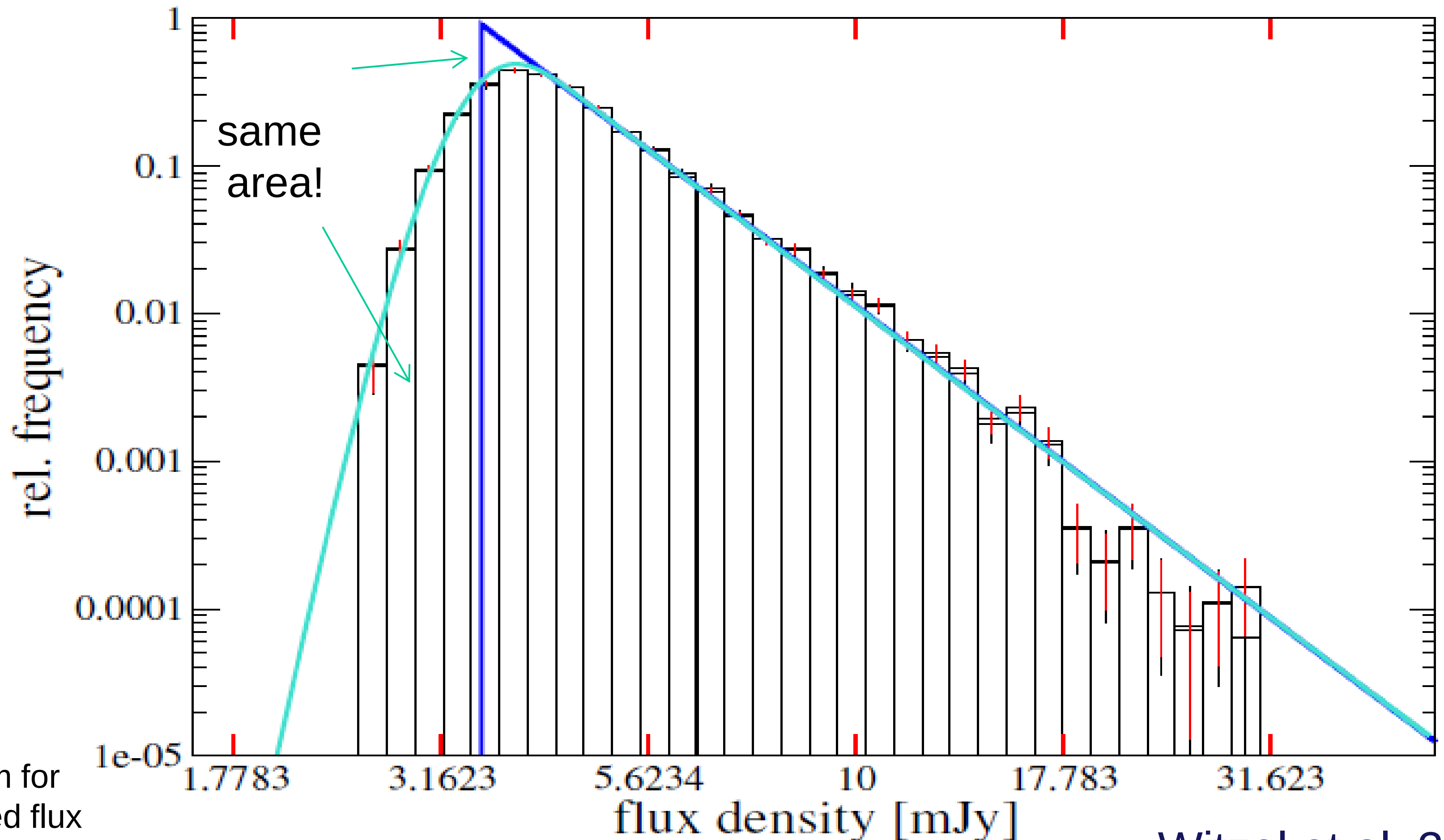

Diagram for polarized flux in work

Witzel et al. 2012

The brown line shows the extrapolation of the best power-law fit, the cyan line the power-law convolved with a Gaussian distribution with 0.32 mJy width.

X-ray light echo : variability of SgrA*

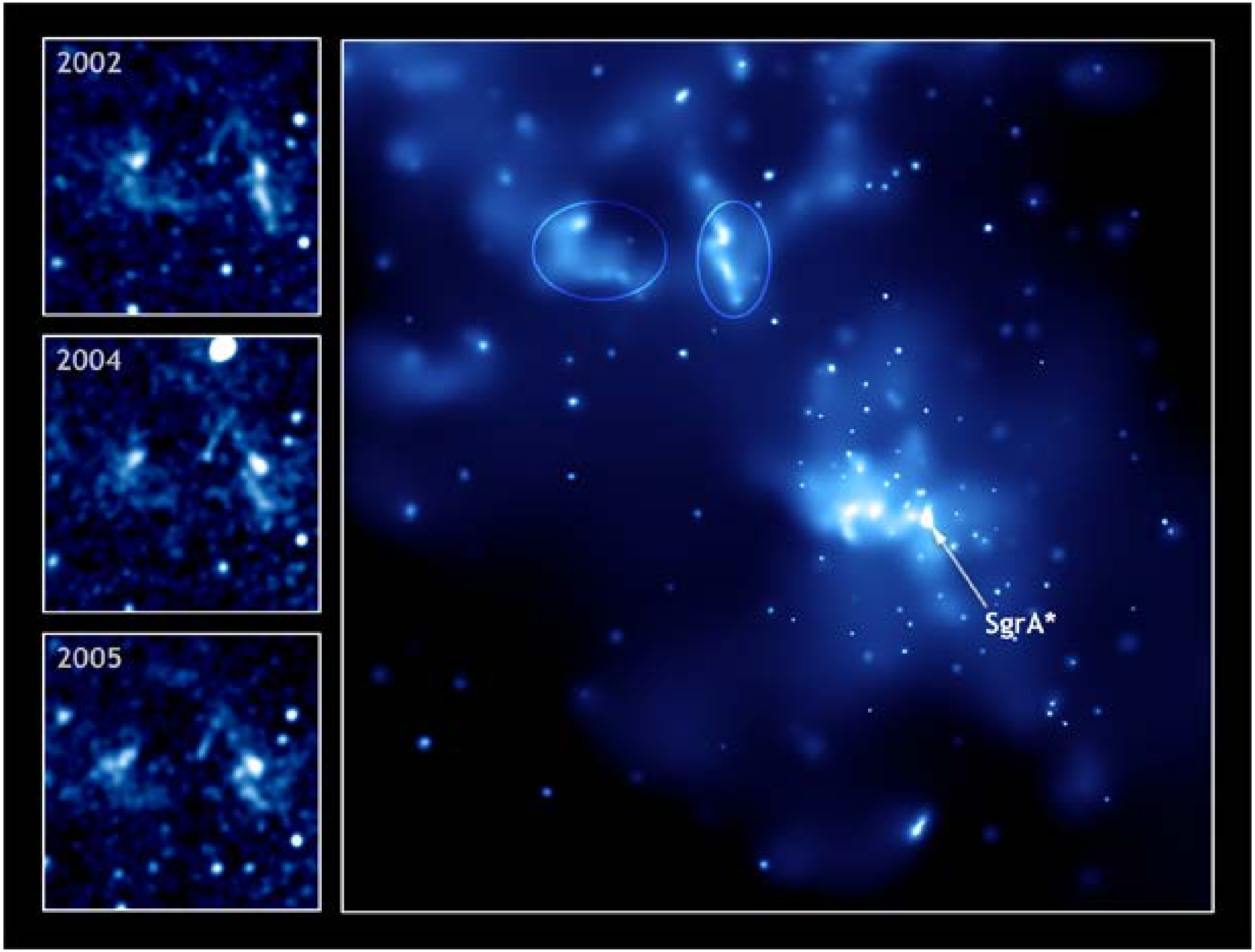

Chandra/ NASA

The statistics allows to explain the event 400 years ago that results in the observed X-ray light echo

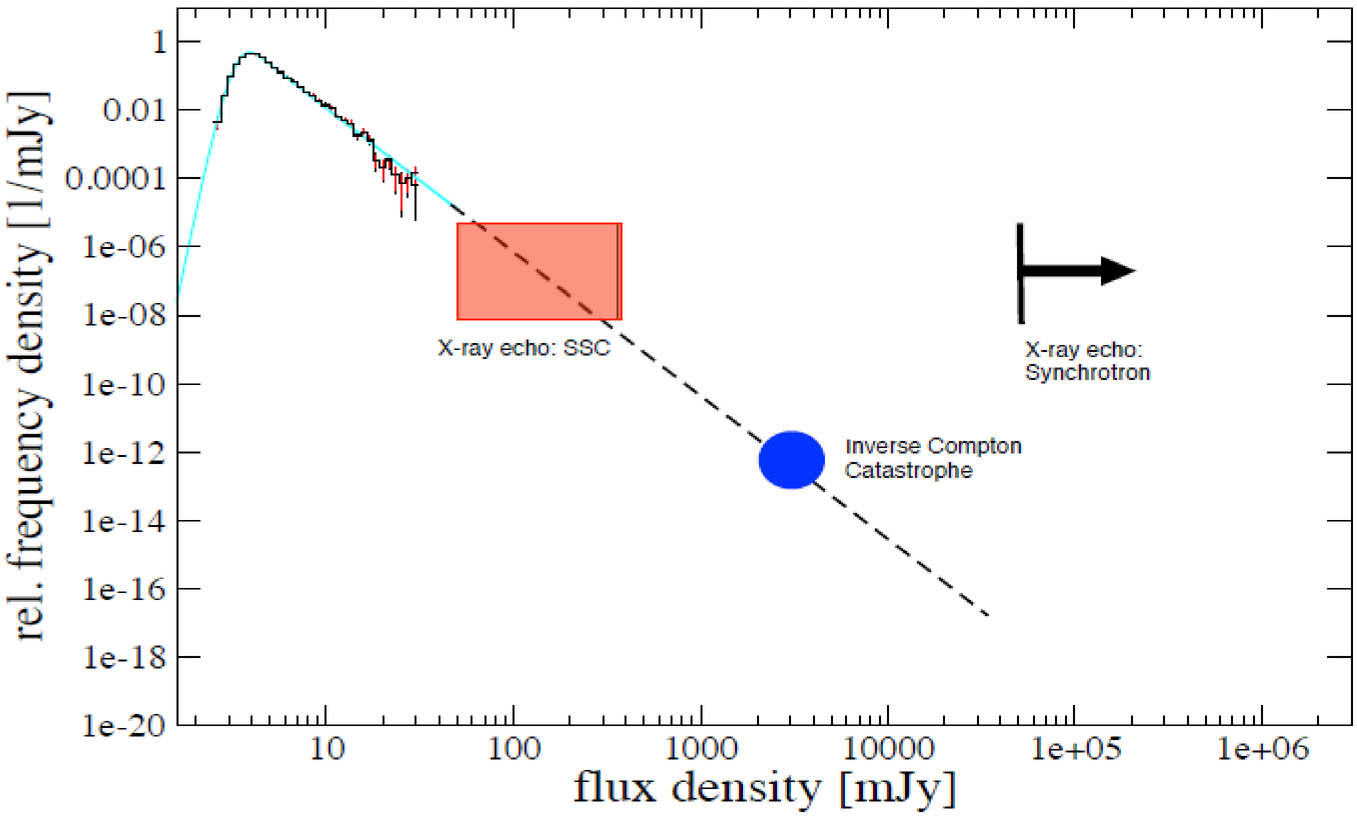

Fluorescent back-scatter from molecular clouds surrounding the GC:

Revnivtsev et al. 2004,
Sunyaev & Churazov 1998,
Terrier et al. 2010

and

Witzel et al. 2012

Illustration of a flux density histogram extrapolated from the statistics of the observed variability. The expected maximum flux density given by the inverse Compton catastrophe and a estimation of its uncertainty is shown as the magenta circle, the SSC infrared flux density for a bright X-ray outburst as expected from the observed X-ray echo is depicted as the red rectangular.

Spectral properties in the X-Ray domain

Chandra X-ray flare statistics in the 2-8 keV band

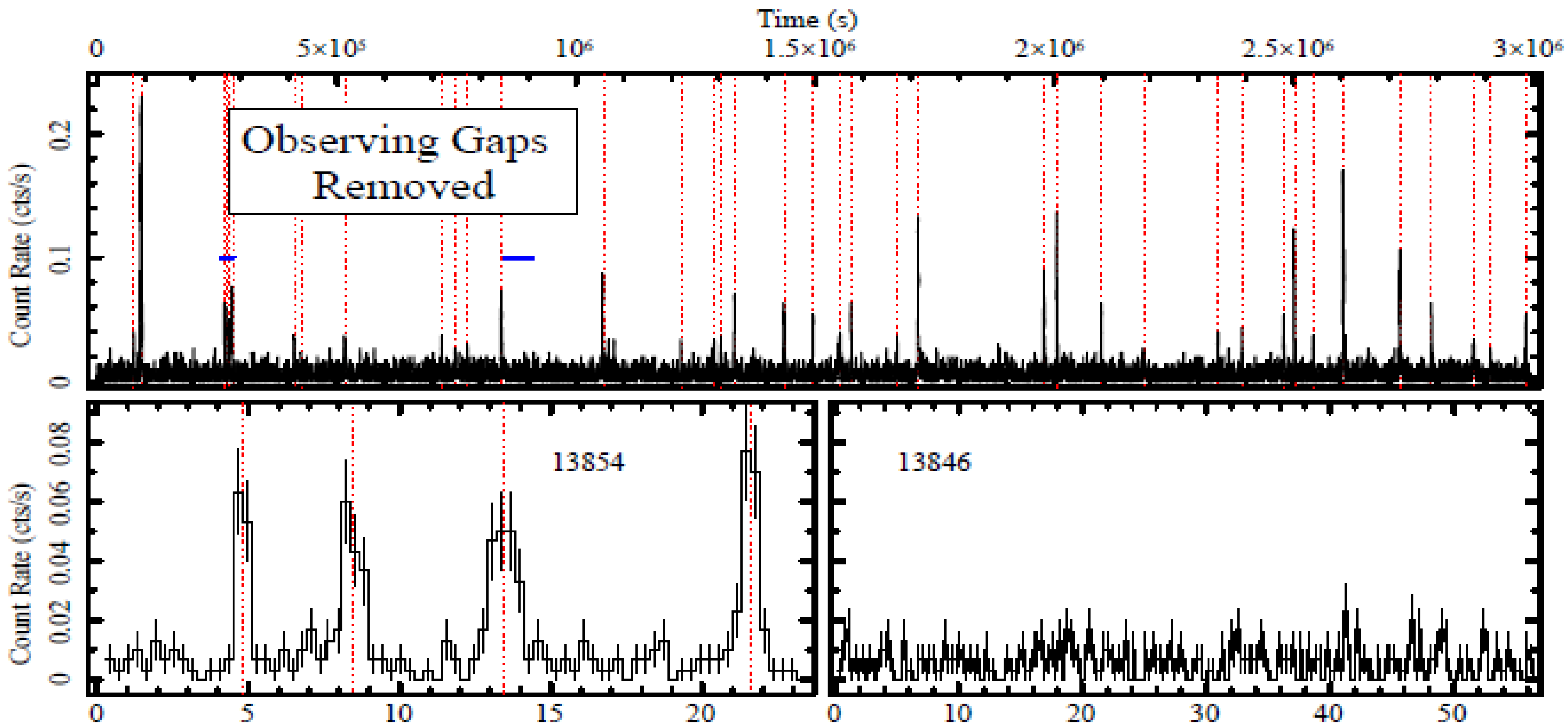

Neilsen, Novak et al. 2013: 39 detected flares in the 3Ms X-ray Visionary Project (XVP) observations. **Mean X-ray flare rate: ~1 per day; (NIR ~4/day);** mean X-ray flare luminosity 5x10^34 erg/s (10 times fainter than the brightest Chandra flare; Novak et al. 2012); up to Γ=2; dN/dL~L^(-1.9+-0.4)

2012 NuSTAR flares in the 3-79 keV band

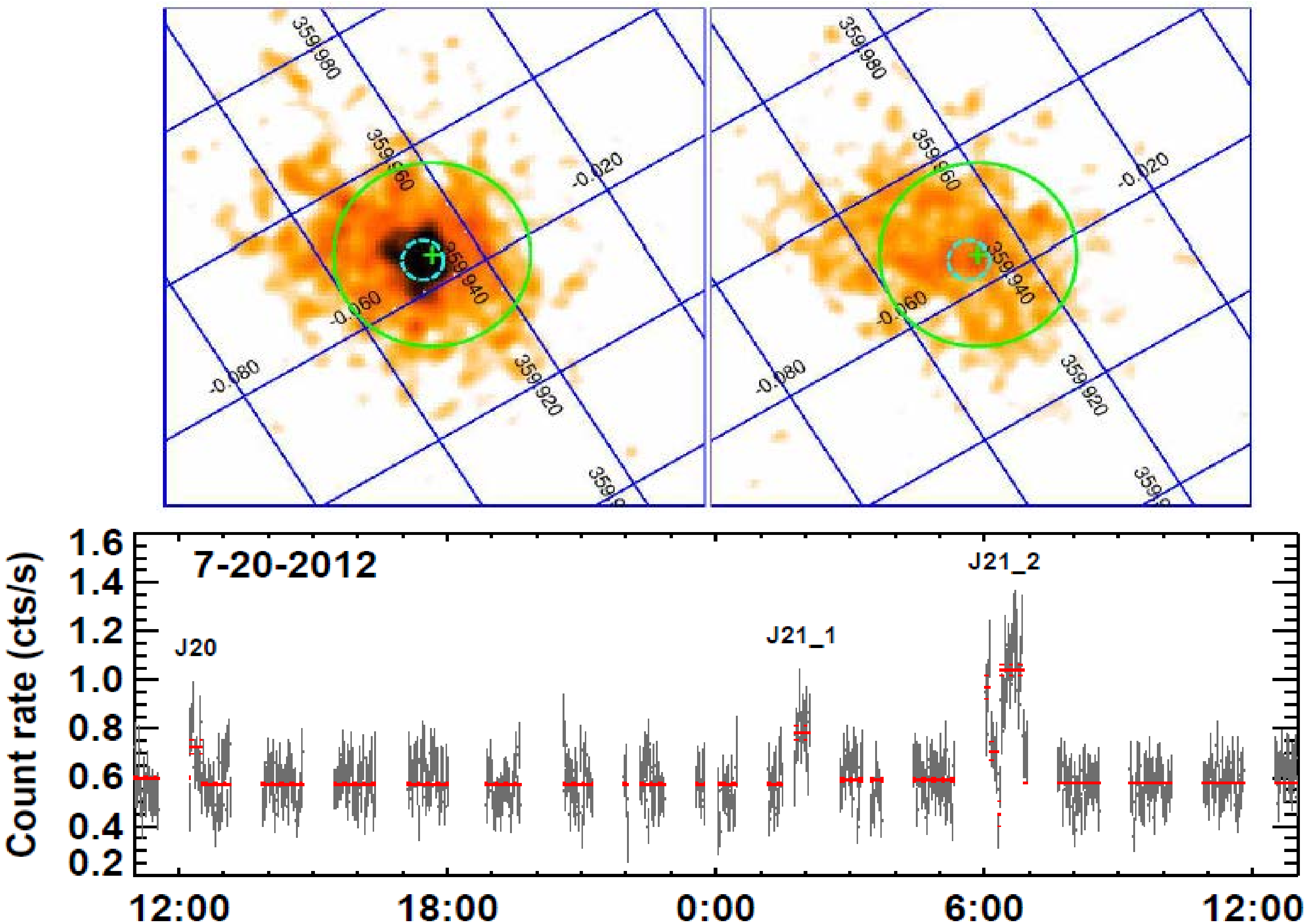

Barriere et al. 2014

NuSTAR‘s focal plane module A images (4.5‘x4.5‘) of the July 2012 flare J21_2 on and off the event including the light curve.